Elastic turbulence in porous media

Christopher A. Browne

a dissertation
presented to the faculty
of princeton university
in candidacy for the degree
of Doctor of Philosophy

recommended for acceptance
by the Department of
Chemical and Biological Engineering

Adviser: Sujit S. Datta

May 2022

Abstract

Polymer additives have potential as a key engineering tool for modifying environmental, industrial, energy, and microfluidic flows. In many cases, polymer elasticity can drive unstable, chaotic flow fluctuations in many ways reminiscent of turbulence, despite the absence of inertia that is typically requisite. While this unstable flow is well-studied in unconfined settings, it remains poorly understood how—or even if—this instability arises in complex, tortuous porous media, which are characteristic of environmental, industrial, energy, and microfluidic applications. In this dissertation, we address this gap in knowledge by fabricating transparent porous media of controlled geometries and directly imaging the flow in situ. First, using 1D pore arrays, we demonstrate that polymers accumulate memory along the successive expansions and contractions of a porous medium, and produce a surprising bistability in the stationary pore-scale flow state. Next, using 3D bead packings, we demonstrate for the first time that elastic turbulence can arise in disordered 3D porous media at flow conditions relevant to industrial applications. Leveraging this new knowledge of the underlying flow, we develop a theoretical model for the macroscopic flow resistance at varying flow rate, providing the first quantitative link between microscopic fluctuations and macroscopic transport of polymer solutions in porous media, resolving an over-50-year-old puzzle. We then extend this model to stratified porous media characteristic of many environmental applications. We demonstrate that elastic turbulence arises at distinct macroscopic flow rates in individual strata, allowing design of flow conditions that leverage the concomitant increase in flow resistance to redirect flow to low permeability strata and homogenize the flow across strata. Our ongoing work indicates these findings can be generalized to other polymer solutions, and leveraged for new applications, like enhanced mixing under confinement. These results suggest that many modeling approaches from inertial turbulence can be adapted for elastic turbulence—thus providing new avenues to understand, control, and engineer chaotic flows in confined spaces.

Contents

Citations to Previously Published Work

Chapter 1 is based in part on a published review by Christopher A. Browne, Audrey Shih, and Sujit S. Datta. Pore-Scale Flow Characterization of Polymer Solutions in Microfluidic Porous Media. *Small*, 16(9):1903944, 2019.[1]

Chapter 2 has been adapted from published work by Christopher A. Browne, Audrey Shih, and Sujit S. Datta. Bistability in the unstable flow of polymer solutions through pore constriction arrays. *the Journal of Fluid Mechanics*, 890, 2020.[2] **Author Contributions:** C.A.B. performed all experiments; C.A.B. and A.S. performed the image processing; C.A.B. and S.S.D. designed the experiments, analyzed the data, discussed the results, and wrote the manuscript. S.S.D. designed and supervised the overall project.

Chapter 3 has been adapted from published work by Christopher A. Browne and Sujit S. Datta. Elastic turbulence generates anomalous flow resistance in porous media. *Science Advances*, 7:eabj2619, 2021.[3] **Author Contributions:** C.A.B. performed all experiments; C.A.B. and S.S.D. designed the experiments, analyzed the data, developed and implemented the theoretical model, discussed the results, and wrote the manuscript. S.S.D. designed and supervised the overall project.

Chapter 4 has been adapted from unpublished work by Christopher A. Browne, Richard B. Huang, Callie W. Zheng, and Sujit S. Datta. **Author Contributions:** C.A.B. performed all experiments; C.A.B. and R.B.H. developed the 2-layer parallel resistor model; C.A.B. and C.W.Z. developed the n-layer parallel resistor model; C.A.B. and S.S.D. designed the experiments, analyzed the data, discussed the results, and wrote the manuscript. S.S.D. designed and supervised the overall project.

Chapter 5 is based on ongoing unpublished work by Christopher A. Browne, Richard B. Huang, Reinier van Buel, Holger Stark, and Sujit S. Datta. **Author Contributions:** C.A.B. conducted all experiments on solute mixing. R.B.H. conducted all experiments on solution generality. C.A.B, R.B.H., and S.S.D. designed the experiments, analyzed the data, and discussed the results. C.A.B, R.v.B., H.S., and S.S.D. wrote the text. S.S.D. designed and supervised the overall projects.

All movies can be found online at https://github.com/cabrowne/dissertation-movies.

Citations to other work not included in this thesis

Infection percolation: A dynamic network model of disease spreading. Christopher A. Browne, Daniel B. Amchin, Joanna Schneider, Sujit S. Datta. *Frontiers in Physics*, 9:171, 2021.[4]

Numerical investigation of multistability in the unstable flow of a polymer solution through porous media. Manish Kumar, Soroush Aramideh, Christopher A. Browne, Sujit S. Datta, and Arezoo M. Ardekani. *Physical Review Fluids*, 6(3):033304, 2021.[5]

Forced imbibition in stratified porous media. Nancy B. Lu, Amir A. Pahlavan, Christopher A. Browne, Daniel B. Amchin, Howard A. Stone, and Sujit S. Datta. *Physical Review Applied*, 14(5):054009, 2020.[6]

Controlling capillary fingering using pore size gradients in disordered media. Nancy B. Lu, Christopher A. Browne, Daniel B. Amchin, Howard A. Stone, and Sujit S. Datta. *Physical Review Fluids*, 4(8):084303, 2019.[7]

Cooperative size sorting of deformable particles in porous media. Margaret G. O'Connell, Nancy B. Lu, Christopher A. Browne, and Sujit S. Datta. *Soft Matter*, 15(17):3620–3626, 2019.[8]

To all the hazy thoughts in search of an experiment.

... so much of good science—and perhaps all of great science—has its roots in fantasy.

Edward O. Wilson, Letters to a Young Scientist

Acknowledgments

It is my pleasure to acknowledge several minor heroes of my life, who I have been lucky enough to meet and receive valuable feedback: P. E. Arratia, J. C. Conrad, M. D. Graham, S. J. Haward, G. H. McKinley, and A. Q. Shen. My committee A. Z. Panagiotopoulos, R. K. Prud'homme, and H. A. Stone for more valuable thoughts than they realize, and in particular the Stone lab for access to their rheometer and SLA printer.

Acknowledgment is made to the Donors of the American Chemical Society Petroleum Research Fund for partial support of this research through grant PRF 59026-DNI9. This material is also based upon work supported by the National Science Foundation Graduate Research Fellowship Program (to C.A.B.) under Grant No. DGE-1656466. Any opinions, findings, and conclusions or recommendations expressed in this material are those of the authors and do not necessarily reflect the views of the National Science Foundation. C.A.B. was also supported in part by the Mary and Randall Hack Graduate Award of the High Meadows Environmental Institute, and the Wallace Memorial Fellowship.

To my incredible lab, who over coffee and tahini cookies have stimulated so many of these ideas: N. Lu, J. Cho, D. Amchin, M. Derakhshandeh, T. Bhattacharjee, N. C. P. D. Bizmark, J. Schneider, J. Ott, J. Louf, K. Bay, A. Hancock, S. Gonzalez La Corte, A. Martínez-Calvo and E. Chen. Emily, I hope you enjoy their company as much as I have.

To my amazing mentees, A. Shih, M. O'Connell, R. B. Huang, K. Yeung, M. Slutzky, and C. W. Zheng. Your role cannot be overstated, and you are the reason I do research.

To my advisor Sujit Datta, for bringing me along on this incredible journey. Thank you for crafting this space for us to learn. You have shown me what it means to savor science.

Thank you to the life-long friends that made 159 into a home: Charles Argon, Isaac Breinyn, Drew Carson, Jordana Composto, Sebastian Gonzalez La Corte de la Cruz, Jean-François Louf, capt. Galen Mandes, Joanna Schneider, Evan Underhill, Sacha Welinski, and Avi Wolf. I am lucky to have passed each of you in this place, and am thankful we will not have to say good bye.

Finally, thank you to my family: Kimberly, Cynthia, and Robert Browne. Your creativity has been imprinted on me—and this dissertation—more than you realize.

Therefore, since brevity is the soul of wit,
And tediousness the limbs and outward flourishes,
I will be brief.

William Shakespeare, Hamlet

Preface

Dissertations are rarely read and seldom enjoyed. Formal publications already describe this work in technical detail; the academic reader will prefer those documents regardless. You are a friend, family, or (one can dream) a genuinely interested stranger; for you, I have aimed to write something pleasurable—or at least bearable—to read.

Turbulence is the most important unsolved problem of classical physics.

Richard Feynman, 1964 lectures on physics

1

Introduction

In 1964, Richard Feynman called turbulence "the most important unsolved problem of classical physics." This chaotic motion of fluids has garnered intrigue for centuries because it is at once fundamentally unpredictable yet staggeringly universal: the same fractal patterns emerge in the wakes behind flying bugs and behind planes, and the mixing creamer

in our coffee is not so different from a freshwater river dumping into the ocean. This chaos generally carries with it an elevated transport of momentum, solutes, and heat that play crucial roles in a wide range of environmental, industrial, and medical flows. Turbulence is used broadly in the chemical engineering industry to provide enhanced reactive solute mixing in stirred tank reactors and combustion chambers, and enhanced heat transfer in heat exchangers and cooling fins. Turbulence also carries with it an elevated resistance to flow, indicative of a higher rate of viscous dissipation of macroscopic mechanical work into heat, which is important to minimize for the aerodynamics around vehicles and aircraft and to maximize for the propulsion of helicopters, rockets, and watercraft.

Yet turbulence has its limits, and the Achilles's heel is *confinement*. We now understand well that the inertia of moving fluid particles provides a type of transient "memory" that drives this chaotic flow state, while under strong geometric confinement the viscous dissipation of momentum into heat "erases" this memory. This viscous suppression is inevitable in a broad range of environmental and industrial processes—from flow through the tight pore space of groundwater aquifers, to chemical processing in packed beds and chromatography columns, and reactions in the tiny channels of microfluidics and medical diagnostic chips. In these settings, momentum transfer is static in time, solute mixing is diffusion-limited, and heat transfer is conduction-limited.

The solution, then, is to find another type of chaos. We now come to recognize turbulence as part of a broader class of chaotic transport phenomena. Weather patterns in the atmospheric boundary layer exhibit a peculiar variation of turbulence confined to 2D,[9] and a variety of living systems from the microtubules in our cells to collections of bacteria can produce a reminiscent chaotic flow.[10] One such connection was drawn just a year after

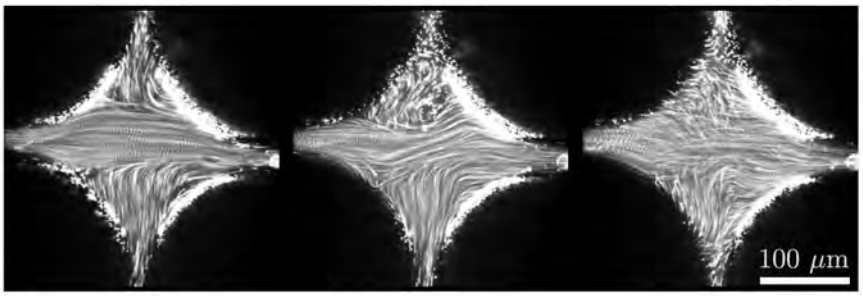

Figure 1.1: Imposed left-to-right flow of a polymer solution in a pore within a disordered 3D porous medium. Panels show increasing flow rate from left to right. Bright streaks show the motion of tracer particles; dark circles at the periphery show the solid grains comprising the solid matrix. At high flow rates, the flow becomes chaotic, with streamlines that continually fluctuate and cross.[3]

Feynman made his quip: by dissolving a dilute amount of flexible polymers into a viscous solvent, rheologists Georgii Vinogradov and V. Manin observed an unusual elastic analog to turbulence with striking visual similarity in its chaotic motion (Figure 1.1 gives an example from this dissertation).[11] Yet despite our capability to engineer with turbulence, few of the same mathematical tools have been translated to these other similarly chaotic flows.

In this dissertation, I attempt to translate some of this understanding from inertial turbulence to the unstable dynamic flow state that arises in polymer solutions. In particular, I have found that Vinogradov's elastic instability gives a similar type of fluid "memory" in porous media (chapter 2), and in disordered 3D porous media produces a flow state very reminiscent of Feynman's turbulence with an analogous increase in viscous dissipation, resolving an over-50-year-old puzzle[12] (chapter 3). Control of this excess resistance can then be leveraged to manipulate flow in geological settings (chapter 4), and engineer enhanced mixing in confined spaces (chapter 5). Polymer solutions thus provide a new avenue to steal ideas from turbulence and adapt them for new settings . Let us then understand these polymer solutions, and how exactly they produce this lucrative "elastic turbulence."*

1.1 Polymer solutions

What is the difference between a liquid and a solid? Perhaps trivially a liquid can flow while a solid remains rigid, but quick examples can easily confound this idea. Peanut butter in the jar is rigid until scooped, while the solid rock mantle of the earth convects continuously.

Still, peanut butter feels very different from a rock, and your intuition can rightly separate them along a spectrum of more liquid-like to more solid-like. Water is of course very liquid-like, and when perturbed it remains rigid only very briefly; namely, the time it takes for molecules to thermally rearrange which is about 1 picosecond (10^{-12} s), much too fast for any camera to record. The earth's mantle conversely is very solid-like, and rotates once every 10 million years, much too slow for any camera to record. Only for intermediate examples (peanut butter, jelly, silly putty, asphalt, glass) does our attention span as humans overlap with the speed of motion for us to notice a solid flowing over the course of a few minutes or years.

This spectrum that we have laid out goes from liquid to solid, based on a single material property that I have vaguely described as "time to flow". The nuances of this time scale (in

This chapter is based in part on a published review by Christopher A. Browne, Audrey Shih, and Sujit S. Datta. Pore-Scale Flow Characterization of Polymer Solutions in Microfluidic Porous Media. *Small*, 16(9):1903944, 2019. [1]

*Though sometimes the term "elastic turbulence" is reserved for unstable viscoelastic flows with specific scaling laws, [13] I will use it in this dissertation to simply refer to any chaotic polymer solution flow in the absence of inertia Re $\ll 1$, as is frequently done. [14,15]

reality a whole library of characteristics) occupy the entire field of rheology, but in a crude sense each material has a spectrum of "relaxation times"—of which generally the longest relaxation time λ dominates—describing how quickly the material relaxes to a fluid state after an initially rigid response to perturbation. Comparing this longest relaxation time to our attention span τ, we can define a dimensionless parameter the Deborah number that characterizes how "liquid-like" or "solid-like" a material behaves:

$$\mathrm{De} = \frac{\lambda}{\tau}. \tag{1.1}$$

For water $\lambda \sim 1$ ps but the fastest we can perceive changes is about $\tau \sim 0.01$ s, so $\mathrm{De} \sim 10^{-10}$, very small indeed indicating water appears liquid-like to us. Conversely, plate tectonics flow $\lambda \sim 1$ MA and our perception to geological change is at most our lifespan $\tau \sim 100$ yr, so $\mathrm{De} \sim 10^{4}$, very large indicating that rock formations appear solid-like to us.

Our interest rests in the middle of this spectrum on fluids that have *competing* timescales because of a blend of components with different relaxation times λ. Consider a ball of silly putty, which acts like an elastic solid during the impact of a bounce, but spreads into a puddle like a viscous liquid when left overnight. The novelty of silly putty is seen by stretching it on intermediate timescales (which by design overlap with the attention span of a child $\tau \sim 10$ s): the putty resists stretching like a rubbery elastic solid that somewhat retains a plastic solid-like shape, but also droops under gravity and thins like a viscous fluid. The origin of this behavior is that silly putty contains polymers: large, strand-like molecules that can bend, coil, and stretch—storing and releasing elastic energy much like microscopic rubber bands. The polymer chains coil and stretch slowly $\lambda_{\mathrm{polymer}} \sim 0.1$ s to 1 min, but the fluid they are dissolved in generally responds very quickly $\lambda_{\mathrm{solvent}} \sim$

1 ps, producing the competing timescales: the solvent is responding like a viscous liquid ($\mathrm{De}_{\mathrm{solvent}} = \lambda_{\mathrm{solvent}}/\tau \ll 1$) while the polymer is responding like an elastic solid ($\mathrm{De}_{\mathrm{polymer}} = \lambda_{\mathrm{polymer}}/\tau \gtrsim 1$), and the fluid as a whole thus exhibits viscous and elastic properties together (hence "viscoelastic"), giving rise to a host of intriguing flow behaviors.[16†]

You are likely familiar with many other viscoelastic polymer solutions in everyday life. The mucus linings of your digestive and respiratory tracts are "gooey" because of biologically produced polymers. Xanthan gum (among others) is frequently used to make gum chewey and give food pastes their rigidity. Nearly every shampoo, conditioner, lotion, and cosmetic has polymers (often polyethylene glycol/PEG, or wormlike micelles which behave in many ways like polymers) to make them hold their shape in your palm, but lather smoothly when rubbed into hair or skin. We will now quantify how these polymer additives modify the viscous resistance of a fluid to flow (§1.2), and modify the elastic flow structure (§1.3).

1.2 Viscosity and resistance to flow

Most fluids you interact with frequently are likely "Newtonian"; that is, fluids that follow Isaac Newton's simple theory of viscosity. The dynamic shear viscosity of a fluid μ describes its resistance to shearing flow: water has a low viscosity of $\mu = 0.89 \times 10^{-3}$ Pa · s, while honey has a much larger $\mu \sim 10^5$ Pa · s. For Newtonian fluids, this viscosity is a constant

[†] In general the solvent is always liquid-like $\mathrm{De}_{\mathrm{solvent}} \ll 1$, and we are only concerned with the timescale of the polymer λ.

material property.[‡] We can use the viscosity to compute the shear stress σ (Pa), which tells us a force per unit area that must be applied to drive a flow:

$$\sigma = \mu\dot{\gamma} \tag{1.2}$$

The shear rate $\dot{\gamma}$ (s^{-1}) describes how quickly the fluid is being moved . For Newtonian fluids, this shear stress is the only stress providing flow resistance. We can similarly compute an energy dissipation rate Φ (or "dissipation function"[17]), which describes the power that must be applied (per unit volume) to maintain the flow:

$$\begin{aligned}\Phi &= \sigma\dot{\gamma} \\ &= \mu\dot{\gamma}^2\end{aligned} \tag{1.3}$$

This can then be used to describe the power or energy expenditure to maintain a flow. For example, honey has a rather high Newtonian viscosity of $\mu = 10,000$ mPa · s (compared to water at 1 mPa · s): to squeeze honey out of a bottle, you will apply a pressure to the bottle to expel fluid. The fluid speeds up as it enters the nozzle—let's say to a velocity $U_s = 5$ cm/s through a $D = 5$ mm diameter and $L = 3$ mm deep nozzle (volume 59 mm^3), creating a characteristic shear rate of $\dot{\gamma} \approx 3U_s/D = 50\ s^{-1}$ (Fig. 1.2). The viscous dissipation of macroscopic mechanical energy into heat is what your hand feels as resistance; in this case with a dissipation function $\Phi \approx 270$ kPa/s and a power dissipation of $P \approx \Phi V \approx 1500$ W (similar to the consumption of a light bulb). For 1 mL of honey

[‡]Constant with shear rate $\dot{\gamma}$, though it is generally a strong function of temperature T. In this dissertation, we never consider changes in temperature, and all data are presented at roughly lab temperature $T \approx 23°$.

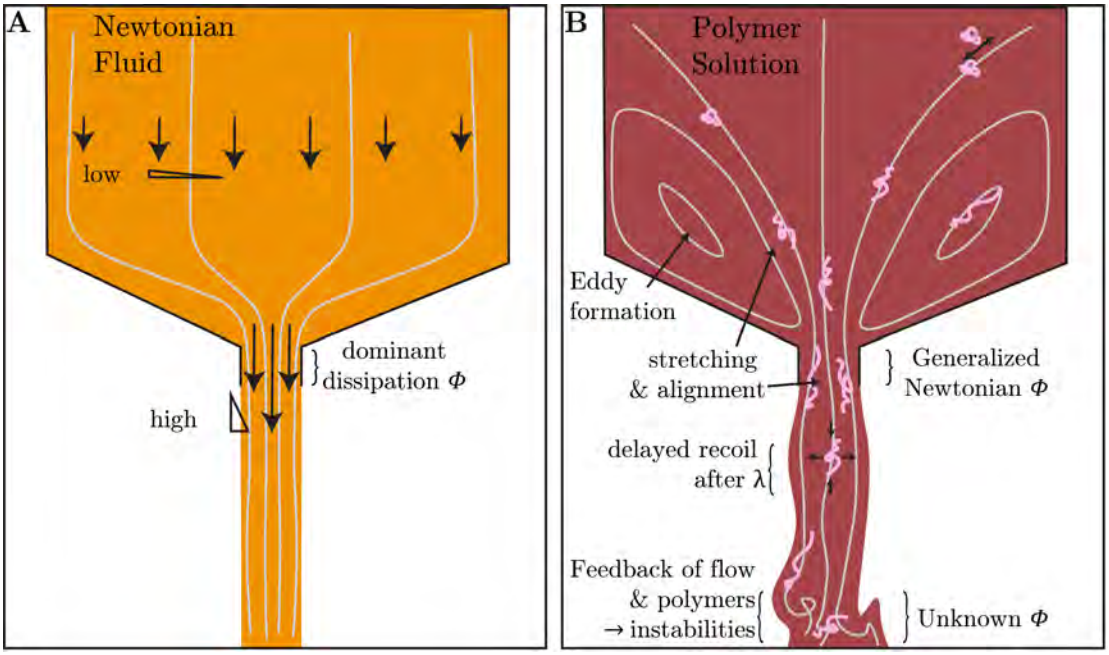

Figure 1.2: Schematic of flow exiting a nozzle. A Newtonian fluids have a parabolic velocity profile, which speeds up in the nozzle provide a high shear rate that dominates the viscous dissipation, and hence power required to drive the flow. **B** Polymer solutions have a modified dissipation in the nozzle because of shear-thinning, which can be captured by a generalized Newtonian model. However, alignment of polymer chains and elastic recoil of polymers can modify other parts of the flow, leading to eddy formation upstream of the constriction and in some cases elastic instabilities, with unknown consequences for energy dissipation.

this will be a net energy consumption of $\approx$ 0.00004 Cal (compared to the of $\approx$ 3 Cal of caloric energy contained in the honey). More accurately we should integrate this dissipation function $P = \int_{\mathcal{V}} \Phi \mathrm{d}V$, which yields a more correct answer $1.2\times$ higher than our quick estimate.

This power consumption changes for a *polymer solution*: for example if you want to squeeze ketchup from the same nozzle. Immediately our first equation is wrong, because the stress is not simply linear with the shear rate $\sigma \neq \mu\dot{\gamma}$, nor is the dissipation function given so clearly by the stress $\Phi \neq \sigma\dot{\gamma}$. Instead, the stress required to flow depends not only on the shear rate, but also the conformations of the microscopic polymer chains. This gives

them a nonlinear shear stress and and additional elastic stress, both of which can greatly modify the flow.

First, the shear stress σ which we are already familiar with is altered for polymer solutions, because the polymers *viscosify* the fluid. The existence of large polymer chains, which generally exist as coiled up balls with a characteristic radius R_g (radius of gyration) create extra friction as they pass over each other in flow, converting more macroscopic mechanical energy into heat through viscous dissipation. However, as we squeeze this ketchup from the bottle, the long polymer molecules will stretch and align as the flow speeds up towards the nozzle (Fig. 1.2). This alignment allows the chains to slip past each other easier, effectively *reducing* this viscosifying effect of the polymers: so our ketchup becomes relatively easier to flow the harder we push on the bottle, as you can confirm yourself: this decrease in flow resistance is similarly why it is so common to accidentally dispense too much ketchup on your food.[18] The viscosity of a polymer solution is thus not always a constant, but rather can decrease with shear rate, and we give this polymer solution viscosity a new symbol η instead of μ to remind ourselves that it is not a constant (Orange line in Fig. 1.3). For arbitrarily small shear rates this will plateau to a maximum viscosity set by the undisturbed polymer coils (zero-shear viscosity η_0), and at very high shear rates this will plateau to a minimum at the viscosity of the background Newtonian solvent (μ, or sometimes η_s). In between these bounds, the viscosity generally follows a sigmoidal shape described by the Carreau-Yasuda model,[19,20] which for moderate shear rates can be simplified conveniently to a power-law decay $\eta \sim \dot{\gamma}^{\alpha_s - 1}$, where $0 < \alpha_s \leq 1$ and $\alpha_s \approx 1$ corresponds to no shear-thinning. The power dissipation function associated with this modified shear viscosity might then look like $\Phi_S = \eta(\dot{\gamma})\dot{\gamma}^2$, quite similar to the dissipation function for

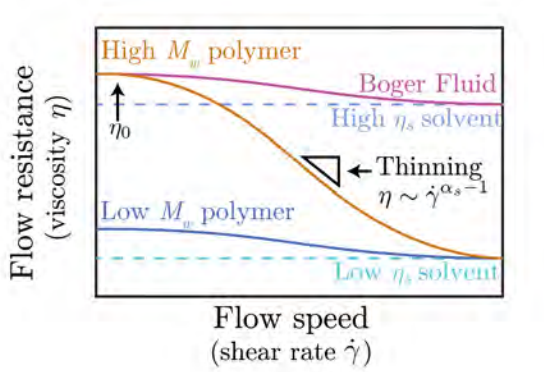

Figure 1.3: Schematic of viscous flow resistance for representative polymer solutions. Newtonian solvents have a viscosity that is constant with shear rate (dashed lines), but polymer solutions the viscosity changes. At low shear rates, the polymer elevates the viscosity (plateaus on left side): this is more pronounced for high M_w polymers (orange) and less pronounced for low M_w polymers (blue). At higher shear rates this viscosity drops off, following a power law for a bit before plateauing again at the viscosity of the background solvent. A special case "Boger" fluid is made by dissolving a high M_w polymer in a high viscosity solvent, so the the polymer is highly elastic, but the magnitude of shear thinning is not very noticeable: these solutions are useful for isolating elastic effects for modeling in the lab.

the Newtonian fluid in Eq. 1.3, but now $\eta(\dot{\gamma})$ is a function that depends on the polymer molecular weight M_w and concentration c as well as the solvent viscosity η_s. Because of this similarity in the dissipation function Φ_S and the shear stress σ to the Newtonian counterparts, this framework for describing polymer solutions is called a "generalized Newtonian" approach.

This viscosifying effect has proved valuable for for engineers to design a host of fluids. You may use flour or cornstarch (fairly rigid high molecular weight biopolymers) to thicken gravy—and if you stir gravy fast enough you may notice shear thinning. Similarly, your body generates mucins (flexible high molecular weight biopolymers) to thicken the water lining your digestive and respiratory tracts into a viscous mucus—you can similarly notice that mucus feels thick in your throat and nostrils, but thins nearly to water during the high shearing action of a sneeze. A range of other household cosmetics, detergents, and prepack-

aged foods similarly use polymers essentially as a cheap way to add viscosity.

Industrial processes also take advantage of this viscosifying effect, and in the 60's polymer additives found use in the oil and gas recovery industries. During oil and gas recovery, a flooding fluid (water plus dilute additives) is injected into a subsurface reservoir to push out the trapped resource. These reservoirs are typically dense porous packings of water-wet soil, rock, and mineral grains, and look much like a sponge or a packing of sand. Dilute solutions of low molecular weight polymers were at first used simply to suppress fingering instabilities during injection and thereby maintain flow uniformity during fluid recovery.[21,22] However, EOR field tests with high molecular weight polymers often yield unexpectedly high recoveries of oil fluid far beyond what is expected from a simple viscosifying effect.[23–28] These findings have prompted the use of high molecular weight polymer solutions for groundwater remediation as well, where a flooding fluid is similarly used to displace contaminants from a subsurface aquifer.[29–32]

What induces this vast improvement in recovery? In 1967, rheologists Marshall and Metzner made a surprising report: despite the polymer solutions being shear-thinning (η *decreases* with shear rate $\dot{\gamma}$), inside of a porous medium the resistance to flow suddenly *increases*—sometimes by over 30×.[12] For clarity this apparent resistance observed in a porous medium—but not in bulk solution—is given a new symbol for an "apparent" viscosity η_{app}, which is thus a function of not only the polymer solution properties (M_w, c, η_s) but also the confining geometry of the porous medium.

The immediate hypothesis for this unusual behavior is the accumulation of elastic memory, which can modify the base flow or dissipate energy through an extensional viscosity (described below).[33–38] However, challenges in rheology and an inability to image the flow

in these opaque porous media have prevented quantification of these competing hypotheses. Thus, broad application is still limited by an incomplete understanding of how these macroscopic variables depend on the pore-scale features of the fluid flow, which in turn depend on polymer properties, pore space geometry, and imposed flow conditions. As a result, the mechanisms underlying polymer solution-enhanced fluid recovery are still widely debated,[1,34–36,39–44] and general principles for predicting and controlling the flow are lacking. In this dissertation, by directly imaging the flow in situ, we can begin to test these hypotheses directly for the first time.

1.3 Elastic flow effects

In addition to this modified viscosity, polymers are *elastic*. Entropy drives polymers to a compact coiled state, often visualized as a ball with radius R_g (radius of gyration). When subjected to a steady extension rate $\dot{\varepsilon}$ (or shear rate $\dot{\gamma}$), the polymer can stretch to an equilibrium length L_{eq} (Fig. 1.5), as we imagined the polymers in our ketchup doing in the extensional flow of the nozzle constriction. This stretched state usually plateaus a bit below the contour length $\sim 0.85L_c$,[45,46] where all molecular bonds would be in their most extended trans conformations. For high molecular weight polymers, this transition becomes sharper and nonlinear, can even double over to produce a hysteretic "switch" between the coiled and stretched conformations (coil-stretch transition) in extensional flows $\dot{\varepsilon}$.[47] In shear flows, high molecular weight polymers instead exhibit a periodic tumbling motion, with regular intervals of stretching, rotating, and recoiling.[48,49] When combined

with streamline curvature, this elastic stress produces a hoop stress, which drives the polymer to compress and travel toward the center of flow curvature, analogous to centripetal motion. This hoop stress is the reason that cake batter will climb up the rods of electric mixers ("rod climbing"). In geometries with contractions, polymers align to minimize these hoop stresses in the corners, leading to the formation of large upstream recirculating eddies (Figure 1.2).[50–54]

In a shear rheometer, this hoop stress can be measured as a normal stress on the rheometer plate or cone, and hence we can estimate the elastic stresses at a given shear rate $\dot{\gamma}$ using the first normal stress difference $N_1(\dot{\gamma})$, which is also a nonlinear function of shear rate and generally most pronounced for high molecular-weight polymers in viscous solvents (an example used in this dissertation is shown in figure 1.4)[19,20]. More sophisticated methods are being developed to discern the dependence of these stresses on extension rate $\dot{\varepsilon}$ as well,[55–64] but for simplicity we shall use characteristic shear rates $\dot{\gamma}$ to estimate these stresses. The relative roles of these viscous liquid-like stresses and elastic solid-like stresses are quantified by the dimensionless Weissenberg number:

$$\mathrm{Wi} \equiv \frac{N_1(\dot{\gamma})}{2\sigma(\dot{\gamma})}. \tag{1.4}$$

The factor of 1/2 arises from the Oldroyd-B constitutive model; some researchers omit this factor for simplicity, to obtain an order-of-magnitude estimate. An alternative Weissenberg number $\lambda\dot{\gamma}$ is also frequently used. In this dissertation, we will recast changes in flow rate Q or shear rate $\dot{\gamma}$ using the above definition.

This high-energy stretched state requires hydrodynamic stress supplied by the extensional or shear flow to maintain the chain under tension: once the extensional or shear flow

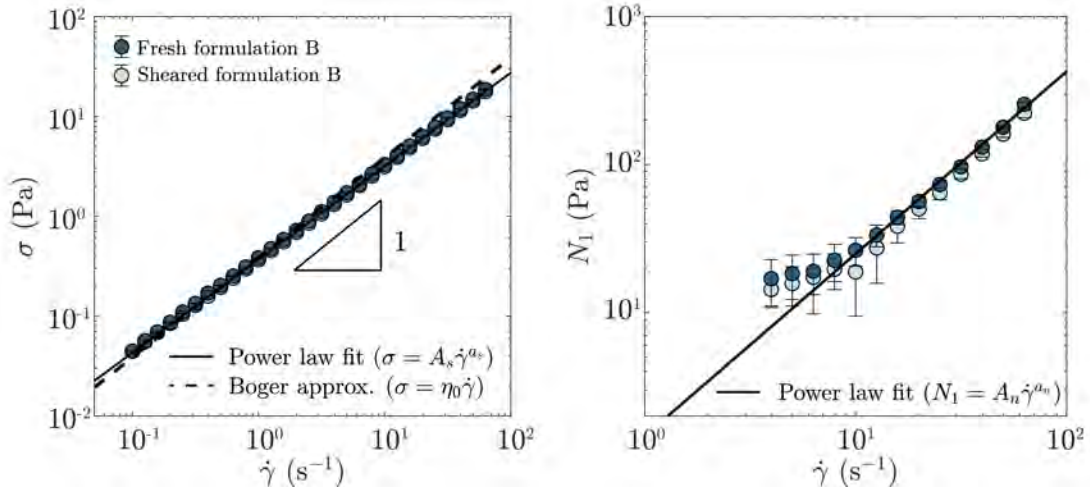

Figure 1.4: Viscous and elastic stresses of example polymer solution in this dissertation under constant shear flow $\dot{\gamma}$. Formulation B used in this dissertation, described further in §A.1

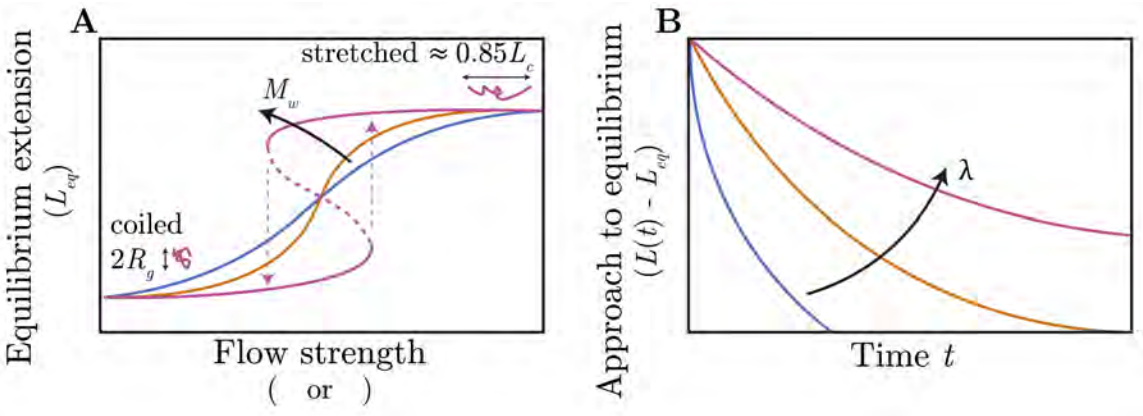

Figure 1.5: Chain extension dynamics A: Equilibrium polymer chain length increases with applied shear rate or extension rate. For high molecular weight polymers, this can eventually give a sharp hysteretic coil-stretch transition during extension $\dot{\varepsilon}$ (purple line) or periodic tumbling during shear $\dot{\gamma}$ (not pictured).[48,49] **B** Polymer chains approach this equilibrium conformation exponentially in time, both in relaxation λ_{rel} and extension λ_{ret}, though these times are often similar and given simply by λ.

stops, the chains will release the elastic energy and relax back to R_g and release this elastic energy. However, these elastic stresses do not build up or release instantaneously. Instead, polymer molecules stretch slowly over a retardation time λ_{ret} and recoil with a relaxation time λ_{rel} (though often these times are assumed to be similar $\lambda \approx \lambda_{\text{ret}} \approx \lambda_{\text{rel}}$) (Fig. 1.5). Detailed work has linked this molecular time scale to the relevant macroscopic time scales one would choose to define De as above (§1.1).[47,65–75] These time scales are often on the order of seconds, and the polymers can be transported by the background flow (advected) faster than they can respond. In particular, when $\text{De} = \lambda\dot{\gamma} \gtrsim 1$ as we defined at the beginning, we have these competing timescales that give viscoelasticity. From a molecular perspective, the polymers are "out of sync" with the local flow, producing a molecular fading-memory that can give the fluid spatial or temporal dynamics. For example, our ketchup will swell a little when it exits the nozzle (dye swell) and toothpaste will spring back into the tube when released (elastic recoil), among other interesting effects (tubeless siphoning)[16].

Finally, in addition to these *steady* (in time) elastic effects, the fading memory of polymer molecules can produce *unsteady* or transient flow effects when strong viscoelasticity is combined with strong streamline curvature $\mathscr{R}$. These instabilities will quantitatively occur when (i) the deformation of the fluid $\dot{\gamma}$ can build up sufficient elastic stresses to overwhelm the dissipating viscous stresses $\text{Wi} \equiv N_1/(2\sigma) \gtrsim 1$; and (ii) these elastic stresses are retained through polymer memory λ during advection U over curved streamlines $\mathscr{R}$ long enough for the elastic stress to be retained as a destabilizing hoop stress $\text{De} \equiv \lambda U/\mathscr{R} \gtrsim 1$. Hence, a linear stability analysis of the Stokes equation for a viscoelastic fluid indicates that the flow becomes unstable when $\text{M} \equiv \sqrt{2\text{Wi} \cdot \text{De}}$ exceeds a threshold,[76,77] which has been empirically found to be $\text{M}_c \approx 6$ to 12 in a range of model geometries.[78,79] This elastic insta-

bility produces a self-sustained[14] chaotic fluctuating flow state, displaying no characteristic spatial or temporal scale.[13,80] This elastic instability thus shares a striking visual similarity with turbulent flows, despite the low Re $\ll 1$ prohibitive for turbulence, prompting Vinogradov and Manin's to term the flow state "elastic turbulence."[11] Though a similar instability arises in a range of shear rheometers and serpentine channels, the structure and magnitude of fluctuations depends sensitively on the confining geometry.[14,76,77,79–85] It thus remains unknown how this instability arises—if at all—in a tortuous, disordered pore space, where polymers may retain memory between successive contractions and expansions of each pore (Figure 1.6).

1.4 Polymer flow in porous media

How then can these elastic flow effects, and potentially elastic instabilities, lead to the puzzling anomalous increase in flow resistance observed in porous media, but not simple shear flows? The porous media relevant to EOR and groundwater remediation are typically dense packings of water-wet soil, rock, and mineral grains. The resulting pore spaces are highly heterogeneous and tortuous, with successive contractions and expansions known as pore throats and pore bodies, respectively; the pore throat diameters L_t typically range from $\sim$ 100 nm to 10 μm while the pore body diameters L_b are typically $\approx$ 2 to 5 times larger (Figure 1.6 and accompanying table). During injection, a polymer solution is forced to flow through this pore space. The interstitial injection speed $U \equiv Q/\varphi A$, where $\varphi \approx 0.1$ to 0.4 is the medium porosity, is limited by the ability to apply a sufficiently large fluid pressure

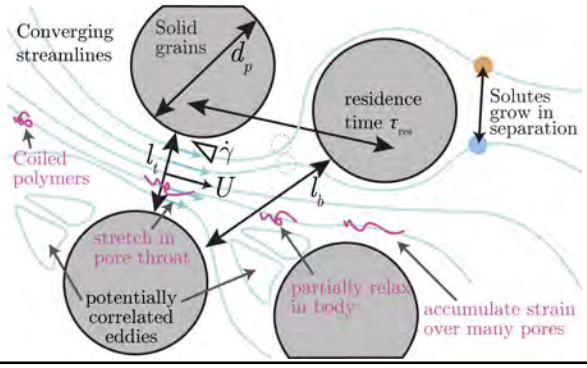

Parameter	Range
Pore throat diameter $l_t \approx 0.16 d_p$	0.1 to 10 μm
Pore body diameter $l_b \approx 0.24 d_p$	0.2 to 50 μm
Fluid viscosity η	10^{-3} to 10^{-1} Pa·s
Interstitial flow speed U	10^{-2} to 10^{2} μm/s
Shear rate $\dot{\gamma} \sim U/l_t$	10^{-3} to 10^{3} s^{-1}
Pore residence time $\tau_{res} \sim l_b/U$	2×10^{-3} to 5×10^{3} s
Polymer relaxation time λ	10^{-2} to 10^{2} s

Figure 1.6 & Table 1.1: Flow in a porous medium. Solid grains of diameter d_p give pore bodies (expansions) a_b and pore throats (constrictions) a_t. Dispersion within the medium causes initially close solutes (orange and blue dots) to continually separate as they are advected along laminar streamlines. Fluid moving with characteristic velocity U creates a shear rate $\dot{\gamma}$ with the solid grain walls, which stretches polymers in the constrictions (pore throats), but only can partially relax in the expansions (pore bodies) due to their nonzero relaxation time λ over the finite pore residence time τ_{res}, which can lead to accumulated extension (Hencky strain ε) over the course of many pores.

drop; thus, interstitial flow speeds typically range between $\sim$ 0.01 and 100 μm/s.[44,86] We summarize these pore-scale parameters in Table 1. Under these conditions, inertia is always absent Re $\equiv \rho U L_t/\eta$ ranges from $\sim 10^{-11}$ to $10^{-3} \ll 1$, and Newtonian fluids thus exhibit laminar, steady-state flow. By contrast, polymer solutions applied in EOR and groundwater remediation can have M ranging from $\sim 10^{-6}$ to 10^{6}, indicating that unstable flow might be able to arise in many of these cases (Table 1.2). However, direct visualization of elastic turbulence in 3D porous media has been precluded by the opacity of typical porous media, and until this thesis, visualizations are limited to 2D models of porous media.

Parameter	Definition	Interpretation	Range
Reynolds	$\mathrm{Re} \equiv \rho U L_t / \eta$	inertial stress / viscous stress	10^{-11} to 10^{-3}
Weissenberg	$\mathrm{Wi} \equiv N_1 / 2\sigma \approx \lambda \dot{\gamma}$	elastic stress / viscous stress	10^{-5} to 10^{5}
Deborah	$\mathrm{De} \equiv \lambda / \tau_{res}$	polymer relaxation time / residence time	2×10^{-6} to 5×10^{4}
Capillary	$\mathrm{Ca} \equiv \eta U \varphi / \gamma$	pore-scale viscous stress / capillary pressure	10^{-10} to 10^{-3}

Table 1.2: Table of key dimensionless parameters characterizing polymer solution flow in porous media. ρ is the fluid density, U is the interstitial flow speed, L_t is the pore throat diameter, η is the fluid shear viscosity, N_1 is the first normal stress difference, σ is the shear stress, λ is the polymer relaxation time, $\dot{\gamma}$ is the shear rate, τ_{res} is the polymer residence time in a pore, φ is the medium porosity, and γ is the aqueous-nonaqueous fluid interfacial tension.

Nevertheless, a broad body of work in 2D microfluidics over the past 20 years has demonstrated that the velocity field is characterized by large eddies with a broad spectrum of spatial and temporal fluctuations that depend on the polymer solution and contraction/expansion geometry.[1,87–98] The simplest model of a pore is a single abrupt constriction. A flowing polymer solution forms large eddies upstream of a constriction above a threshold value of M. While reminiscent of the steady eddies formed by rigid and elongated polymers, these eddies fluctuate strongly in time.[87] The eddy size and asymmetry increases non-linearly with Wi and with increasing contraction ratio L_t/L_b,[88,91,92,95,99–101] though a universal relationship has not been established. Interestingly, the presence of inertia $\mathrm{Re} \gtrsim 1$ suppresses temporal fluctuations of these eddies, and promotes symmetry in their structure.[54,102]

Flow through a pore is often represented instead by flow impinging on a channel-centered cylinder. Single-molecule imaging of fluorescently-labeled DNA provides evidence that polymers are stretched and have hysteretic conformations as they flow around the cylinder[73] in a manner similar to coil-stretch hysteresis. Thus, similar to the case of flow through a constriction, upstream eddies form during polymer solution flow around a cylinder in a narrow channel, growing in size and becoming unstable as Wi increases; intriguingly, the

vertical location of the eddy can exhibit discrete switching between the top and bottom walls of the channel,[97] suggesting a possible connection to bistable polymer conformations, which we explore in chapter 2 of this dissertation.

Real-world porous media are typically composed of many interconnected pore expansions and contractions. To more closely mimic this geometry, experiments have investigated polymer solutions flowing through channels with multiple constrictions, channel-centered pillars, and undulating walls arranged in 1D or in 2D arrays. Results obtained for ordered 1D arrays of pores in channels of narrow widths consistently demonstrate the formation of unstable eddies upstream of constrictions, similar to the case of a single constriction.[89,93,94,103–107] Because polymer stretching is hysteretic and can persist over large length scales,[85] polymer elongation may be retained across multiple pores. This "memory" may therefore provide new spatial structure to the flow over macroscopic scales in a porous medium. Studies of ordered 1D arrays are beginning to reveal such effects. For example, decreasing the distance between pillars in a narrow channel produces stronger fluctuations at similar values of Wi;[94] conversely, in a wider channel, the wake formed downstream of a first cylinder can merge with the wake formed downstream of a second.[96] Chapter 2 of this dissertation studies the role of this polymer memory in successive expansions and contractions of a model porous medium, demonstrating how a novel bistability can arise when polymer memory can persist during advection between pores $\lambda \gtrsim Ul_s$.

This complex coupling between pores also manifests in 2D arrays, showing flow behavior that can differ strongly from the 1D case. For example, polymer solutions flowing through ordered 2D arrays show strong velocity fluctuations throughout the pore space—but eddies are never observed.[44,108] Intriguingly, in other studies of flow through ordered

2D arrays of circular, square, and triangular pillars, large triangular 'dead zones' form on the upstream faces of the pillars; these dead zones are characterized by strong polymer compression and elongation, but unlike eddies, they show no apparent recirculation.[109,110] These dead zones periodically grow and disappear; moreover, the frequency of this process increases further downstream along the porous medium, indicating that coupling between pores influences the flow.[111] Consistent with these observations, the temporal variation in pressure measurements increases downstream along ordered 2D arrays of circular pillars, suggesting that instabilities grow spatially.[103,112] Combining such flow visualization to measurements of the overall pressure drop provides a way to directly link flow structure to macroscopic flow resistance. Such measurements show a dramatic increase in macroscopic flow resistance—mimicking the increase in η_{app} observed in bulk porous media—at the onset of unstable flow.[44,106,113,114] Simulations in model porous geometries can also capture the onset of flow fluctuations[115–117] and the associated increase in flow resistance.[114,118,119] These recent findings thus suggest the possibility that the striking increase in polymer solution flow resistance measured in bulk porous media reflects the onset of unstable flow.

Real-world porous media, however, are typically disordered: the pore sizes and spacing between grains are not uniform. While the majority of experiments and simulations have focused on studying polymer solution flow in ordered arrays, ongoing work is beginning to reveal that structural disorder can dramatically impact flow behavior. For example, flow visualization in 2D arrays of circular pillars shows that while a highly unstable flow state arises in an ordered medium due to sustained polymer elongation, velocity fluctuations are nearly completely suppressed in a disordered array, suggesting that elastic turbulence cannot arise in inherently disordered 3D media.[15] However, other results show the opposite

effect, suggesting that the onset of elastic turbulence in disordered media is sensitive to the particular geometry considered.[120] Hence, while microfluidic experiments in 2D arrays in many ways help guide our understanding of polymer solution flow, the increased dimensionality, tortuosity, connectivity, and disorder of real 3D porous media likely play crucial roles that remain unmodeled. To fill this gap in knowledge, in chapter 3 of this dissertation we fabricate transparent model 3D disordered porous media and directly image the flow in situ. We find that elastic turbulence does indeed arise, but at a different onset Wi_c in each pore—likely linked to the disordered geometry of individual pores. Guided by these findings, we quantitatively establish that the energy dissipated by unstable pore-scale fluctuations generates the anomalous increase in flow resistance through the entire medium through a dissipation function χ very analogous to the dissipation function observed in inertial turbulence Φ'.[§] Our results thus help to resolve this longstanding puzzle.[12]

Finally, we will explore structurally heterogeneous porous media, like those found in many environmental applications, such as remediation of contaminated groundwater aquifers,[32,122] recovery of oil from subsurface reservoirs,[21,123] and extraction of heat from geothermal reservoirs.[124] These media are often vertically-layered by strata of distinct permeabilities—leading to uneven partitioning of flow across strata, which can often be undesirable. In chapter 4, we use direct in situ visualization to demonstrate that elastic turbulence can generate chaotic spatiotemporal fluctuations and excess flow resistance in individual strata. In particular, we find that this instability arises at lower imposed flow rates in higher-permeability strata, diverting flow towards lower-permeability strata and helping to homogenize the

[§]The unstable dissipation functionΦ'[17] or equivalently the turbulent kinetic energy dissipation ε.[121] We avoid use of symbol ε to avoid overlap with the Hencky strain, which is typically given the same symbol, and use of the term kinetic energy dissipation, since in our low Re flows it is dissipation of mechanical energy.

flow. Guided by the experiments, we develop a parallel-resistor model that quantitatively predicts the flow rate at which this homogenization is optimized for a given stratified medium, providing a new approach to homogenize fluid and passive scalar transport in heterogeneous porous media.

Chapter 5 of this dissertation will report some ongoing work to generalize these findings to polymer solutions at different concentrations c and explore how the chaotic fluctuations can generate elevated pore-scale mixing of solutes. The appendix A gives details materials and methods that will be useful for replicating and building upon this work.

Memory is an illusion, nothing more. It is a fire that needs constant tending.

Ray Bradbury, A Pleasure to Burn

2

Chaos and memory

Elastic turbulence is driven by polymer memory, which allows molecules to retain elastic hoop stresses as they are advected over curved streamlines long enough to destabilize the laminar flow. This requisite streamline curvature can be produced by a single obstruction or constriction—both of which provide a similar mixed extensional-shear

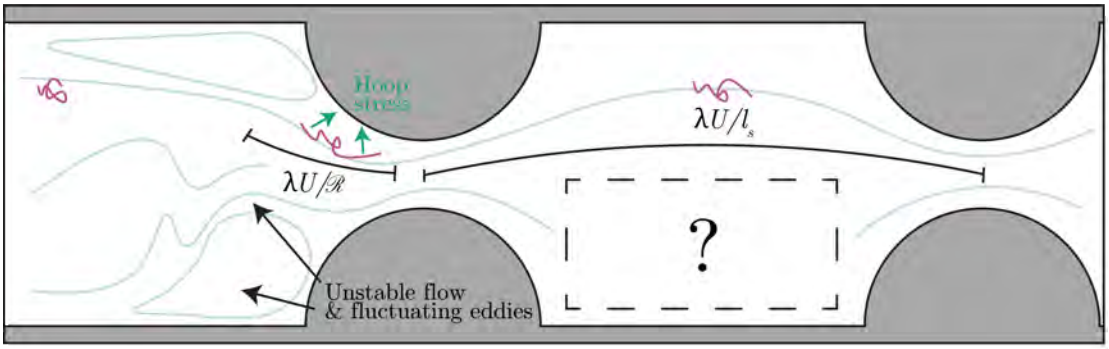

Figure 2.1: Schematic of unstable flow through successive contractions and expansions of a model 2D porous medium. In single contraction, unstable flow and fluctuating eddies appear above threshold value of $\mathcal{M}$, related to retention of polymer memory λ during advection U over streamlines of curvature $\mathscr{R}$. For successive contractions, it is unknown how polymer memory during advection over the pore separation distance l_s alters the flow structure.

flow with strong streamline curvature curvature $\mathscr{R}$ (Fig. 2.1). In these geometries, polymer chains are aligned and elongated by the flow, generating upstream recirculating eddies that minimize the extensional stress associated with chain misalignment.[50–54] Previous work has also shown when elastic turbulence arises in such single-constrictions.[87–97] In particular, this instability arises for sufficient polymer memory over streamline curvature $\mathrm{De} = \lambda U/\mathscr{R}$ and sufficient elastic stresses $\mathrm{Wi} = N_1/(2\sigma)$, giving the onset condition $\sqrt{2\mathrm{Wi}\cdot\mathrm{De}} > \mathrm{M}_c \approx 6$ to 12.

However, real porous media are comprised of not one but *many* successive constrictions and expansions. Imaging of flow through one-dimensional (1D) arrays of *widely-spaced* pore throats consistently demonstrates the formation of unstable eddies upstream of each throat, similar to the case of an isolated throat.[89,93,103–106] By contrast, when the spacing

This chapter has been adapted from published work by Christopher A. Browne, Audrey Shih, and Sujit S. Datta. Bistability in the unstable flow of polymer solutions through pore constriction arrays. *the Journal of Fluid Mechanics*, 890, 2020.[2] **Author Contributions:** C.A.B. performed all experiments; C.A.B. and A.S. performed the image processing; C.A.B. and S.S.D. designed the experiments, analyzed the data, discussed the results, and wrote the manuscript. S.S.D. designed and supervised the overall project.

between pore throats is small, chain elongation may persist across multiple pores as the polymers are advected through the pore space. Thus, memory of strain in one pore may influence the flow in a pore further downstream, potentially providing new spatio-temporal structure to the flow. However, this possibility remains to be explored. Studies conducted at a Reynolds number $\mathrm{Re} \sim 20$ and an Elasticity number $\mathrm{El} \equiv \mathrm{Wi}/\mathrm{Re} \sim 1$, and thus also subject to inertial effects, show that decreasing the spacing between pores produces stronger flow fluctuations[94]—providing a clue that polymer memory may indeed influence the flow. Nevertheless, whether and how polymer memory impacts flow through a porous medium has not been fully resolved for the case of $\mathrm{Re} \ll 1$ and $\mathrm{El} \gg 1$, in which elastic effects dominate and inertial effects do not also arise. This flow regime is particularly relevant to key applications including oil recovery and groundwater remediation, which can have Re ranging from $\sim 10^{-11}$ to 10^{-3} and El ranging from $\sim 10^{2}$ to 10^{11}.

Thus, this chapter will address **the role of polymer memory** over the course of successive expansions and contractions of a porous medium for elasticity-dominated flows ($\mathrm{Re} \ll 1$ and $\mathrm{El} \gg 1$). We accomplish this by directly imaging the flow with confocal microscopy in 1D ordered arrays of pore constrictions, enabling us to systematically tune this pore-to-pore memory by varying the pore separation distance l_s. When the spacing between pores is large, unstable eddies form upstream of each throat, similar to observations of an isolated throat (§1.3). By contrast, when the spacing between pores is sufficiently small, the flow exhibits a surprising *bistability*. In each pore body, the flow persists over long durations in one of two distinct flow states: an eddy-dominated state in which a pair of large unstable eddies forms in the corners of the pore body, and an eddy-free state in which strongly-fluctuating fluid streamlines fill the entire pore body and eddies do not

form. We hypothesize that this unusual behavior arises from the interplay between flow-induced polymer elongation, which promotes eddy formation, and relaxation of polymers as they are advected between pores, which enables the eddy-free state to form. Consistent with this idea, we find that the flow state in a given pore persists for long times. In addition, we find that the instantaneous flow state is correlated between neighboring pores; however, these correlations do not persist over long times. Thus, our results reveal that the characteristics of unstable flow are not determined just by injection conditions and the geometry of the individual pores, but also depend on the spacing between pores. Ultimately, these results help to elucidate the rich array of behaviors that can arise in polymer solution flow through porous media.

2.1 Materials and Methods

The void space of a porous medium is typically composed of successive expansions known as pore bodies connected by narrower constrictions known as pore throats.[125–128] We use 3D stereolithography (SLA) printing to make model porous media that recapitulate these geometric features (Appendix A.2).[8] Importantly, this approach provides precise control over the pore space geometry, and yields devices that can be optically interrogated while also withstanding the high pressures that arise during elastic polymer solution flow.

The media are made of straight, square channels, with constrictions defined by evenly-spaced hemi-cylindrical posts shown in Figure 2.2. For simplicity, this geometry thus does not incorporate complex pore space tortuosity and connectivity; instead, it provides a way

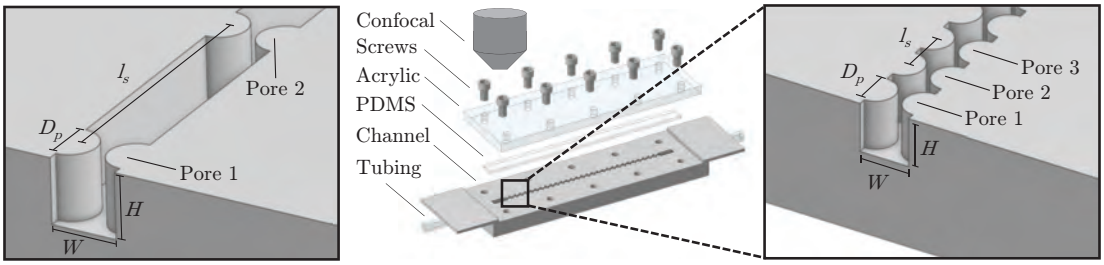

Figure 2.2: Experimental setup. Fluidic channel contains pore throat constrictions defined by opposing hemi-cylindrical posts and is fabricated using a stereolithographic 3D-printer. Dimensions are $W = 2$ mm, $H = 2$ mm, $D_\mathrm{p} = 1.6$ mm. We vary the pore throat separation distance l_s and the number of throats in the channel (two examples are shown in the left and right panels). The channel is screwed shut with an acrylic plate over a thin strip of PDMS. Inlet and outlet tubing is glued into 3D-printed holes. The setup is inverted and videos are captured on a confocal microscope; middle panel is vertically flipped for clarity.

to isolate and systematically probe the role of pore spacing on flow behavior. Each channel is $W = 2$ mm wide, $H = 2$ mm high, and 7 cm long, with opposing posts of diameter $D_\mathrm{p} = 1.6$ mm that are laterally separated by $L_\mathrm{c} = 0.4$ mm and spaced by a center-to-center distance of l_s along the flow direction. The space between hemi-cylinders along the flow direction thus defines the pore bodies, while the lateral constriction between opposing hemi-cylinders defines the pore throats. Varying l_s provides a way to systematically test the influence of pore spacing on the flow. To probe the effects of polymer memory, we compare an isolated pore throat with $l_\mathrm{s} \to \infty$, a pair of widely-separated throats with $l_\mathrm{s} = 16W$, and an array of closely-separated thirty throats with $l_\mathrm{s} = 1W$.

To fabricate each device, we 3D-print the open-faced channel with a FormLabs Form 2 stereolithography printer, using a proprietary clear polymeric resin (FLGPCL04) composed of methacrylate oligomers and photoinitiators. We then glue inlet and outlet tubing directly into 3D-printed connectors designed to minimize perturbation of the polymers away from the pores. Finally, as shown in figure 2.2, the whole assembly is screwed shut using a clear acrylic sheet laser-cut to size and placed on top of a thin strip of polydimethyl-

siloxane (PDMS), which provides a water-tight seal (§A.2).

Our polymer solution is a dilute ($C = 300$ ppm $\approx 0.3C^*$) solution of hydrolyzed polyacrylamide (HPAM) in water (10 wt.%) and glycerol (89 wt.%) with 1 wt.% NaCl (Formulation A in §A.1). We inject our polymer solution through the porous medium at a fixed volumetric flow rate Q using a syringe pump and begin imaging well after a time of $\approx 300 \left(D_\mathrm{p} WH - \pi D_\mathrm{p}^2 H/4 \right) /Q$, after which the flow reaches a dynamic equilibrium in which the statistical properties of the flow do not appreciably change (§A.2.1). We invert the setup and image the flow at the channel mid-plane using a resonant line scanning confocal microscope (§A.2.2). To visualize the flow we disperse 1 ppm of fluorescent 1 μm polystyrene tracer particles, and average successive frames for $10\tau_\mathrm{pv}$, yielding the micrographs shown in figures 2.3, 2.5, 2.6, 2.7, and 2.8. The particles can be considered faithful tracers of the streamlines because tracer particle advection dominates over diffusion, as described by the particle-scale Péclet number $\mathrm{Pe} \equiv (Q/A)D_p/\mathcal{D} > 10^5 \gg 1$, where $\mathcal{D} = k_B T/3\pi\eta_0 D_t = 6 \times 10^{-3}$ $\mu\mathrm{m}^2/s$ is the Stokes-Einstein particle diffusivity. We thus refer to the particle pathline measurements as fluid streamlines throughout this chapter.

The channel dimensions and polymer concentration used in our experiments enable us to isolate the influence of polymer elongation and relaxation between pores, with a minimal influence of polymer surface adsorption, flow-induced chain migration, wall slip, shear banding, and polymer entanglement. As described further in appendix §A.7, we expect that polymer adsorption, migration, and wall slip occur over length scales $\sim$ 0.1 to 10 μm, over one to three orders of magnitude smaller than the smallest channel dimension $L_\mathrm{c} = 400$ μm. Also as described further in the appendix §A.7, we expect that shear banding and polymer entanglement effects do not occur for the dilute concentrations explore here. How-

ever, such effects could play a role in the flow of more concentrated polymer solutions in media with smaller pores.

The shear stress varies approximately linearly with shear rate, with a shear thinning exponent ≈ 0.92, indicating that shear thinning effects are small due to the high viscosity of the background solvent. Indeed, the pure solvent viscosity is approximately $\beta = 0.6$ times the measured solution viscosity. However, for accuracy, we use the rate-dependent shear viscosity $\eta(\dot{\gamma}) \equiv \sigma(\dot{\gamma})/\dot{\gamma}$ in all calculations. The shear rate varies widely within the complex geometry used in our experiments; therefore, to determine a shear rate that characterizes each experiment, we evaluate the wall shear rate in the pore throat at each value of Q tested, since it is the maximal shear rate in our system. We do this using a numerical solution for a power-law shear-thinning fluid. [129,130] We use this choice of the maximal shear rate to estimate characteristic values of the fluid Reynolds number*, Weissenberg number†, Elasticity number‡, and the M parameter. In particular, this choice of wall shear rate enables us to provide upper bounds for the fluid Reynolds numbers $\ll 1$, ensuring that inertia is negligible throughout the flow, as well as the M parameter, whose maximal value is believed to generate unstable flow. [131]

An elastic instability arises when elastic stresses—characterized by a large value of Wi—persist over curved streamlines. This persistence of elastic stresses occurs if the flow time

*Reynolds number at the pore-throat $\mathrm{Re} \equiv \rho U_t L/\eta(\dot{\gamma})$, where ρ is the density of the solvent, $U_t \equiv Q/A_t$ is the average speed corresponding to flow through the pore throat cross-section $A_t = (W - D_p)H$, and the length scale L is chosen to be half the constriction width $\frac{1}{2}(W - D_p)$. This estimate represents an upper bound for the Reynolds number characterizing the flow; in our porous media experiments, Re ranges from $\approx 8 \times 10^{-5}$ to 7×10^{-3}, indicating that viscous stresses dominate over inertial stresses.

†Weissenberg number at the pore throat $\mathrm{Wi} \equiv N_1(\dot{\gamma}_w)/2\sigma(\dot{\gamma}_w)$, following convention, where $\dot{\gamma}_w$ is the maximal wall shear rate as described in 2.1. In our porous media experiments, Wi ranges from $\approx$ 2 to 9, indicating that elastic stresses dominate.

‡Elasticity number at the pore throat $\mathrm{El} \equiv \mathrm{Wi}/\mathrm{Re}$, which compares elastic stresses to inertial stresses, are $\gtrsim 900$. Our experiments thus probe the elasticity-dominated flow regime.

scale $U_t/\mathscr{R}$, where $\mathscr{R}$ is the streamline radius of curvature, exceeds the polymer relaxation time λ. Thus, elastic stresses build up in the flow, leading to the generation of unstable flow, when the parameter $\mathrm{M} \equiv \sqrt{2\mathrm{Wi} \cdot \lambda U_t/\mathscr{R}}$ exceeds a threshold value, as confirmed experimentally for diverse flow geometries.[76–79] Indeed, the M parameter is derived from a linear stability analysis of the Navier-Stokes equation for a viscoelastic fluid;[76,77] specifically, it represents the order of the largest destabilizing term in the Navier-Stokes equation, which leads to the generation of unsteady flow. Therefore, M parameterizes the onset of flow instability due to fluid elasticity, and we use this parameter to describe the different flow regimes tested in our experiments. We evaluate M using the wall shear rate in the pore throat at each value of Q tested, since this produces the maximal shear rate and therefore the highest local M, which is believed to generate unstable flow.[131] For this value of the shear rate, we then use our measurements of polymer solution rheology to calculate Wi as well as the rheological relaxation time $\lambda = \mathrm{Wi}/\dot{\gamma}$. We find $\lambda \approx 0.3$ to 6 s, in good agreement with previous measurements performed on similar solutions.[85] Additionally, we calculate the streamline radius of curvature using the empirical expression M[77] for the onset of unstable flow around a cylindrical post of diameter D_p centered within a channel of width W: $\mathscr{R} \approx \left(2/D_p + 32.5/W\right)^{-1}$, where D_p and W are as illustrated in figure 2.2. We note that in our experiments, the posts are wall-centered instead of channel-centered; determining whether and how this difference in geometry influences $\mathscr{R}$ will be a useful direction for future theoretical work. Using the calculated values of Wi, λ, and $\mathscr{R}$, we then calculate $\mathrm{M} \equiv \sqrt{2\mathrm{Wi} \cdot \lambda U_t/\mathscr{R}}$. The corresponding values of M range from $\approx$ 6 to 31 for our experiments.

2.2 Isolated pore throat

To test the limiting case of widely-spaced pores ($l_s \to \infty$), we first investigate flow through an isolated pore throat centered in a channel. At low imposed flow rates, and thus at low values of M, the flow is laminar: the fluid streamlines do not cross and do not change in time. We do not observe eddies—instead, the streamlines smoothly converge as they approach the throat and symmetrically diverge as they leave it. However, above a threshold value of $M \approx 19$, we observe the onset of a flow instability: a pair of unstable eddies forms against the channel walls upstream of the pore throat, as exemplified in figures 2.3a-c (at the pore throat) and d-f (upstream) for $M = 19.4$, 23.9, and 30.5.

Within each eddy, the fluid recirculates with a speed slower than the mean imposed flow speed in the channel. The fluid streamlines continually fluctuate on long timescales, and also continually cross, indicating that fluctuations in the flow occur on a time scale shorter than the streamline duration of $10\tau_{pv}$ (figures 2.3d-f). These fluctuations are reflected in the motions of the eddy boundaries and lengths, which also fluctuate as the flow progresses. Similarly, while the fluid in the region formed between the eddies does not recirculate, the fluid streamlines also continually fluctuate on long timescales and continually cross, reflecting the presence of rapid fluctuations in the flow throughout. By contrast, the flow is more steady downstream of the pore throat: we do not observe any eddies or marked temporal changes in the flow for all values of M tested. This result is consistent with previous observations of highly unstable eddies upstream of a cylinder in a channel, but suppressed fluctuations and no eddies downstream.[97] We therefore focus our subsequent analysis on

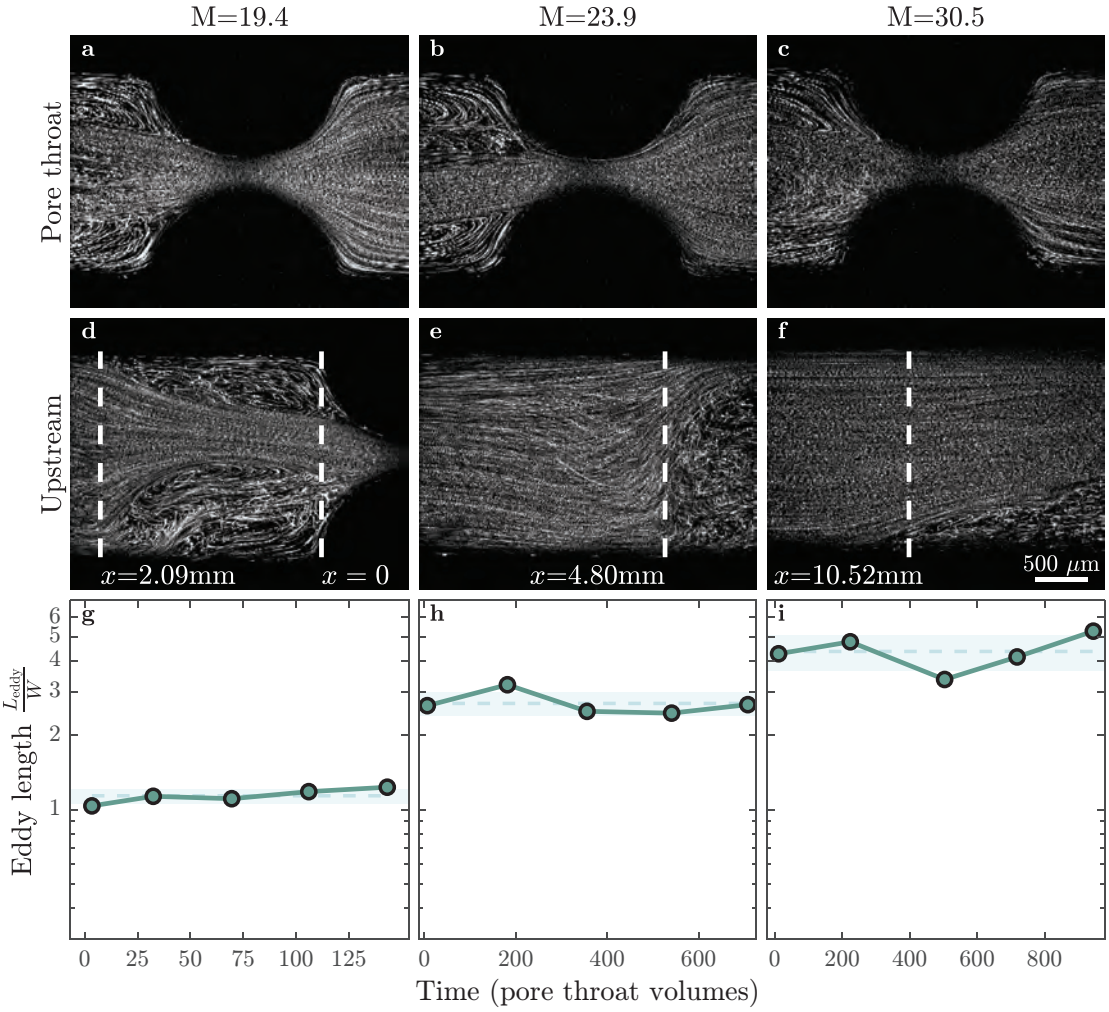

Figure 2.3: streamline images of polymer solution flow through a straight channel with a single pore throat. streamline images are averaged over $10\tau_{pv}$. Flow rates are expressed via the M parameter, which equals 19.4, 23.9, and 30.5 for panels **a**, **b**, and **c** respectively, corresponding to Weissenberg numbers $\mathrm{Wi} = 5.6, 6.9$, and 8.8. **a–c** show strong recirculating eddies upstream of the pore throat, but no downstream eddies at any flow rate. **d–f** show the leftmost edge of the eddies in front of the pore throat. Dashed lines indicate where the eddy-dominated region begins. x indicates the distance in millimeters from the base of the hemi-cylinder. **g–i** show the measured eddy length over time normalized by τ_{pv}. Shaded regions show standard deviation around the temporal mean (dashed lines).

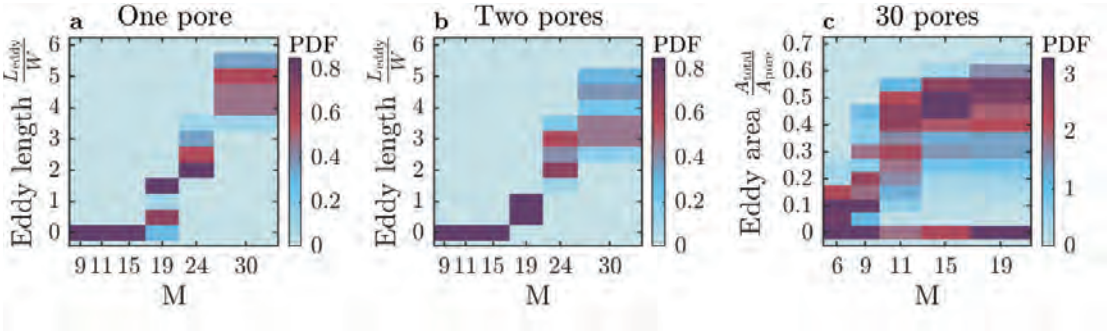

Figure 2.4: Probability density functions of measured eddy sizes for different values of M, averaged over at least $7\tau_{pv}$ and over two separate replicate experiments, displayed vertically as heatmaps. **a** PDFs of L_{eddy}/W for a channel with a single pore throat constriction. For each value of M there is a single characteristic eddy length that increases monotonically with M. **b** PDFs of L_{eddy}/W for a channel with two widely-spaced pores $l_s = 16W$ apart. Again, for each value of M there is a single characteristic eddy length that increases monotonically with M. **c** PDFs of A_{total}/A_{pore} for a porous medium with 30 closely-spaced pores $l_s = W$ apart. Here, the PDFs for $M > 9$ are bimodal, showing multiple characteristic eddy areas (one peak at $\frac{A_{eddy}}{A_{pore}} \approx 60\%$ and one peak at $\frac{A_{eddy}}{A_{pore}} \approx 0$). The two branches in the PDFs indicate a bistability in unstable flow states.

the upstream region.

To further characterize this behavior, we track the eddy length L_{eddy} over time for each value of M tested. We measure L_{eddy} from the base of the hemi-cylinders ($x = 0$ in figure 2.3d) to the farthest upstream location having a streamline oriented perpendicular to the imposed flow direction (dashed lines in figures 2.3d-f). Consistent with the visual observations, L_{eddy} fluctuates over time in each experiment, as indicated by the shaded regions in figures 2.3g-i; however, it fluctuates around a single mean value that increases with M. We quantify these fluctuations using the coefficient of variation c_v, defined as the ratio between the standard deviation and the mean of the measurements of L_{eddy} over time. Taking data from two replicate experiments at these imposed flow rates, we find $c_v \approx 0.3$, 0.3, and 0.4 for $M = 19.4$, 23.9, and 30.5 respectively.

We summarize all of our measurements by plotting the probability density (PDF) of time-averaged measured eddy lengths for each value of M tested. Below the threshold value

of M $\approx$ 19, we do not observe eddies and hence $L_{\text{eddy}} = 0$. By contrast, above this threshold, $L_{\text{eddy}} > 0$ fluctuates about a well-defined mean value, which increases with M, as shown in figure 2.4a. This increase in L_{eddy} is similar to previous measurements for isolated constrictions; these studies demonstrate that eddies form when polymers are elongated, and the size of eddies grows as polymers are increasingly elongated.[50–54] Our results thus suggest that flow fluctuations arising from unstable flow elongate the individual polymer chains,[132–136] which then generate unstable upstream eddies to minimize extensional stresses.[50–54]

2.3 Two widely-spaced pore throats

We next investigate two pore throats spaced a distance $l_s = 16W$ apart along the flow direction. As we find with an isolated throat, the flow is laminar at low values of M, while above a similar threshold value of M $\approx$ 19, we observe the onset of the flow instability. A pair of unstable eddies again forms against the channel walls upstream of each pore throat, as exemplified in figures 2.5a-c (first throat) and d-f (second throat). Moreover, as with the isolated pore throat, the flow is more steady immediately downstream of each throat, with no observable eddies or temporal changes in the flow for any values of M tested.

We again quantify this behavior by measuring L_{eddy} over time for each value of M tested. For each pore throat, L_{eddy} again fluctuates around a single mean value that increases with M (figures 2.5g-i)—similar to the case of an isolated throat. The PDFs of the combined time-averaged measurements of L_{eddy} also reflect its increase with M, as shown in figure 2.4b. Intriguingly, however, we observe two key differences from the isolated throat. First, while the mean values of L_{eddy} are similar for the two pore throats, eddies upstream of the

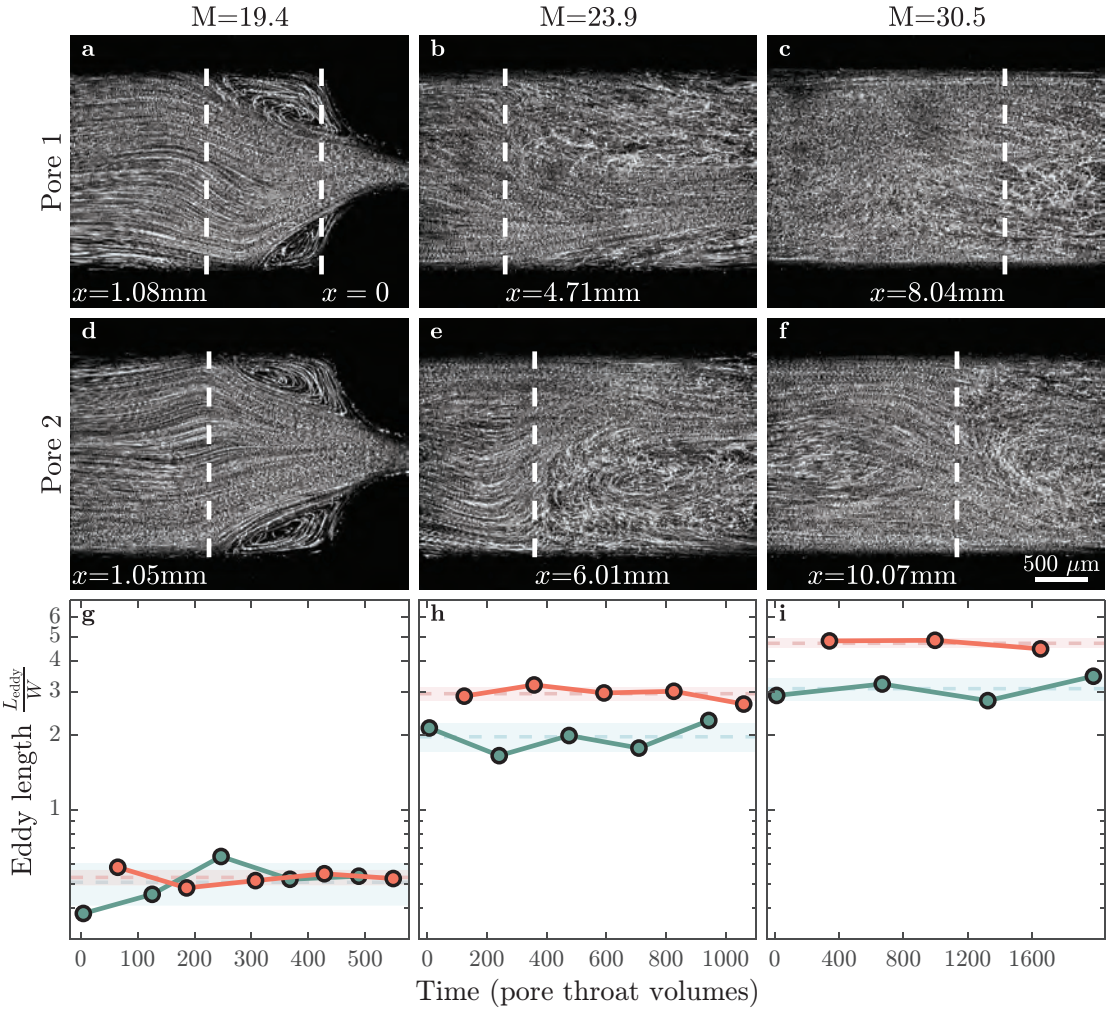

Figure 2.5: Streamline images of polymer solution flow through a straight channel with two pore throats separated by $l_s = 16W$. Streamline images are averaged over $10\tau_{pv}$. Flow rates are expressed via the M parameter, which equals 19.4, 23.9, and 30.5 for **a**, **b**, and **c** respectively, corresponding to $\mathrm{Wi} = 5.6, 6.9$, and 8.8. **a–c** show the leftmost edge of the eddies in front of the first pore throat. **d–f** show the leftmost edge of the eddies in front of the second pore throat. No eddies are observed downstream of either throat. **g–i** show the measured eddy lengths over time normalized by τ_{pv} for pore 1 (green) and pore 2 (red). Shaded regions show standard deviation around the temporal mean (dashed lines).

second throat (red points, figures 2.5g-i) are slightly larger than eddies upstream of the first throat (green points) for large values of M. Second, the eddies upstream of the second throat are less unstable—the temporal fluctuations in L_{eddy} are notably suppressed for the second pore throat for all M above the threshold for unstable flow (compare red to green shaded regions in figures 2.5g-i). Comparing the coefficients of variation confirms this finding: for the first pair of eddies, $c_v = 0.2 \pm 0.1$ while for the second pair, $c_v = 0.10 \pm 0.02$, which is significantly smaller ($p = 0.02$, one-tailed t-test). Thus, when the spacing between pore throats is reduced, the spatio-temporal characteristics of the flow are altered—presumably because polymer elongation can persist across multiple pores.

2.4 Thirty closely-spaced pore throats

To further test the hypothesis that polymer memory impacts flow behavior, we next investigate flow through a medium with an even smaller spacing between pore throats. Specifically, the flow channel contains thirty pore throats spaced a distance $l_s = W$ apart along the flow direction. In this case, we find that the flow behavior is strikingly different from the larger l_s cases described in Sections 2.2 and 2.3.

One key difference is that the threshold for the onset of the flow instability is dramatically lowered. At low imposed flow rates, and thus at low values of M, the flow is laminar: the fluid streamlines do not cross and do not vary over time. In this regime, a pair of small, symmetric, laminar, recirculating eddies forms in the corners of each pore body due to the small spacing between successive pore expansions and constrictions. Above a threshold value of $\text{M} \approx 9$—considerably smaller than the threshold $\text{M} \approx 19$ for the single- and double-throat cases—we observe the onset of unstable flow: the fluid streamlines continu-

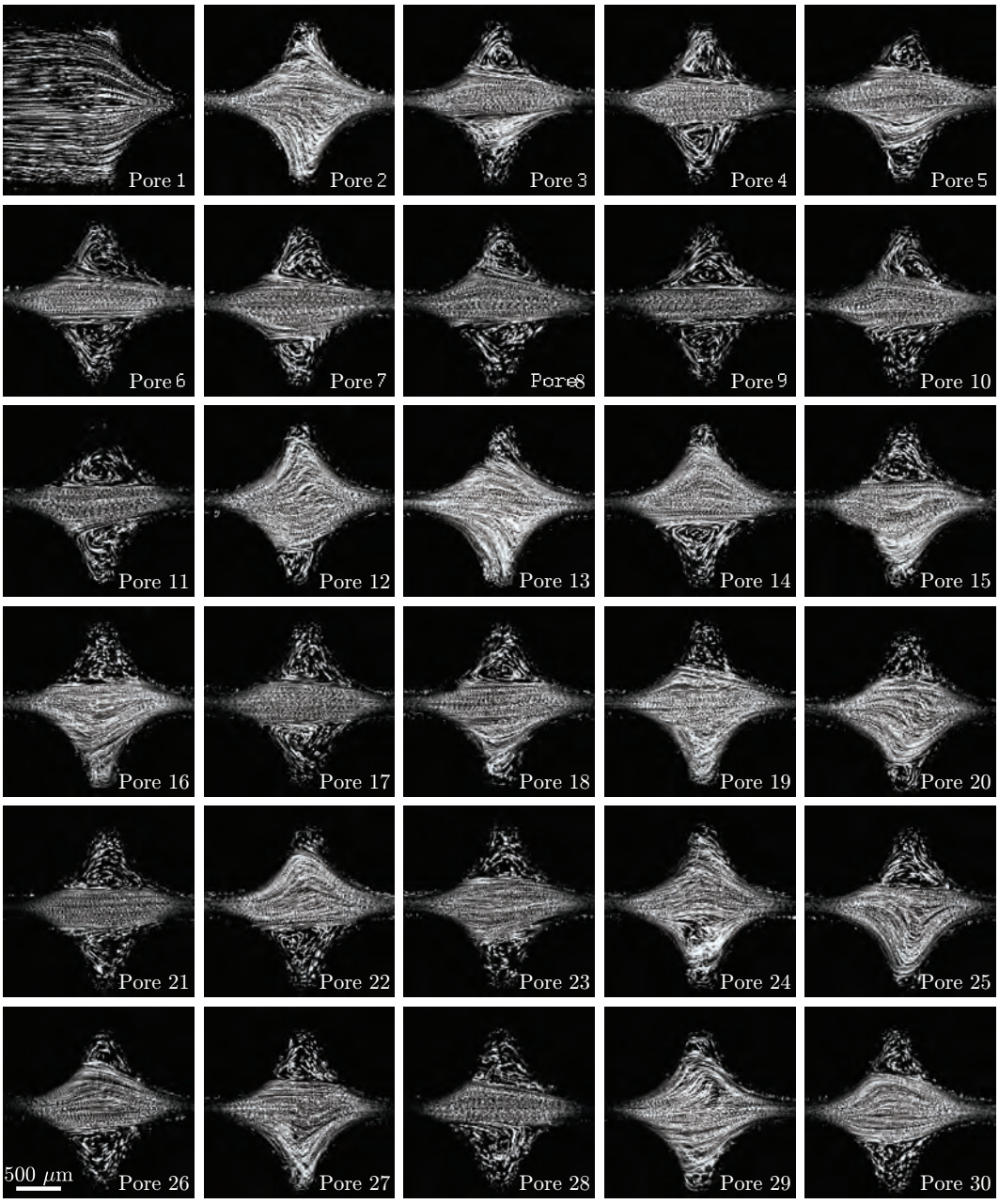

Figure 2.6: Streamline images of polymer solution flow through a porous medium with 30 pore throats separated by $l_s = W = 2$ mm at $\mathrm{M} = 11.4$. Images span 2.11 mm across. Streamline images are averaged over $10\tau_{pv}$. Pore 6 exemplifies the eddy-dominated state, with eddies that continually fluctuate both internally and at their boundaries, while pore 2 exemplifies the eddy-free state, with strongly-fluctuating streamlines that fill the entire pore body.

ally cross and vary over time. Thus, decreasing the spacing between pore throats decreases the threshold value of M required for unstable flow, suggesting that polymer memory strongly impacts the flow behavior.

Even more strikingly, we observe two distinct flow states that can arise in each pore body throughout the medium: an 'eddy-dominated' state in which a pair of large unstable eddies forms in the corners of the pore body, and an 'eddy-free' state in which strongly-fluctuating fluid streamlines fill the entire pore body and eddies do not form. This surprising bistability is illustrated in figure 2.6, which shows the streamline images taken sequentially from each pore in the medium at $\mathrm{M} = 11.4$. Pore 6 exemplifies the eddy-dominated state, with eddies that continually fluctuate both internally and at their boundaries, while pore 2 exemplifies the eddy-free state, with strongly-fluctuating streamlines that fill the entire pore body. Though these snapshots are taken at an optical slice in the center of the channel height, imaging at other heights shows similar flow streamlines, indicating that the spatial structure of the flow does not vary appreciably across the channel height. This observation is in stark contrast to the typical assumption that flow behavior in a porous medium is determined just by injection conditions and the geometry of the individual pores.[137] Instead, we find that different pores can exhibit distinct flow characteristics, even when the individual pore geometries and imposed flow rates are all identical.

To quantify this behavior, we measure the two-dimensional (2D) area of the individual eddies A_{eddy} over time for each value of M tested. In laminar flow, the eddies occupy only $\approx 5\%$ of the total area of a pore, which we define as $A_{\mathrm{pore}} \equiv Wl_{\mathrm{s}} - \pi D_{\mathrm{p}}^2/4$. By contrast, unstable eddies in the eddy-dominated state have values of A_{eddy} that fluctuate strongly in time, and whose mean value can be up to $\approx 30\%$ of A_{pore}, while in the eddy-free state

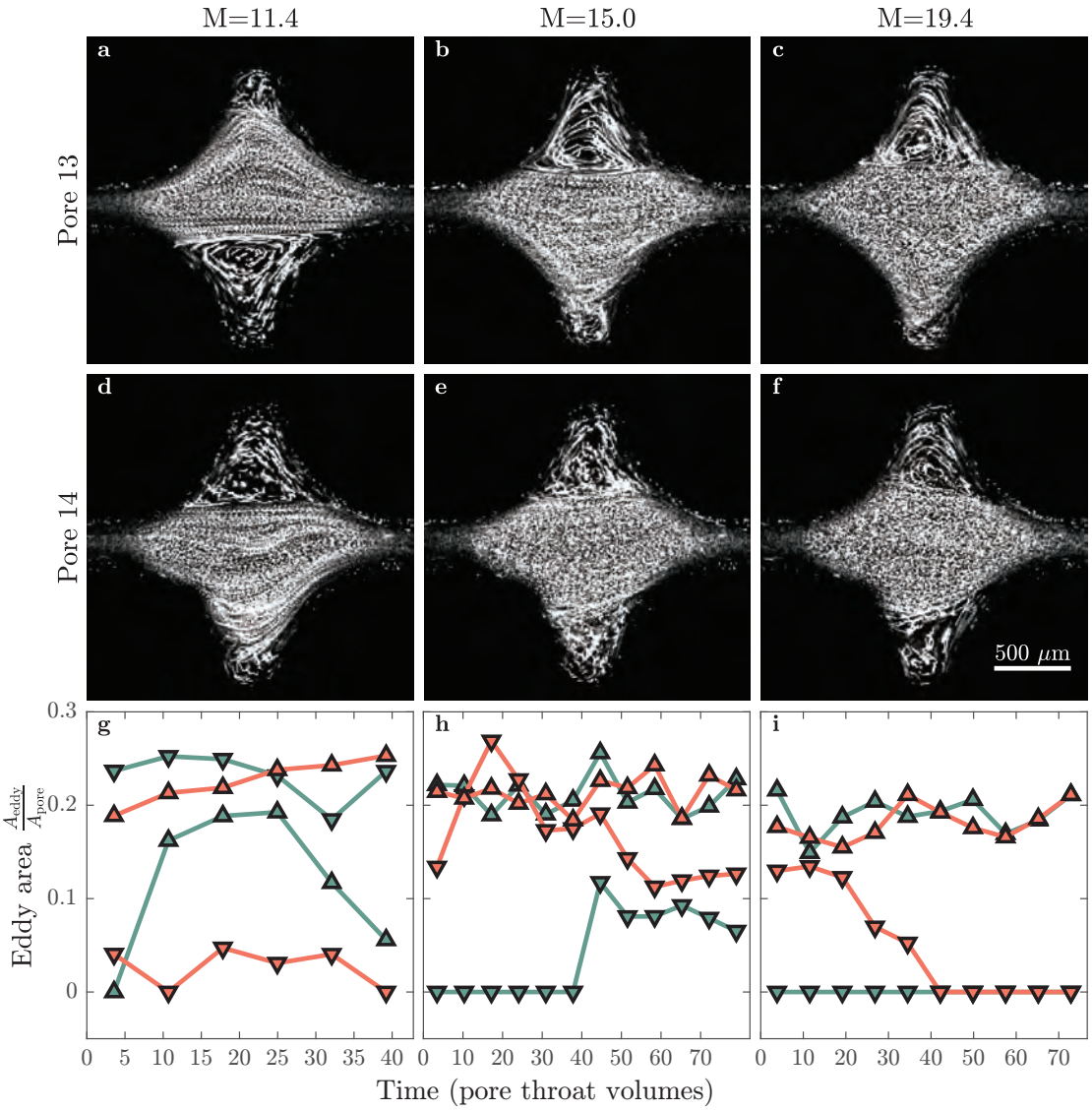

Figure 2.7: Streamline images of polymer solution flow through pores 13 **a–c** and 14 **d–f** at different flow rates corresponding to $\mathrm{M} = 11.4, 15$, and 19.4 (left to right). Streamline images are averaged over $10\tau_{\text{pv}}$. **g–i** show the measured eddy areas $A_{\text{eddy}}/A_{\text{pore}}$ over time normalized by τ_{pv} for pore 13 (green) and pore 14 (red). Upward triangles are for the top region of the pore body, downward triangles are for the bottom region of the pore body.

$A_{\text{eddy}} \approx 0$. Intriguingly, while the two flow states are each unstable, the flow behavior in each pore body appears to be bistable, as illustrated in figure 2.7: a pore will persist in a given unstable flow state for a long duration of time before switching, seemingly randomly, to the other flow state. For example, at $\text{M} = 11.4$, the upper eddy in pore 13 and the lower eddy in pore 14 (figure 2.7g, upward-pointing red triangles and downward-pointing green triangles respectively) persist in the eddy-dominated state over the entire imaging duration, while the lower eddy in pore 13 persists in the eddy-free state (downward red triangles). However, the upper eddy in pore 14 initially switches from the eddy-free to the eddy-dominated state, in which it persists for $15\tau_{\text{pv}}$ before switching back to the eddy-free state (upward green triangles). We observe this flow bistability in all pores of the medium, and at all values of M tested; two more examples for $\text{M} = 15$ and 19.4 are shown in figures 2.7h-i respectively.

To further characterize the flow bistability shown in figures 2.7g-i, we plot the PDFs of the time-averaged measurements of A_{total}, which describes the total A_{eddy} measured in each pore combined for all thirty pores in the medium. Below $\text{M} \approx 9$, $A_{\text{total}} \approx 10\%$ of A_{pore}, and eddies do not change in time; by contrast, above the onset of the flow instability at $\text{M} \approx 9$, the PDFs become bimodal, reflecting the bistability in flow behavior (figure 2.4c). The eddy-dominated state is represented by the upper branch of the PDFs, in which A_{total} increases with M, eventually plateauing at $\approx 60\%$ of A_{pore} at the highest values of M tested. The eddy-free state is represented by the lower branch of the PDFs, in which $A_{\text{total}} \approx 0$ over all M. This bistability does not arise in porous media with wider pore spacings: the lower branch of the PDFs does not appear in figures 2.4a-b. Thus, when the spacing between pore throats is reduced from $l_s = 16W$ to $l_s = W$—and thus, elongation of indi-

vidual polymers is more likely to persist across multiple pores—the flow abruptly becomes bistable, exhibiting two coexisting unstable flow states. Indeed, previous work has theorized that unstable flow may bifurcate into two coexisting flow states;[106,138,139] to our knowledge, our work is the first experimental confirmation of this prediction.

2.5 Bistability and polymer conformations in flow

How does this unusual flow bistability arise? Previous measurements of polymer conformations indicate that differing fractions of coiled and elongated chains coexist in extensional and unstable flows depending on the imposed flow conditions.[47,71,73] Furthermore, simulations indicate that polymers having different elongation can have dramatically differing pore-scale flow behaviors.[140,141] Thus, we hypothesize that flow bistability arises from the interplay between flow-induced polymer elongation, which promotes eddy formation, and relaxation of polymers as they are advected between pores, which enables the eddy-free state to form.

We first consider a pore in the eddy-dominated state. Polymers entering the pore are likely in an elongated conformation due to the combined influence of unstable flow fluctuations and extension by flow converging into the upstream pore throat. Indeed, previous work has demonstrated that eddies form upstream of a constriction when polymers are elongated.[50–54] Eddy formation minimizes extensional stresses in the center of the pore: the net flow through the pore body occurs in a nearly-straight channel spanning one pore throat to the next, as can be seen in the example of pore 6 in figure 2.6. For simplicity, we consider the limit of large M, in which eddies completely fill the corners of the pore body. With the exception of unstable fluctuations, the flow velocities in this channel are then

aligned along the flow direction with speed $\sim U_t \equiv Q/A_t \sim 1$ mm/s, and therefore the extensional component of the flow in the channel is minimal. The elongated polymers thus continue to relax as they are advected through this channel, reaching their equilibrium coiled conformation after a duration $\sim \lambda_{rel}$, the chain relaxation time. We compare this time scale to the residence time required for the polymers to transit across the pore body from the upstream throat to the downstream throat, $\sim l_s/U_t$, yielding an advective Deborah number $De_{adv} \equiv \lambda_{rel} U_t/l_s$. When l_s is small and $De_{adv} \gtrsim 1$, chains are still elongated as they enter the next pore body, thereby promoting eddy formation in the current pore and the downstream pore as well. For our experiments in the unstable regime with $l_s = W$, De_{adv} ranges from ~ 0.5 to 3 using $\lambda_{rel} \sim \lambda \approx 1$ s; this estimate likely under-estimates De_{adv}, since λ_{rel} is known to increase considerably in extensional flow.[142] Thus, we expect the eddy-dominated state to persist in the pore body over time before random flow fluctuations cause it to switch to the eddy-free state, consistent with our measurements shown in figures 2.7g-i. We also expect the eddy-dominated state to be correlated between neighboring pores.

We next consider the formation of the eddy-free state. As polymers pass through eddy-dominated pores, they gradually relax to the coiled conformation. When a sufficient fraction of coiled polymers are at the entrance to a pore, there will be no driving force for eddy formation. The pore will thus be in the eddy-free state. The fluid streamlines then diverge from the upstream pore throat, creating a compressional flow that further promotes the coiled conformation. As the polymers continue to traverse the pore body, they remain coiled until they encounter the converging flow into the downstream pore throat. This extensional flow partially elongates the chains, which requires a time scale $\sim \lambda_{ret}$.

We again compare this time scale to the residence time required for the polymers to transit from the beginning of the converging region to the downstream throat, in this case $\sim H\left(WD_\mathrm{p}/2 - \pi D_\mathrm{p}^2/8\right)/Q$. This comparison yields another advective Deborah number $\mathrm{De}'_\mathrm{adv} \equiv \lambda_\mathrm{ret} Q/\left[H(WD_\mathrm{p}/2 - \pi D_\mathrm{p}^2/8)\right]$. When $\mathrm{De}'_\mathrm{adv} \gtrsim 1$, chains are not elongated as they enter the next pore body, thereby promoting the eddy-free state in the current pore and the downstream pore as well. For our experiments in the unstable regime, $\mathrm{De}'_\mathrm{adv}$ ranges from ≈ 0.7 to 5 using $\lambda_\mathrm{ret} \sim \lambda \approx 1$ s, although these values again likely under-estimate $\mathrm{De}'_\mathrm{adv}$. Thus, similar to the eddy-dominated state, we expect the eddy-free state to persist in the pore body over time before random flow fluctuations cause it to switch to the eddy-dominated state, consistent with our measurements shown in figures 2.7g-i. Moreover, we again expect the eddy-free state to be correlated between neighboring pores.

2.6 Temporal and Spatial Characteristics of the Flow

The hypothesis presented in §2.5 makes two testable predictions: first, that the two different unstable flow states each persist over long times before randomly switching, and second, that the flow states between neighboring pores n and $n+1$ are correlated. We test these predictions by investigating the temporal and spatial characteristics of the pore-scale flow. Specifically, we simultaneously image two neighboring pores within the medium, pores $n = 21$ and $n + 1 = 22$, at $\mathrm{M} = 15$ and monitor the flow states for $2500\tau_\mathrm{pv}$. Figure 2.8a shows a snapshot of the flow streamlines imaged simultaneously and averaged over $10\tau_\mathrm{pv}$ at an instance when both pores are in the eddy-dominated state.

The data in figures 2.7g–i support the first prediction that the two distinct flow states persist over long times. To further test this prediction, we measure the distribution of dura-

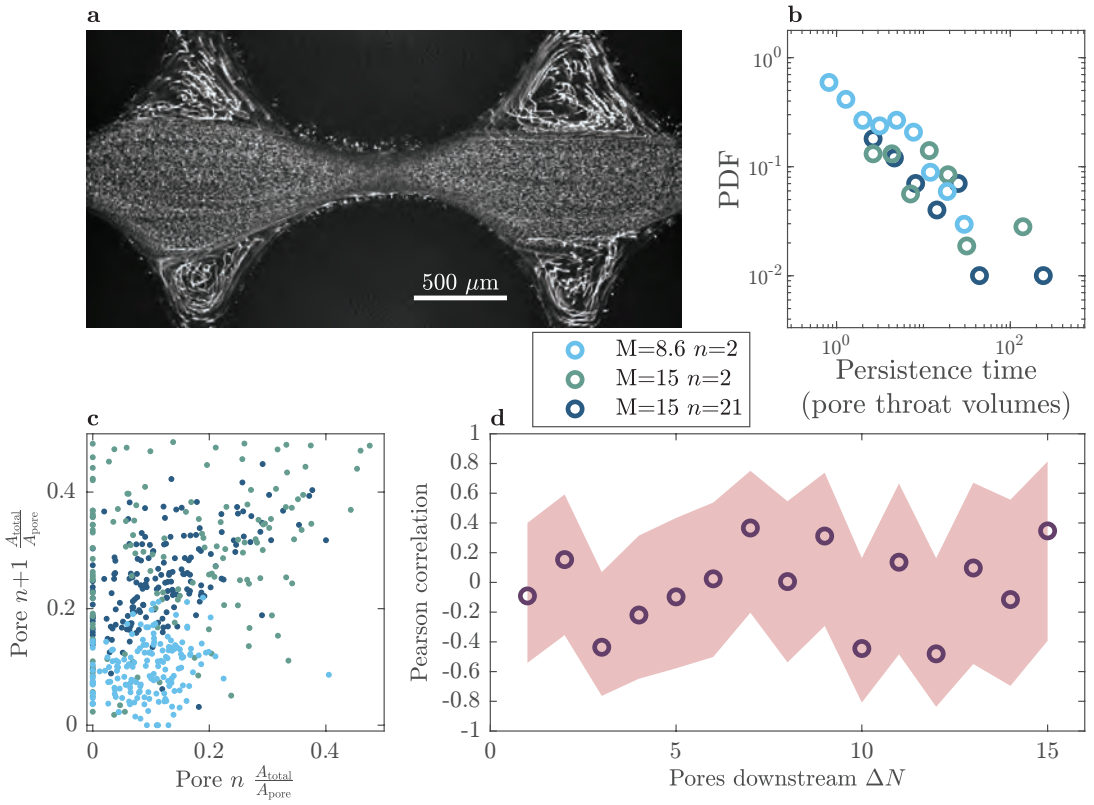

Figure 2.8: **a** Simultaneous streamline imaging of pores 21 and 22 averaged over $10\tau_{\text{pv}}$ for M $= 15.0$. Both pores are in the eddy-dominated state. **b** Probability density function of times between discrete switching events, representing the duration over which a given flow state persists in pores n or $n+1$, for pores imaged over at least $400\tau_{\text{pv}}$. For panels b and c, light blue shows M $= 8.6$ for $n = 2$, teal blue shows M $= 15$ for $n = 2$, and navy blue shows M $= 15$ for $n = 21$. The data are broadly distributed with long tails. **c** Instantaneous eddy areas of pores n and pore $n+1$ are positively correlated, indicating that flow states are correlated between neighboring pores. **d** Pearson correlation coefficients between pores separated by a length $l_s\Delta N$ and imaged sequentially a time $80\tau_{\text{pv}}\Delta N$ apart for M $= 15.0$. The flow state of each pore is averaged over $80\tau_{\text{pv}}$. Thus, this analysis only quantifies any possible long-time correlations that persist over time scales larger than $80\tau_{\text{pv}}\Delta N$. Light red shaded region indicates 99% confidence interval for estimated correlation coefficient given the sampling size.

tions over which each flow state persists in a given pore before switching to the other state; we define a switching event as the instant when the total eddy area A_{total} in a given pore crosses a threshold value of $0.05\,A_{\text{pore}}$. This threshold is motivated by the clear separation between the eddy-dominated and eddy-free states indicated by the probability density function in figure 2.4c. In agreement with our expectation, we find a broad distribution of long flow persistence times with no characteristic persistence time, as shown by the navy blue points in figure 2.8b—confirming our first prediction. Indeed, theoretical predictions for two-state systems that have self-stabilizing states—similar to the eddy-dominated and eddy-free states described here—also predict broad distributions of state persistence times.[143]

The image in figure 2.8a supports the second prediction that the flow states in neighboring pores are correlated. To further test this prediction, we measure the instantaneous total eddy areas $A_{\text{total},n}$ and $A_{\text{total},n+1}$ in pores $n = 21$ and $n + 1 = 22$ by imaging both pores simultaneously over several thousand τ_{pv}. To visualize the streamlines of the individual tracer particles, we average successive frames for $10\tau_{\text{pv}}$; this procedure enables us to determine the presence or absence of recirculating eddies in the pore bodies and provides a way to directly measure the eddy areas by tracking the eddy boundaries, as exemplified in figure 2.8a. We thereby compute the total eddy area A_{total} in each pore body of area A_{pore}. Over the course of this experiment, the pore bodies exhibit the full range of flow behaviors: we measure the full range of possible total eddy sizes for each pore body, ranging from $A_{\text{total}} = 0$ to the maximal value $A_{\text{total}} \approx 0.5A_{\text{pore}}$. Then, to quantify the correlation in flow state between pores n and $n + 1$, we plot the total eddy areas simultaneously measured for both pores at different times, $A_{\text{total},n}$ and $A_{\text{total},n+1}$ respectively. These measurements show a positive correlation between the instantaneous flow states of neighboring

pores $n = 21$ and $n + 1 = 22$ over the imaging duration, as shown by the navy blue points in figure 2.8c. We quantify this correlation using the Pearson correlation coefficient $\rho_{n,n+1} \equiv \text{cov}\left(A_{\text{total},n}, A_{\text{total},n+1)}\right) / \left[\sigma(A_{\text{total},n})\sigma(A_{\text{total},n+1})\right]$, where cov is the covariance and σ is the standard deviation of the instantaneous measurements of $A_{\text{total},n}$ and $A_{\text{total},n+1}$ over the different times. We find $\rho_{21,22} = 0.55 > 0$, confirming a positive correlation between the eddy sizes in the neighboring pores 21 and 22 that is statistically significant ($p < 0.001$, two-tailed t-test). Thus, the unstable flow states in neighboring pores are correlated with each other, confirming our second prediction.

To further test how this behavior varies spatially and with M, we repeat these measurements near the inlet at pores $n = 2$ and $n + 1 = 3$ at two different flow rates corresponding to $\text{M} = 15$ and $\text{M} = 8.6$. We expect that decreasing the flow rate will decrease the advective Deborah numbers De_{adv} and De'_{adv}; thus we expect that at lower flow rates, unstable flow states will still be broadly distributed, but will persist over shorter time scales. Our data confirm this expectation: we find that at the lower flow rate, flow states persist for slightly shorter times, as indicated by the light blue points ($\text{M} = 8.6$, $n = 2$) compared to the teal blue points ($\text{M} = 15$, $n = 2$) shown in figure 2.8b. The unstable flow states in neighboring pores remain positively correlated with each other in both cases, as shown by the light blue and teal blue points in figure 2.8c; the corresponding Pearson correlation coefficients are $\rho_{2,3} = 0.25 > 0$ and $\rho_{2,3} = 0.21 > 0$ respectively, confirming a positive correlation that is statistically significant ($p < 0.001$, two-tailed t-test). This positive correlation likely reflects the fact that, even at the lower flow rate with $\text{M} = 8.6$, both $\text{De}_{\text{adv}} \approx 0.5$ and $\text{De}'_{\text{adv}} \approx 0.7$ are close to one, and thus, flow states are still likely to be correlated between neighbors. Intriguingly, while the correlation coefficient does not depend strongly on M for this range

of flow rates, it does increase with position along the flow direction: for the same M $= 15$, $\rho_{2,3} = 0.21$ while $\rho_{21,22} = 0.55$, suggesting that flow states in neighboring pores become increasingly correlated downstream. Further exploring this spatial dependence of correlations in unstable flow state will be a useful direction for future work.

While neighboring pores exhibit correlated flow states on short time scales, imaging of flow through the entire medium (figure 2.6) suggests that these correlations are not sufficient to produce long-range correlations in the flow over long times. Indeed, as quantified by the measurements in figure 2.8b, we do not expect correlations to persist, even for neighboring pores, when flow state is averaged over sufficiently long time scales. To test this expectation, we sequentially image pores $n = 2$ through $n = 30$ for $80\tau_{\mathrm{pv}}$ each. We use these data to compute the time-averaged eddy area in each pore, $\bar{A}_{\mathrm{total},2}$ through $\bar{A}_{\mathrm{total},30}$, where each value of $\bar{A}_{\mathrm{total}}$ is averaged over $80\tau_{\mathrm{pv}}$. We then quantify any possible correlations between these 29 measurements of the time-averaged eddy areas using the correlation coefficient $\rho_{n,n+\Delta N} \equiv \mathrm{cov}\left(\bar{A}_{\mathrm{total},n}, \bar{A}_{\mathrm{total},n+\Delta N}\right) / \left[\sigma(\bar{A}_{\mathrm{total},n})\sigma(\bar{A}_{\mathrm{total},n+\Delta N})\right]$, which in this case quantifies correlations between the measured $\bar{A}_{\mathrm{total}}$ for all pores n and $n + \Delta N$ that are thus separated by a length $l_s\Delta N$; here, cov is the covariance and σ is the standard deviation of the time-averaged measurements of $\bar{A}_{\mathrm{total},n}$ and $\bar{A}_{\mathrm{total},n+\Delta N}$, for a given value of ΔN ranging from 1 to 15, over the different values of n. In this analysis, instead of tracking the instantaneous correlation for many different time points as before, we track a time-averaged correlation for many different pairs of pores. Thus, this correlation analysis does not capture any possible flow correlations ΔN pores apart that arise on time scales shorter than $80\tau_{\mathrm{pv}}\Delta N$: it only quantifies any possible long-time correlations that persist over time scales larger than $80\tau_{\mathrm{pv}}\Delta N$. Consistent with our expectation, we do not find long-time correlations in flow

state, even between nearest neighbors: the correlation coefficient does not statistically deviate from zero for any values of ΔN throughout the medium, as shown in figure 2.8d. Thus, while unstable flow states are correlated over short times across neighboring pores, these correlations do not persist over long time scales—presumably due to the influence of random fluctuations in the flow, which likely promote switching between flow states. Our data do not preclude the possibility that longer-range correlations may arise at shorter time scales, or that correlations in flow state can evolve spatially throughout the medium; indeed, previous work has indicated that velocity correlations can coherently propagate through other experimental geometries.[97] Investigating whether the flow correlations described in figure 2.8a-c can persist over broader spatial and temporal ranges will be a useful direction for future work.

2.7 Conclusions

Our work describes the first experimental observations of bistability in the flow of an elastic polymer solution through porous media, confirming previous theoretical predictions.[106,138,139] We find that when the spacing between pores is sufficiently small, and when the imposed flow rate is sufficiently large, the flow stochastically switches between two distinct unstable flow states. In the eddy-dominated state, a pair of large unstable eddies forms in the corners of a pore body, while in the eddy-free state, strongly-fluctuating fluid streamlines fill the entire pore body and eddies do not form. Our results thus indicate that in a porous medium the pore-scale flow behavior may not be determined just by injection conditions—as quan-

tified by the Weissenberg number Wi or the M parameter[76,77]—and the geometry of the individual pores, as is often assumed.

Our model 1D geometry does not incorporate pore size disorder, tortuosity, and connectivity for simplicity; it instead provides a way to isolate and systematically probe the role of pore spacing on flow behavior. Incorporating these additional complexities in the medium geometry, and extending our findings to 2D and 3D media in which transverse interactions between pores may also play a role,[15,44,103,104,108,109,111–115,117–119,144] will be an important direction for future studies. Moreover, because pressure drop measurements are often used to characterize flow through porous media,[24–28,34,42,123] exploring the connection between unstable flow states and the macroscopic pressure drop across the medium will also be an important extension of our work.

We hypothesize that the flow bistability arises from the interplay between flow-induced polymer elongation, which promotes eddy formation, and relaxation of polymers as they are advected between pores, which enables the eddy-free state to form. Consistent with this idea, we find that the eddy sizes increase with the imposed flow rate. Additionally, we find that a flow state in a given pore persists over long time scales before switching to the other flow state, presumably due to random flow fluctuations. Flow state is also strongly correlated between neighboring pores at short time scales; however, these correlations are not sufficient to produce correlations in the flow through the entire medium over long times. Elucidating the factors that determine the length and time scales over which flow correlations persist will be an interesting direction for future work.

While our experiments probe the case of dilute polymer solutions—in which polymer overlap likely does not influence flow behavior—flow behavior is known to change con-

siderably at higher concentrations due to the increased propensity of polymer chains to overlap.[109,111] We therefore expect that in more concentrated solutions, overlap of polymer chains will increase the relaxation and retardation times λ_{rel} and λ_{ret}, leading to larger values of the advective Deborah numbers De_{adv} and De'_{adv}. Thus, we expect that more concentrated polymer solutions will have correlated flow states that span more pores and that persist over longer time scales.

The different spatial and temporal characteristics of the two flow states described here could impact fluid mixing and the displacement of trapped immiscible fluids from the pore space in a variety of ways.[145,146] Thus, a deeper understanding of these flow behaviors could provide guidance to applications that require specific mixing or fluid displacement behaviors. Examples include oil recovery and groundwater remediation, in which the viscous forces exerted by the polymer solution could displace a trapped fluid from the pores, or unstable mixing due to the fluid instability could improve the transport of oxidants and surfactants to the fluid interface. Such flow behaviors could also be harnessed in other emerging applications such as controlling mixing and flow in lab-on-a-chip devices, filtration, and extrusion of polymeric resins during 3D-printing.

...an exquisite thing, a small thing that could upset balances and knock down a line of small dominoes and then big dominoes and then gigantic dominoes...

Ray Bradbury, A sound of Thunder

3

Chaos and resistance

We have seen how polymer memory can give rise to unstable flows and interesting spatial and temporal correlations in *ordered 2D* porous geometries. However, diverse applications—ranging from groundwater remediation [32] and oil recovery [21,123] to filtration [147] and chromatography [148]—rely on the viscous-dominated flow of polymer solutions through *disordered 3D* porous media. In these real porous media, the resistance to flow, quantified by an

apparent viscosity η_{app}, abruptly *increases* for many high molecular weight, flexible polymer solutions—even though the shear viscosity η of the bulk solution *decreases* with increasing shear rate.[44,123,149–151] The reason for this anomalous increase has remained a puzzle ever since it was first reported over half a century ago in the 1960s.[12]

This anomalous increase in flow resistance is often thought to reflect the accumulated extension of individual polymer molecules as they are transported through constrictions of the pore space,[34–38] though direct validation of this idea remains lacking. Some recent simulations[119] and experiments in ordered two-dimensional (2D) geometries[44,111,152–154] have instead suggested that this anomalous increase in flow resistance is linked to the onset of an elastic instability, arising from the buildup of polymer-induced elastic stresses during transport. Such instabilities are well-studied in a range of simplified geometries,[1,2,14,54,76,78,90,105,155–158] and can generate chaotic flow fields reminiscent of those observed in inertial turbulence[14,80,154]—often termed "elastic turbulence". However, whether this phenomenon arises in disordered 3D porous media, and if so, how exactly it influences macroscopic transport, is still debated; typical 3D media are opaque, precluding direct characterization of the flow in situ. Indeed, while magnetic resonance measurements of the diffusivity of a secondary fluid phase have hinted that elastic turbulence can arise in disordered 3D porous rocks,[43] direct verification remains lacking. Furthermore, recent experiments in model 2D media indicate that geometric disorder, inherent in most naturally-occurring media, can instead suppress

This chapter has been adapted from published work by Christopher A. Browne and Sujit S. Datta. Elastic turbulence generates anomalous flow resistance in porous media. *Science Advances*, 7:eabj2619, 2021.[3]
Author Contributions: C.A.B. performed all experiments; C.A.B. and S.S.D. designed the experiments, analyzed the data, developed and implemented the theoretical model, discussed the results, and wrote the manuscript. S.S.D. designed and supervised the overall project.

the onset of elastic turbulence,[15] casting doubt on this mechanism entirely—although other experiments have shown that this suppression is sensitive to the specific choice of 2D geometry,[120] and thus, disorder may not generally suppress elastic turbulence. Additionally, while studies in 2D provide a straightforward way to visualize the flow and thereby yield powerful insights, such models differ in their connectivity, porosity, and complexity from 3D pore spaces; therefore, it is unclear how results obtained in 2D can be extrapolated to 3D media. As a result, despite its fundamental importance and strong impact in applications, why the macroscopic flow resistance of polymer solutions anomalously increases in porous media is still unknown.

In this chapter, by directly visualizing the flow of a polymer solution in a transparent three-dimensional (3D) porous medium, **we demonstrate that this anomalous increase is indeed dominated by the added dissipation arising from elastic turbulence**. We find that the transition to unstable flow in each pore is continuous, arising due to the increased temporal persistence of discrete bursts of instability above an onset flow rate; however, this onset value varies from pore to pore. Thus, unstable flow is spatially heterogeneous across the different pores of the medium, with unstable and laminar regions coexisting. Guided by these findings, we quantitatively establish that the energy dissipated by unstable pore-scale fluctuations generates the anomalous increase in flow resistance through the entire medium. Our results thus help to resolve this long-standing puzzle. Moreover, by linking the onset of unstable flow at the pore scale to flow resistance at the macroscale, our work yields generally-applicable guidelines for predicting and controlling polymer solution flows.

3.1 Anomalous increase in macroscopic flow resistance coincides with the pore-scale onset of elastic turbulence.

We model disordered 3D porous medium using consolidated random packing of borosilicate glass beads (Figure 3.1A) of porosity $\varphi \approx 0.41$ (fabrication details in §A.4). Such bead packings have well-demonstrated reproducibility in pore size statistics and flow properties that can often be generalized to other, more complex media.[159] The polymeric fluid used is a dilute solution of high molecular weight (18 MDa) partially hydrolyzed polyacrylamide (HPAM) in a viscous aqueous solvent, formulated to precisely match its refractive index to that of the glass beads—thus rendering the medium transparent when saturated (Formulation B in §A.1). Additionally dispersing a dilute fraction of fluorescent latex microparticles (200 nm diameter), which act as flow tracers, therefore enables monitoring of the flow field using confocal microscopy (§A.4.2) and measurement of the two-dimensional (2D) fluid velocities $\mathbf{u}$ in the pore space *via* particle image velocimetry (PIV) (§A.5.1). We characterize the macroscopic flow behavior by injecting the polymer solution into the medium at a constant volumetric flow rate Q and measuring the corresponding steady-state pressure drop $\langle \Delta P \rangle_t$ across the medium; the angled brackets indicate an average over time t (Fig. 3.2).

For a Newtonian fluid, the relationship between pressure drop and flow rate is given by Darcy's law: $\langle \Delta P \rangle_t / \Delta L = \eta (Q/A)/k$, where η is the fluid dynamic shear viscosity measured using shear rheology (Fig. A.2), and ΔL, A, and k are the length, cross sectional area, and absolute permeability of the medium, respectively. For a polymer solution, for which the viscosity can change depending on flow conditions, this relationship is still employed in practice, but with η replaced by the "apparent viscosity" $\eta_{\text{app}} \equiv \frac{\langle \Delta P \rangle_t / \Delta L}{(Q/A)/k}$ that repre-

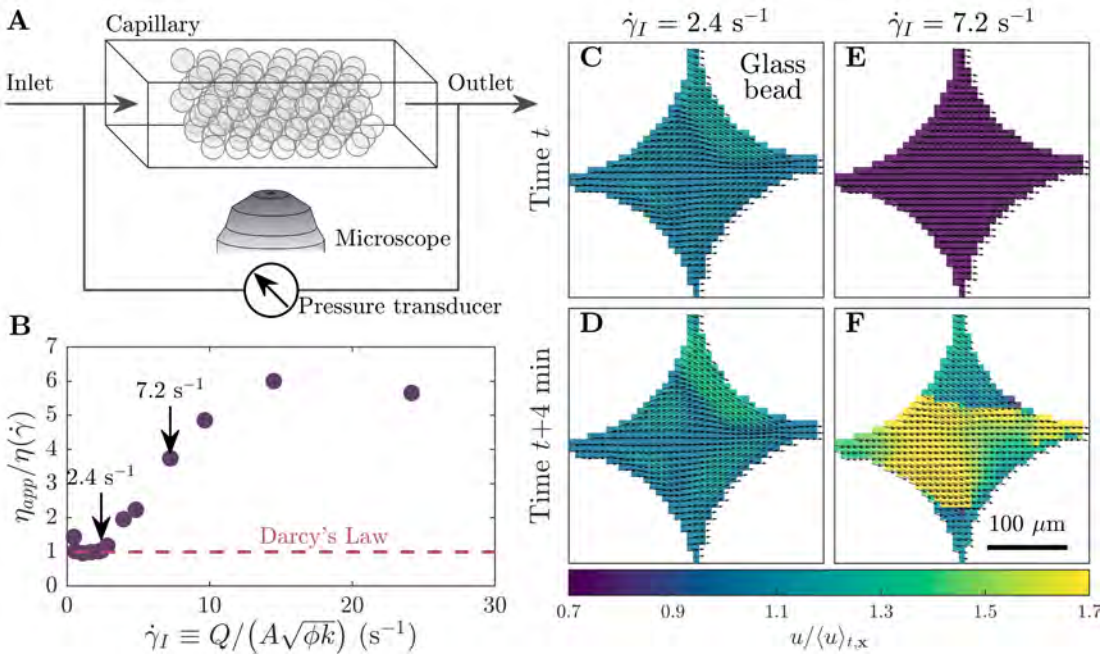

Figure 3.1: Pore-scale visualization reveals that the anomalous increase in flow resistance coincides with the onset of elastic turbulence. **(A)** Our porous medium is a lightly-sintered random packing of borosilicate glass beads confined in a quartz capillary with a square cross section. We inject the polymer solution containing fluorescent tracers into the medium using a syringe pump, and simultaneously image the flow in situ using a confocal microscope while measuring the pressure drop across the medium using differential pressure transducers. **(B)** Above a threshold flow rate, parameterized by the characteristic shear rate $\dot{\gamma}_I$, the macroscopic pressure drop, represented by the reduced apparent viscosity $\eta_{\text{app}}/\eta(\dot{\gamma}_I)$, anomalously increases and deviates from the prediction of Darcy's Law given by the shear viscosity of the bulk solution. **(C-F)** Flow visualization in an example pore; applied flow is left to right. Arrows indicate the vector field, and colors indicate the velocity magnitude $u = |\mathbf{u}|$ normalized by its value averaged spatially over the pore and temporally over the entire duration of the experiment, $\langle u\rangle_{t,\mathbf{x}} = \langle|\mathbf{u}|\rangle_{t,\mathbf{x}}$. **(C-D)** At a low flow rate, the flow does not change over time. **(E-F)** At a higher flow rate, the flow exhibits strong spatio-temporal fluctuations characteristic of elastic turbulence.

sents the macroscopic flow resistance. To facilitate comparison to the bulk shear viscosity, we therefore represent the pressure drop measurements by plotting the reduced apparent viscosity $\eta_{\text{app}}/\eta(\dot{\gamma}_I)$ as a function of the interstitial shear rate $\dot{\gamma}_I \equiv \frac{Q/(\varphi A)}{\sqrt{k/\varphi}}$ defined using the characteristic pore flow speed $Q/(\varphi A)$ and length scale $\sqrt{k/\varphi}$;[137,160] because all the other parameters are independently known, this relationship provides a direct mapping from the measured pressure drop to the apparent viscosity. As expected, at low flow rates, $\eta_{\text{app}} = \eta(\dot{\gamma}_I)$. However, above a critical flow rate corresponding to $\dot{\gamma}_I \approx 4\,\text{s}^{-1}$, η_{app} increasingly exceeds $\eta(\dot{\gamma}_I)$, eventually peaking at $\approx 6\eta(\dot{\gamma}_I)$ as shown in Fig. 3.1B; the corresponding pressure drop data reflect the same behavior, as shown in Fig. 3.2A. Pressure drop measurements taken while ramping up (dark blue) and down (light green) flow rate show no measurable hysteresis (Fig. 3.2B), similar to observations in model 2D porous media,[14,15,161] though polymer solution flows do exhibit hysteretic behavior in other geometries.[80,162] This anomalous increase and eventual peak in the macroscopic flow resistance parallels previous reports.[12,44,123,149–151]

Simultaneous visualization of the pore-scale flow provides a clue to the underlying reason for this anomalous increase. Fig. 3.1C–F shows the velocity field within an example pore measured at two different times. At low flow rates, for which $\eta_{\text{app}} = \eta(\dot{\gamma}_I)$, the flow is laminar and steady over time (Fig. 3.1C–D, Movie 3.1). Strikingly, concomitant with the anomalous increase in flow resistance, we observe strong spatial and temporal fluctuations in the flow at high flow rates (Fig. 3.1E–F)—despite the negligible influence of inertia in the flow, as indicated by the Reynolds number $\text{Re} \lesssim 10^{-4} \ll 1$. As shown in Movie 3.2, the fluid pathlines continually cross and vary over time, indicating the emergence of an elastic instability.

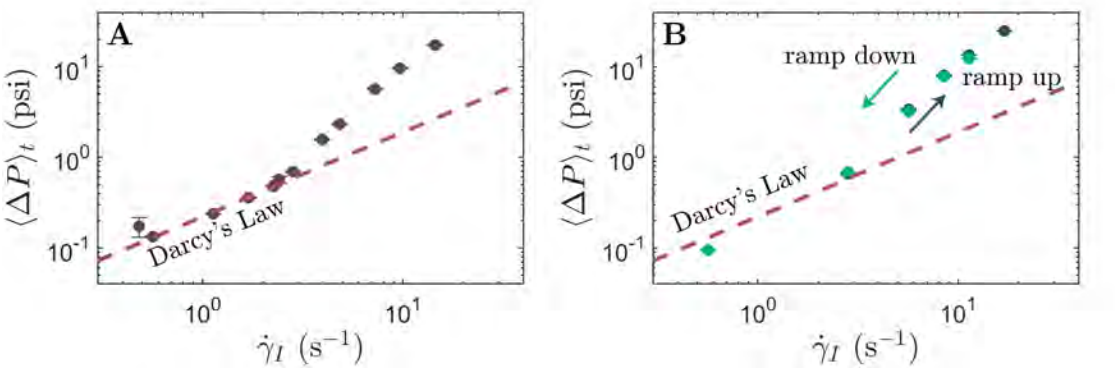

Figure 3.2: Raw pressure drop data at different imposed flow rates. **A** Time-averaged pressure drop data corresponding to Figs. 1B and 4C. Red dashed line shows the prediction of Darcy's Law using the shear viscosity of the bulk solution. Error bars represent one standard deviation of the pressure drop measurements taken over a 1 h measurement window; when not shown, error bars are smaller than the symbol size. **B** Pressure drop measurements taken while ramping up (dark blue) and down (light green) flow rate show no measurable hysteresis, similar to observations in model 2D porous media.[14,15,161]

3.2 Unstable fluctuations are chaotic in space and time

To characterize the spatial and temporal scales associated with unstable flow fluctuations, we subtract the temporal mean from each velocity vector, point-by-point, to focus on the velocity fluctuations $\mathbf{u}' = \mathbf{u} - \langle \mathbf{u} \rangle_t$. We monitor the fluctuations in two pore above the instability onset ($\mathrm{Wi}_I = 3.9$ and 4.4) for 60 s (Movie 3.5, Fig. 3.3). Still-frames show the instantaneous velocity fluctuation at an example time-point (Fig. 3.3A), and kymographs taken at a vertical line of pixels at the pore center line show how these bursts of fluctuations grow and decay in time Fig. 3.3B).

We use the measured time-dependent velocity field to directly compute the frequency- and wavenumber-dependent power spectral density of flow fluctuations, as shown in Fig. 3.4. These power spectra indicate that the fluctuating velocity fields are chaotic in both space and time, exhibiting power law decays with exponents $\beta \sim 1.1$ to 1.4 and $\alpha \sim 0.8$ to

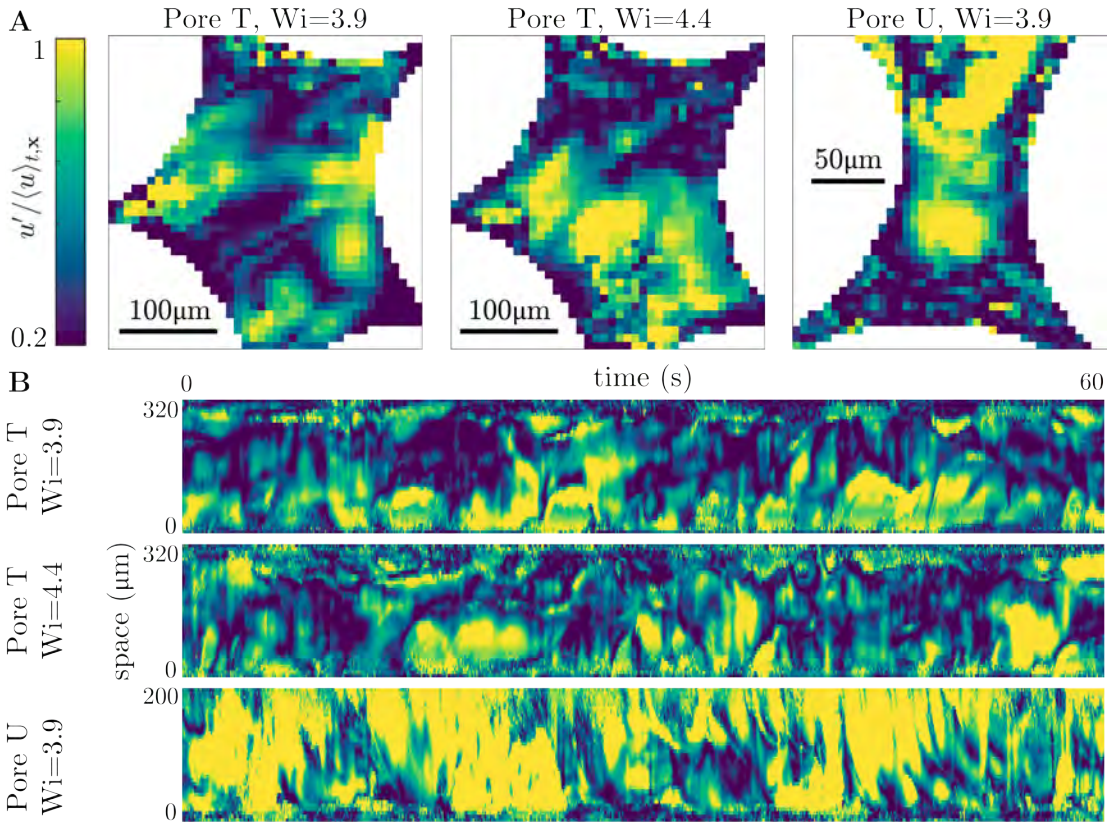

Figure 3.3: Characterization of spatiotemporal fluctuations in flow velocity. **A** Magnitude of velocity fluctuations u' normalized by the mean velocity $\langle u \rangle_{t,\mathbf{x}}$ for a pore at $\mathrm{Wi}_I = 3.9$, the same pore at $\mathrm{Wi}_I = 4.4$, and another pore at $\mathrm{Wi}_I = 3.9$. Pore labels are described in Table A.3. **B** Accompanying kymograph of fluctuations taken from a vertical line along the center of each pore (spatially averaging 3 pixels in the x-direction). The PIV frame rate of 6 frames per second shows finer time resolution than Fig. 3.5A-D, allowing for the spectral analysis shown in Fig. 3.4.

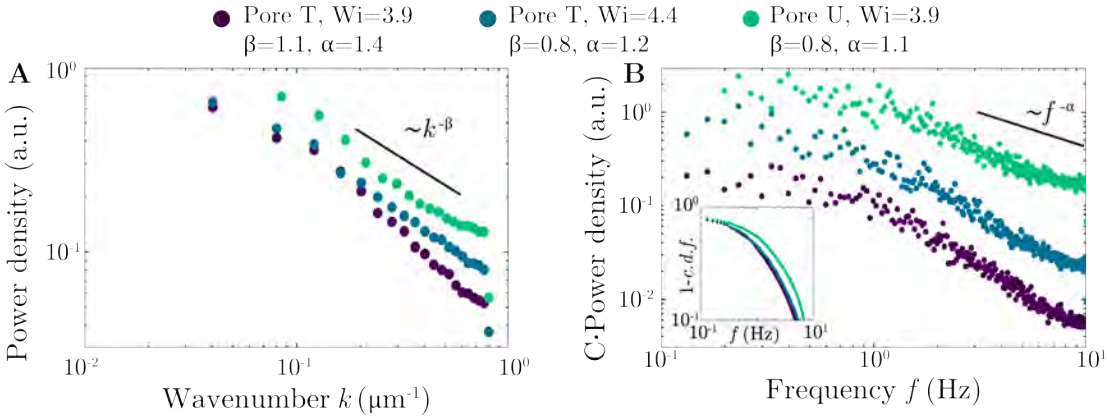

Figure 3.4: Spatial and temporal power spectra of velocity fluctuations. **A** The Fourier transform of the spatial signal $u'(x)$ averaged over the temporal points in the kymograph to smooth out noise. Best fit power-law scalings decay with wave numbers $\sim k^{-\beta}$ with $\beta \approx -0.8$ to 1.1, in agreement with the range $\beta \approx 1$ to 3 reported for elastic turbulence in various other geometries.[80,85,163,164] The upper wavenumbers are limited by the pixel size 0.62 μm, and the lower wavenumbers are limited by the frame size (200 or 320 μm). **B** The Fourier transform of the temporal signal $u'(t)$, averaged to smooth noise over 3 time points and a box of pixels taken from the center of the pore (10×7 for pore T, 5×13 for pore U), vertically shifted by a constant factor for clarity (C = 1 for pore T at $\mathrm{Wi}_I = 3.9$, C = 2 for pore T at $\mathrm{Wi}_I = 4.3$, C = 6 for pore U at $\mathrm{Wi}_I = 3.9$). Best fit power-law scalings decay with frequencies $\sim f^{-\alpha}$ with $\alpha = 1.1$ to 1.4. The upper frequency is capped at 2 Hz because of the PIV framerate and time averaging, and lower frequencies deviate $\lesssim .2$ Hz because of the finite experiment duration. These scalings agree with the broad range of $\alpha \approx 1$ to 3.7 reported for elastic turbulence in various other geometries.[11,15,85,120,161,164,165] Inset shows the complementary cumulative distribution function (*c.d.f.*) indicating that the majority of measured power spectral density is contained in fluctuations longer than one polymer relaxation time $\lambda \approx \mathrm{Wi}_I/\dot{\gamma}_I \approx 0.4$ s.

1.1, respectively. While these differ from some other previous reported exponents for elastic turbulence, they are consistent with the range of values observed for elastic turbulence in various other studies exploring different geometries and polymer solutions, which report exponents $\sim$ 1 to 4.6[11,15,80,85,120,161,163–165] and $\sim$ 1 to 3,[80,85] respectively. Investigating how these exponents vary across different geometries and solutions will be a useful direction for future work. Our visualization thus reveals that elastic turbulence *does* arise in 3D porous media, contrary to previous suggestions based on studies in 2D media that the disordered structure of the medium suppresses elastic turbulence.[15]

3.3 The pore-scale transition to fully unstable flow is continuous, with an onset that varies from pore to pore.

We next characterize the transition to elastic turbulence in our example pore from Fig. 3.1. Near the onset of the anomalous increase in flow resistance, flow fluctuations (blue in Fig. 3.5A-B) manifest as intermittent, abrupt bursts that coexist with the base laminar flow (purple in Fig. 3.5B), but quickly decay (Movie 3.3). Well above this onset, however, these fluctuations (blue-green-yellow in Fig. 3.5C) still coexist with the laminar flow, but persist over time (Fig. 3.5D, Movies 2.4–2.5); moreover, their normalized magnitudes are considerably larger (Fig. 3.6). Further examples corroborating this finding with higher-speed imaging are shown in Fig 3.3. Intriguingly, similar behavior is observed in the intermittent transition to inertial turbulence: for sufficiently large Re, discrete bursts of unstable flow appear and decay, persisting for longer durations as Re increases.[166] Thus, the transition to inertial turbulence is in many cases thought to be a non-equilibrium transition characterized by a continuously growing turbulent fraction.[167,168] Our results suggest the tantalizing possibility that the pore-scale transition to fully unstable flow—in this case, driven by an elastic instability—may similarly be a continuous non-equilibrium transition, as suggested recently in simulations.[164]

We test this hypothesis by measuring the fraction of time F_t a pore spends in the unstable state, as is often done to characterize the transition to inertial turbulence,[168] for 12 different pores over a broad range of flow rates. This quantity characterizes flow intermittency; in particular, as F_t increases, unstable bursts become more persistent over time, lasting for longer durations. Eventually, $F_t = 1$ corresponds to the turbulent state in which

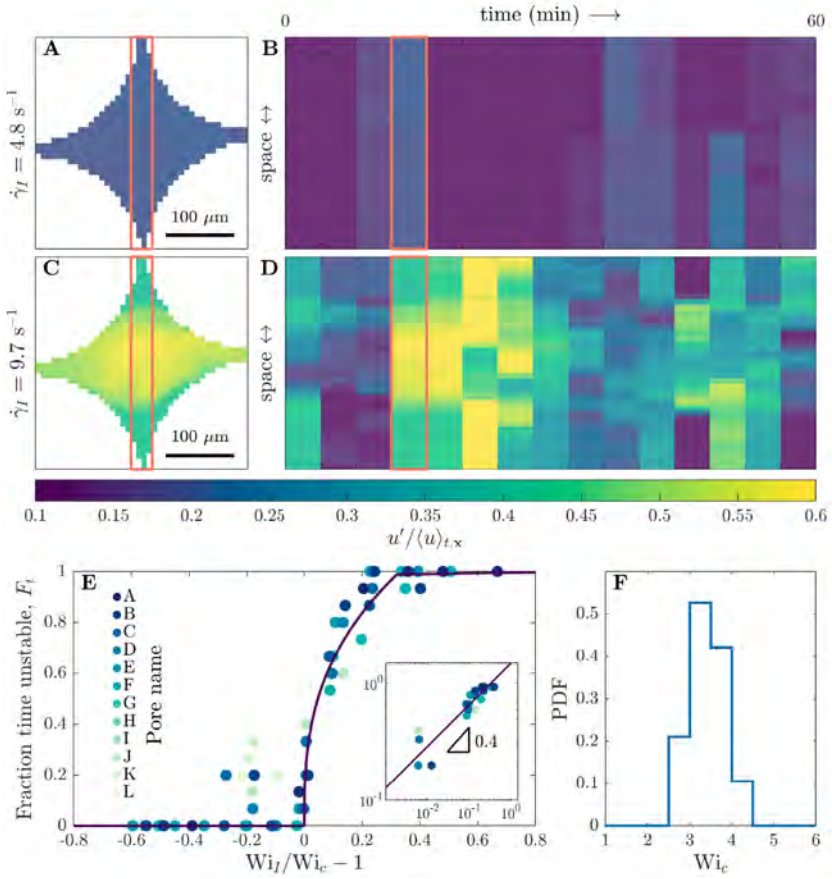

Figure 3.5: The pore-scale transition to elastic turbulence is a continuous non-equilibrium transition between distinct flow states. **(A-B)** Near the onset of elastic turbulence, flow fluctuations are intermittent and short-lived; **(A)** shows the normalized magnitude of flow fluctuations in a given pore at a given time, while **(B)** shows how the fluctuations in the red box vary over time. **(C-D)** Well above the onset of elastic turbulence, flow fluctuations are stronger and persist over time. **(E-F)** Continuous higher-speed imaging in another pore, also above the onset of elastic turbulence, again shows that flow fluctuations persist over time—even at short time scales. **(G)** The fraction of time F_t a pore spends in an unstable state ($u'/\langle u \rangle_{t,\mathbf{x}} > 0.2$) continually grows above a threshold flow rate, parameterized by the threshold Weissenberg number Wi_c. Different pores are characterized by different values of Wi_c, as shown by the probability density function in **(H)**; however, they all exhibit a similar transition to elastic turbulence as shown by the collapse of the measurements of F_t in **(G)** when the imposed Wi_I is rescaled by Wi_c for each pore. The inset shows the power-law scaling $F_t \sim (\mathrm{Wi}_I/\mathrm{Wi}_c - 1)^{0.4}$; the exponent is obtained from the best fit to the data, with an uncertainty of ± 0.1 determined by varying the instability threshold by $\pm 10\%$.

the flow is always unstable. Because the unstable flow is driven by polymer elasticity rather than fluid inertia, we describe the pore-scale transition to elastic turbulence using the characteristic Weissenberg number defined using the macroscopic imposed flow conditions, $\mathrm{Wi}_I \equiv N_1(\dot{\gamma}_I)/2\sigma(\dot{\gamma}_I)$; this parameter compares elastic stresses quantified by the first normal stress difference N_1 to viscous stresses quantified by the shear stress σ, and represents the upper limit of the spatially-varying local Weissenberg number (Fig. A.5). It can also be related to the largest destabilizing term in a linear stability analysis of the creeping flow limit of the Cauchy Momentum equation for a viscoelastic fluid.[76] For each pore, at low Wi_I, the flow is laminar and unchanging in time, with $F_t = 0$. Above a critical value Wi_c, however, the pore is unstable for a non-zero fraction of time, and F_t smoothly increases above zero. It eventually saturates at unity for $\mathrm{Wi}_I \gg \mathrm{Wi}_c$, indicating that the elastic turbulence has fully developed. Notably, this transition is general: while the critical value Wi_c varies from pore to pore (Fig. 3.5G), presumably due to the disordered structure of the pore space, F_t grows similarly with the rescaled $\mathrm{Wi}_I/\mathrm{Wi}_c$ for all 12 pores, as shown by the different colors in Fig. 3.5G—indicating a continuous phase transition. We observe some scatter in the data, possibly due to the influence of polydispersity in polymer properties and local correlations in the flow between neighbors; investigating these effects will be a useful direction for future work. However, in all cases, the data for Wi_I near Wi_c appear to follow the power-law scaling $F_t \sim (\mathrm{Wi}_I/\mathrm{Wi}_c - 1)^{0.4}$ (Fig. 3.5G, inset). Thus, the pore-scale transition to elastic turbulence is a continuous phase transition reminiscent of the intermittent transition to inertial turbulence.[164,166]

An unexpected consequence of the pore-to-pore variability in Wi_c, which ranges from $\mathrm{Wi}_{c,min} \approx 2.6$ to $\mathrm{Wi}_{c,max} \approx 4.4$ (Fig. 3.5H), is that the occurrence of elastic turbulence is

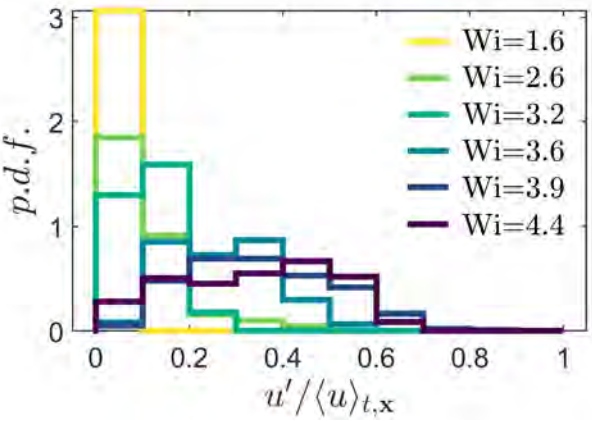

Figure 3.6: Distribution of the magnitude of flow fluctuations u' normalized by the mean $\langle u\rangle_{t,\mathbf{x}}$ in a representative pore B at different imposed Weissenberg numbers. For the laminar $\mathrm{Wi}_I = 1.6$, the fluctuations are contained near zero, representing experimental PIV noise. At higher Wi_I, the fluctuations grow in magnitude, and hence the persistence of bursts above our chosen threshold $u'/\langle u\rangle_{t,\mathbf{x}} > 0.2$ increase continuously.

spatially heterogeneous throughout the medium. In particular, because some pores become unstable at different values of Wi_I than others, unstable pores coexist amid stable, laminar pores for Wi_I in this range. An example is shown in Fig. 3.7, which displays the normalized root mean square of the flow fluctuations u' over time, $u'_{rms}/\langle u\rangle_{t,\mathbf{x}}$ for three different pores. At low flow rates and therefore Wi_I, all three pores are stable, as shown in the first column. As flow rate and therefore Wi_I is increased, Pore A ($2.6 < \mathrm{Wi}_c \leq 3.2$) becomes unstable first, while Pores B–C remain stable, as shown in the second column. At a higher Wi_I, Pore B ($3.2 < \mathrm{Wi}_c \leq 3.6$) next becomes unstable, as shown in the third column. Finally, at an even higher Wi_I, Pore C ($3.9 < \mathrm{Wi}_c \leq 4.4$) also becomes unstable, as shown in the last column. Thus, as Wi_I increases from ≈ 2.6 to 4.4, an increasing fraction of pores become unstable. This observation that single pores exposed to the same macroscopic flow rate become unstable in different ways provides a fascinating pore-scale analog of "molecular individualism,"[169] in which single polymers exposed to the same extensional flow elongate

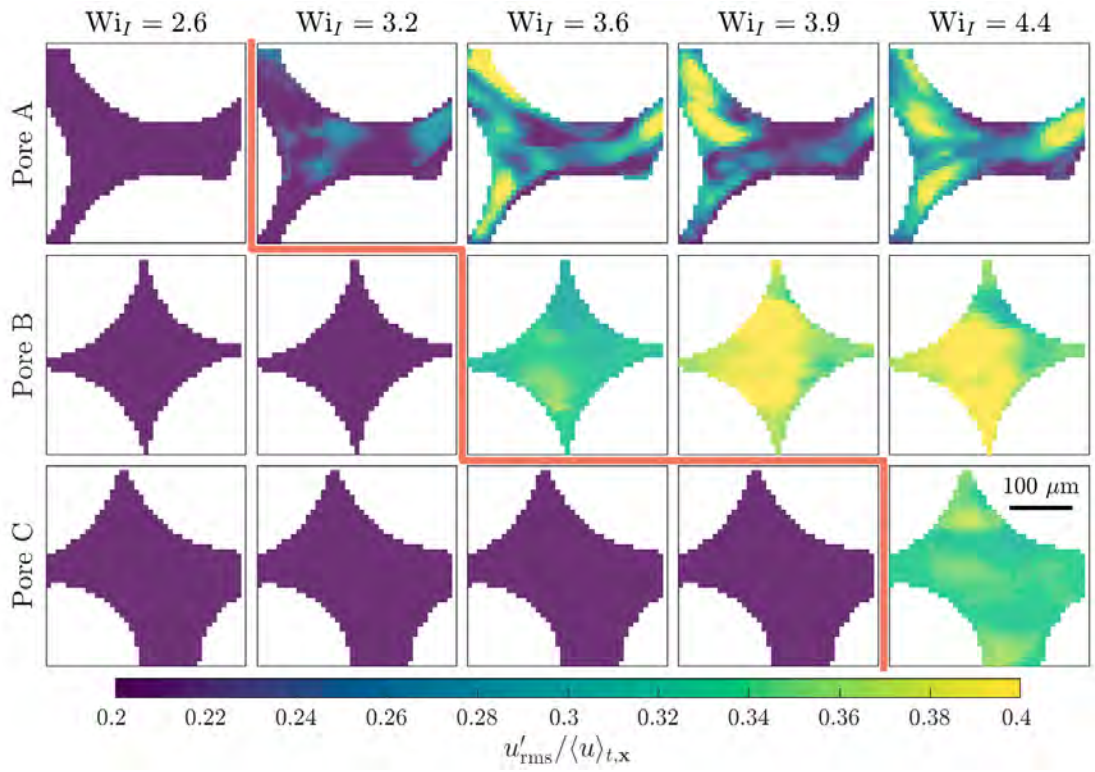

Figure 3.7: The occurrence of elastic turbulence is spatially heterogeneous throughout a porous medium, reflecting "porous individualism". Images show the normalized magnitude of root mean square flow fluctuations over 60 min in different pores and at different flow rates, parameterized by Wi_I. Applied flow is left to right. Pore A becomes unstable at the lowest flow rate, as shown by the red line in the first row. Pore B becomes unstable at the next highest flow rate, shown by the red line in the second row. Pore C becomes unstable only at even higher flow rates.

in different ways; we therefore term it "porous individualism". Indeed, monitoring a larger field of view spanning multiple pores on a side confirms that the flow states in neighboring pores are not appreciably correlated (Fig. A.6).

3.4 Simplified power balance enables pore-scale flow fluctuations to be linked to macroscopic transport.

How does this variability in the occurrence of elastic turbulence impact the macroscopic flow resistance? Motivated by the similarities between elastic and inertial turbulence revealed by our pore-scale imaging, as well as by previous studies in a range of simplified geometries,[14,80,154] we hypothesize that the flow fluctuations that arise in elastic turbulence impart additional viscous dissipation to the flow—akin to fluctuations in inertial turbulence. Just as the power dissipation for a Newtonian fluid is given by $\Phi = \mu\dot{\gamma}^2$ and the excess dissipation for inertial turbulence is given by $\Phi' = \mu\langle \mathbf{s}' : \mathbf{s}' \rangle$,* we find that the power dissipation of elastic turbulence can similarly be estimated as $\langle \chi \rangle_{t,V} = \eta \langle \mathbf{s}' : \mathbf{s}' \rangle$. In this section, we derive this *unstable dissipation function* explicitly, outlining and justifying the necessary assumptions.

3.4.1 Full derivation of power balance

We quantify this hypothesis using the power density balance for viscous-dominated flow. We start with the scalar partial differential equation for the rate of change of mechanical

*The unstable dissipation function Φ'[17] or equivalently the turbulent kinetic energy dissipation ε.[121]

energy per unit volume, obtained by dotting the Cauchy momentum equation with velocity:[17]

$$\frac{\partial}{\partial t}\left(\frac{1}{2}\rho u^2\right) + \nabla \cdot \frac{1}{2}\rho u^2 \mathbf{u} - P\nabla \cdot \mathbf{u} + \nabla \cdot [\tau \cdot \mathbf{u}] - \rho \mathbf{u} \cdot \mathbf{g} = -\nabla \cdot P\mathbf{u} - \tau : \nabla \mathbf{u}, \quad (3.1)$$

where $\mathbf{u}(\mathbf{x}, t)$ is the fluid velocity, ρ is the fluid density, $P(\mathbf{x}, t)$ is the fluid pressure, $\tau(\mathbf{x}, t)$ is the fluid stress tensor, and $\mathbf{g}$ is gravitational acceleration.

The first term $\frac{\partial}{\partial t}\left(\frac{1}{2}\rho u^2\right)$ represents the change in kinetic energy, which is of order Re and thus negligible. The second term $\nabla \cdot \frac{1}{2}\rho u^2 \mathbf{u}$ represents the acceleration over a control volume; this term disappears, since the inlet and outlet of our capillary have the same surface area, so there is no acceleration across the medium. The third term $P\nabla \cdot \mathbf{u}$ represents the reversible work of compression, which is negligible for an incompressible fluid $\nabla \cdot \mathbf{u} = 0$. The fourth term $\nabla \cdot [\tau \cdot \mathbf{u}]$ represents viscous work done across control surfaces; this term disappears, since there is no viscous work done at the capillary walls and the flow is unidirectional across the inlet and outlet control surfaces. The fifth term $\rho \mathbf{u} \cdot \mathbf{g}$ represents gravitational work done, which scales with the Reynolds and Froude numbers: $\rho \mathbf{u} \cdot \mathbf{g} \sim \mathrm{Re}/\mathrm{Fr}^2 = \rho g D_p^2/\eta_0 \approx 0.0028 \ll 1$ and is thus negligible. This leaves only the last two terms for our experiments:

$$-\nabla \cdot P\mathbf{u} = \tau : \nabla \mathbf{u}. \quad (3.2)$$

The left hand side represents the rate of work done by the fluid pressure and the right hand side represents the rate of viscous energy dissipation, per unit volume. The velocity gradient tensor can be decomposed into a symmetric and asymmetric component $\nabla \mathbf{u} = \mathbf{s} + \omega$,

where $\mathbf{s} = (\nabla\mathbf{u} + \nabla\mathbf{u}^{\mathrm{T}})/2$ is the rate of strain tensor and $\omega = (\nabla\mathbf{u} - \nabla\mathbf{u}^{\mathrm{T}})/2$ is the vorticity tensor.

3.4.2 Macroscopic averaging

Taking the volume integral of Eq. 3.2 and applying the divergence theorem to the left hand side yields the macroscopic power balance over the control volume. This volume is composed of the four capillary walls and a surface perpendicular to the walls well upstream and downstream of the bead packing, such that the flow is unidirectional $\mathbf{u} = u_x\hat{\mathbf{x}}$ across the inlet/outlet surfaces $\mathbf{n} = \pm\hat{\mathbf{x}}$:

$$\begin{aligned} -\int_{\mathscr{A}} P\mathbf{u}\cdot\mathbf{n}\mathrm{d}A &= \int_V \tau : (\mathbf{s}+\omega)\mathrm{d}V \\ \implies (Q/A)A\Delta P &= V\langle\tau : (\mathbf{s}+\omega)\rangle_V \\ \implies \frac{\Delta P}{\Delta L} &= \frac{\langle\tau : (\mathbf{s}+\omega)\rangle_V}{Q/A}. \end{aligned} \tag{3.3}$$

3.4.3 Time averaging

Drawing inspiration from the treatment of inertial turbulence, in which flows similarly exhibit strong spatio-temporal fluctuations, we decompose the velocity into a time-averaged and a fluctuating component $\mathbf{u}(\mathbf{x},t) = \mathbf{u}_0(\mathbf{x}) + \mathbf{u}'(\mathbf{x},t)$, from which it follows that the rate of strain and vorticity tensors also decompose $\mathbf{s}(\mathbf{x},t) = \mathbf{s}_0(\mathbf{x}) + \mathbf{s}'(\mathbf{x},t)$ and $\omega(\mathbf{x},t) = \omega_0(\mathbf{x}) + \omega'(\mathbf{x},t)$. The pressure similarly decomposes into a mean and fluctuating component $P(\mathbf{x},t) = P_0(\mathbf{x}) + P'(\mathbf{x},t)$, with $\langle P'\rangle_t = 0$ and thus $\langle P\rangle_t = P_0$. The time-averaged pressure drop is obtained by taking the time average $\langle\ \rangle_t = \frac{1}{t_c}\int_{-t_c/2}^{+t_c/2}(\ )\mathrm{d}t$ of Eq. 3.3 over a moving window $t = \pm t_c/2$, where t_c is a sufficiently large time window for

meaningful averaging:[170]

$$\frac{\langle \Delta P \rangle_t}{\Delta L} = \frac{\langle \langle \tau : (\mathbf{s} + \omega) \rangle_t \rangle_V}{Q/A}. \tag{3.4}$$

3.4.4 Neglect of strain history effects

In principle, Eq. 3.4 provides a direct link between the measured pore-scale flow field, quantified on the right hand side, and macroscopic pressure drop, given on the left hand side, as explored in recent simulations.[119] However, in practice, evaluating the right hand side of Eq. 3.4 requires knowledge of the full dependence of the stress τ on polymer strain history in 3D,[16] which is currently inaccessible in our experiments. Nevertheless, two features of the flow, detailed below, motivate the development of a simplified version of Eq. 3.4 that permits us to examine the influence of unstable pore-scale flow fluctuations on macroscopic transport.

First, while the flow fluctuates strongly over a broad range of time scales, the majority of the measured spectral power is contained in fluctuations occurring over a duration longer than the characteristic polymer relaxation time λ (complementary cumulative density function of the power spectral density show in figure 3.4). We therefore approximate the measured time-dependent flow as being quasi-steady over the polymer relaxation time, enabling us to adopt a generalized Newtonian fluid approach[16] in which the stress is parameterized by the shear viscosity η_s, which is a function of the local strain rate, and the extensional viscosity η_e, which is a function of accumulated strain in the quasi-steady flow field.

Second, analysis of the measured flow field indicates that polymers do not accumulate appreciable Hencky strain during advection through the tortuous pore space. We assess the role of extensional viscosity by directly computing the strain history of sample fluid ele-

ments along Lagrangian paths in the flow field measured in three representative pores. For a selected fluid element voxel, we use the measured time-dependent 2D velocity field to compute its propagation; specifically, using the pixel-by-pixel local velocity $d\mathbf{x}/dt = \mathbf{u}(\mathbf{x}, t)$, we compute the time to move to the next voxel as $\Delta t \approx \Delta x/u(\mathbf{x}, t)$, where Δx is the pixel size and $u(\mathbf{x}, t)$ is the local velocity magnitude. For this computed pathline, we then compute the accumulated Hencky strain over one polymer relaxation time $\lambda = \mathrm{Wi}/\dot{\gamma}_I = 0.3$ to 1 s as $\varepsilon = \int_0^\lambda \dot{\varepsilon}(\mathbf{x}, t)dt$. We perform this measurement for five different starting locations throughout a pore for each of the 15 quasi-steady flow field snapshots, and repeat this set of 75 measurements for three different pores, to obtain a representative distribution of Hencky strains. The resulting distributions for each flow rate show that Hencky strains are much smaller than 1 (Fig. 3.8), suggesting that extensional viscosity effects can be neglected, which typically arise when $\varepsilon \gtrsim 2$ to 3.[171] Thus, while local polymer extension drives the onset of the unstable flow, accumulated extension is likely not a strong contributor to the global viscous dissipation as is often suggested;[34–38] we therefore neglect any polymer contributions to the extensional viscosity and take the Newtonian limit of the Trouton ratio $\mathrm{Tr} \equiv \eta_e/\eta_0 = 3$.

3.4.5 Generalized Newtonian Decomposition

These two assumptions then allow us to decompose the dissipation function $\langle \tau : \nabla \mathbf{u} \rangle_t$ into a mean and fluctuating component. Because our calculations of Hencky strain described above suggest that extensional viscosity does not appreciably contribute to the global viscous dissipation, we express the fluid stress as a function of the local rate of strain tensor, $\tau_{ij}(s_{ij})$.[137] Since the stress is nonlinear for a non-Newtonian fluid, the function for stress

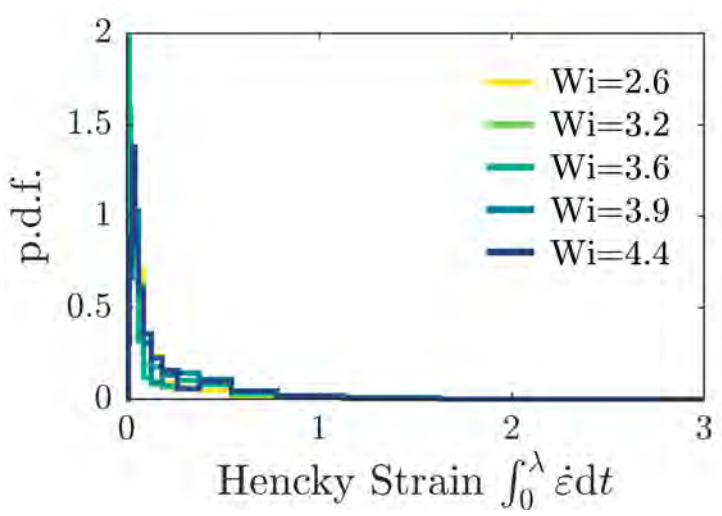

Figure 3.8: Distribution of measured Hencky strains along sample pathlines of duration $\lambda_0 \approx 1$ s. Colors indicate different macroscopic flow rates (reported as Wi_f). Distributions are taken over three pores, each with five sample track starting locations, and 15 time points with differing flow fields.

$\tau_{ij}(s_{0,ij} + s'_{ij})$ cannot easily be separated into a mean and fluctuating term; instead, we expand τ_{ij} with a Maclaurin series, applying the definition of fluctuations $\langle s'_{ij} \rangle_t \equiv 0$ and $\langle \omega'_{ij} \rangle_t \equiv 0$, but $\langle s'^2_{ij} \rangle_t \neq 0$:

$$
\begin{aligned}
&\langle \tau_{ij}|_{s_{0,ij}+s'_{ij}}(s_{ij}+\omega_{ij})\rangle_t \\
&\quad = \left\langle \left(\tau_{ij}|_{s_{0,ij}} + \left.\frac{\partial \tau_{ij}}{\partial s_{ij}}\right|_{s_{0,ij}} s'_{ij} + \frac{1}{2}\left.\frac{\partial^2 \tau_{ij}}{\partial s_{ij}^2}\right|_{s_{0,ij}} s'^2_{ij} + \frac{1}{3}\left.\frac{\partial^3 \tau_{ij}}{\partial s_{ij}^3}\right|_{s_{0,ij}} s'^3_{ij} + \mathcal{O}(s'^4_{ij}) \right) \right. \\
&\qquad \left. \left(s_{0,ij} + \omega_{0,ij} + s'_{ij} + \omega'_{ij}\right) \right\rangle_t \\
&\quad = \underbrace{\tau_{ij}|_{s_{0,ij}}\left(s_{0,ij}+\omega_{0,ij}\right)}_{\text{Mean flow: Darcy}} + \underbrace{\left[\left.\frac{\partial \tau_{ij}}{\partial s_{ij}}\right|_{s_{0,ij}} + \frac{s_{0,ij}+\omega_{0,ij}}{2}\left.\frac{\partial^2 \tau_{ij}}{\partial s_{ij}^2}\right|_{s_{0,ij}} \right] \langle s'^2_{ij} \rangle_t}_{\text{Unstable flow: } \langle \chi \rangle_t} + \mathcal{O}(\langle s'^4_{ij} \rangle_t),
\end{aligned}
\tag{3.5}
$$

which is accurate to fourth order $\mathcal{O}(\langle s'^4_{ij} \rangle_t)$. The first term reflects the viscous dissipation of the mean flow, ultimately yielding Darcy's law when volume averaged, by definition:

$\langle \tau_{ij}|_{s_{0,ij}}(s_{0,ij}+\omega_{0,ij})\rangle_V/(Q/A) = \eta(\dot{\gamma}_I)(Q/A)/k$. The second term reflects viscous dissipation due to unstable flow fluctuations, and we define it as the rate of added dissipation $\langle\chi\rangle_t$, analogous to the unstable dissipation function Φ' (or TKE dissipation ε) defined in inertial turbulence.[17,121]

3.4.6 Unstable dissipation function

The term in square brackets in Eq. 3.5 has units of a dynamic viscosity, prompting the *ansatz* that it should be proportional to $\eta(\dot{\gamma}_0)$, where $\dot{\gamma}_0 \equiv 2s_{0,xy} = \partial u_0/\partial y + \partial v_0/\partial x$ and c_{ij} is the proportionality constant:

$$\begin{aligned}\langle\chi\rangle_t &\equiv \left[\left.\frac{\partial\tau_{ij}}{\partial s_{ij}}\right|_{s_{0,ij}} + \frac{s_{0,ij}+\omega_{0,ij}}{2}\left.\frac{\partial^2\tau_{ij}}{\partial s_{ij}^2}\right|_{s_{0,ij}}\right]\langle s_{ij}'^2\rangle_t \\ &\equiv c_{ij}\eta(\dot{\gamma}_0)\langle s_{ij}'^2\rangle_t. \end{aligned} \tag{3.6}$$

For a power-law fluid, $\tau_{ij} = A_s(s_{ij})^{\alpha_s}$, where A_s and α_s are material constants. This constitutive relationship allows us to compute c_{ij}:

$$\begin{aligned} c_{ij}\eta(\dot{\gamma}_0) &\equiv \left.\frac{\partial\tau_{ij}}{\partial s_{ij}}\right|_{s_{0,ij}} + \frac{s_{0,ij}+\omega_{0,ij}}{2}\left.\frac{\partial^2\tau_{ij}}{\partial s_{ij}^2}\right|_{s_{0,ij}} \\ &= \alpha_s A_s s_{0,ij}^{\alpha_s-1}\left(1 + \frac{s_{0,ij}+\omega_{0,ij}}{s_{0,ij}}\frac{(\alpha_s-1)}{2}\right) \\ &= \alpha_s 2^{1-\alpha_s}\left(1 - (1+\Lambda_{ij})\frac{(1-\alpha_s)}{2}\right)\eta(\dot{\gamma}_0), \end{aligned} \tag{3.7}$$

where, assuming isotropic unstable flow fluctuations, $\eta(s_{0,ij}) \approx \eta(s_{0,xy}) \equiv \eta(\dot{\gamma}_0/2)$.

The term $\Lambda_{ij} \equiv \omega_{0,ij}/s_{0,ij}$ cannot be directly measured from a 2D flow field; simple

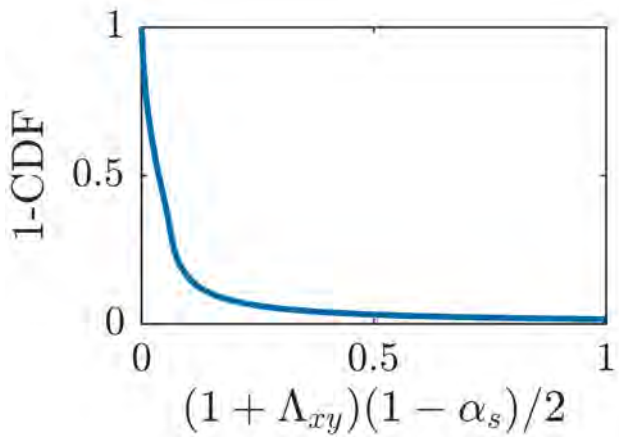

Figure 3.9: Magnitude estimate of correctional term in simplified power balance. The complementary cumulative distribution function of the in-plane component of the correctional term $(1+\Lambda_{xy})(1-\alpha_s)/2$, distributed over all tested flow rates and pixels. For a vast majority of pixels, the magnitude of this term is much less than 1. The average value of $\langle(1+\Lambda_{xy})(1-\alpha_s)/2\rangle_{v,Q} = 0.026 \ll 1$ indicates that $1-(1+\Lambda_{xy})(1-\alpha_s)/2 \approx 1$.

averaging for the unknown elements in the third direction k would trivially return $\Lambda_{ik} = 0$. However, estimating the magnitude of Λ_{ij} using just the in-plane component indicates that the entire term is typically much less than order one: averaging over all pixels and flow rates yields $\langle(1+\Lambda_{ij})(\alpha_s-1)/2\rangle_{V,Q} = 0.026 \ll 1$, as shown in Fig. 3.9. We therefore neglect this term. Thus, $c = \alpha_s 2^{1-\alpha_s}$; $c = 1$ for a Newtonian fluid and $0 < c < 1$ for shear-thinning fluids. Using our measured fluid rheology, we find $c = 0.98$—reflecting that our fluid has nearly constant shear viscosity for the shear rates tested.

The unstable dissipation function $\langle\chi\rangle_t$ then depends primarily on the fluctuating rate of strain tensor $\langle s_{ij}'^2\rangle_t$. Again assuming isotropic flow fluctuations, as is frequently done in the

case of inertial turbulence,[172,173]

$$\left\langle \left(\frac{\partial u_z'}{\partial z}\right)^2 \right\rangle_t \approx \frac{1}{2}\left[\left\langle \left(\frac{\partial u_x'}{\partial x}\right)^2 \right\rangle_t + \left\langle \left(\frac{\partial u_y'}{\partial y}\right)^2 \right\rangle_t\right]$$

$$\left\langle \left(\frac{\partial u_x'}{\partial z}\right)^2 \right\rangle_t \approx \left\langle \left(\frac{\partial u_y'}{\partial z}\right)^2 \right\rangle_t \approx \left\langle \left(\frac{\partial u_z'}{\partial x}\right)^2 \right\rangle_t \approx \left\langle \left(\frac{\partial u_z'}{\partial y}\right)^2 \right\rangle_t$$

$$\approx \frac{1}{2}\left[\left\langle \left(\frac{\partial u_x'}{\partial y}\right)^2 \right\rangle_t + \left\langle \left(\frac{\partial u_y'}{\partial x}\right)^2 \right\rangle_t\right]$$

$$\left\langle \left(\frac{\partial u_x'}{\partial z}\frac{\partial u_z'}{\partial x}\right) \right\rangle_t \approx \left\langle \left(\frac{\partial u_y'}{\partial z}\frac{\partial u_z'}{\partial y}\right) \right\rangle_t$$

$$\approx -\frac{1}{4}\left[\left\langle \left(\frac{\partial u_x'}{\partial x}\right)^2 \right\rangle_t + \left\langle \left(\frac{\partial u_y'}{\partial y}\right)^2 \right\rangle_t\right]$$

$$\implies \langle \chi \rangle_t \equiv c\eta(\dot{\gamma}_0)\langle s_{ij}'^2 \rangle_t$$

$$\approx c\eta(\dot{\gamma}_0)\left[2\left\langle \left(\frac{\partial u_x'}{\partial x}\right)^2 \right\rangle_t + 2\left\langle \left(\frac{\partial u_y'}{\partial y}\right)^2 \right\rangle_t + 3\left\langle \left(\frac{\partial u_y'}{\partial x}\right)^2 \right\rangle_t\right.$$

$$\left. + 3\left\langle \left(\frac{\partial u_x'}{\partial y}\right)^2 \right\rangle_t + 2\left\langle \frac{\partial u_y'}{\partial x}\frac{\partial u_x'}{\partial y} \right\rangle_t\right]. \tag{3.8}$$

This quantity, which quantifies the rate of added viscous dissipation due to unstable flow fluctuations, can now be fully determined from our PIV measurements. Though our computations use the full form shown in Eq. 3.8, we can analogously write this as $\langle \chi \rangle_t \approx \eta \langle \mathbf{s}' : \mathbf{s}' \rangle_t$, as is typically done for the analogous term in inertial turbulence $\mu \langle \mathbf{s}' : \mathbf{s}' \rangle_t$[†].

Crucially, we can directly measure the rate of added dissipation $\langle \chi \rangle_t$ using flow visual-

[†]The turbulent kinetic energy dissipation is generally given the symbol ε, which we avoid here to prevent overlap with the Hencky strain. We also avoid use of the term kinetic energy dissipation, since in our low Re flows this term is more appropriately thought of as a dissipation of mechanical energy.

ization in each pore; an example is shown in Fig. 3.10A. Consistent with our expectation, the rate of local viscous dissipation sharply increases by nearly three orders of magnitude at the onset of elastic turbulence, and continues to increase as Wi_I increases above Wi_c (Fig. 3.10A, green/yellow regions), suggesting indeed that viscous dissipation associated with shear fluctuations at the pore scale may explain the anomalous rise in macroscopic flow resistance.

3.4.7 Apparent viscosity

Having computed the unstable dissipation rate, averaged across the medium $\langle \chi \rangle_{t,V}$, we use this quantity to determine the overall apparent viscosity of the flowing polymer solution. We substitute $\langle \chi \rangle_{t,V}$ into Eqs. 3.4-3.5 to obtain our final result:

$$\begin{aligned} \frac{\langle \Delta P \rangle_t}{\Delta L} &\equiv \frac{\eta_{\mathrm{app}}}{k}\frac{Q}{A} \\ &\approx \underbrace{\frac{\eta(\dot{\gamma}_I)(Q/A)}{k}}_{\text{Darcy's law}} + \underbrace{\frac{\langle \chi \rangle_{t,V}}{(Q/A)}}_{\text{Fluctuations}} + \left\{ \begin{array}{c} \text{Strain} \\ \text{history} \\ \text{effects} \end{array} \right\}, \end{aligned} \tag{3.9}$$

or rearranging for apparent viscosity:

$$\eta_{\mathrm{app}}(\dot{\gamma}_I) = \eta(\dot{\gamma}_I) + \frac{k\langle \chi \rangle_{t,V}}{(Q/A)^2} + \left\{ \begin{array}{c} \text{Strain} \\ \text{history} \\ \text{effects} \end{array} \right\}. \tag{3.10}$$

Eq. 3.10 thus provides a way to quantitatively link the pore-scale flow fluctuations arising in elastic turbulence and the anomalous increase in macroscopic flow resistance. In

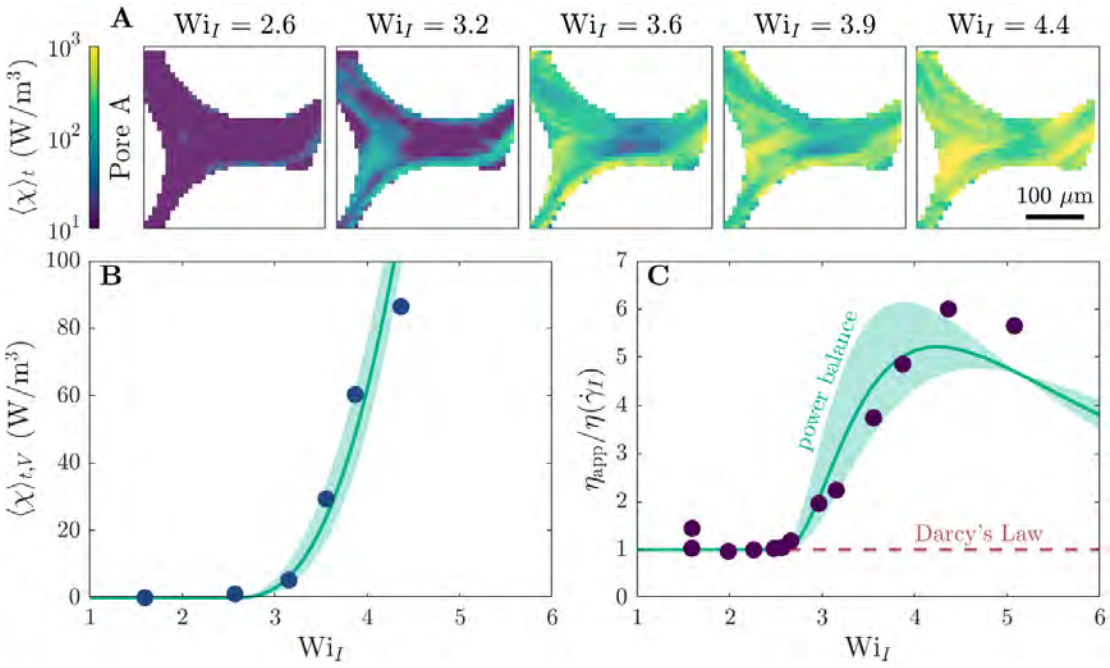

Figure 3.10: Anomalous increase in macroscopic flow resistance is determined by the added viscous dissipation due to unstable flow fluctuations. **(A)** The rate of added viscous dissipation $\langle\chi\rangle_t$ directly measured from flow visualization for the example of Pore A sharply increases above the onset of elastic turbulence. **(B)** Averaging the spatially-averaged $\langle\chi\rangle_t$ over all pores imaged yields the overall added viscous dissipation, which increases as a power law $\sim (\mathrm{Wi}_I/\mathrm{Wi}_c - 1)^{2.6}$ above the macroscopic threshold $\mathrm{Wi}_c \approx 2.6$, as shown by the green curve. **(C)** The measured power-law fit to $\langle\chi\rangle_{t,V}$ enables prediction of the macroscopic apparent viscosity η_{app} *via* the power balance Eq. 3.10, as shown by the green curve and detailed in the SI; the uncertainty associated with the fit to $\langle\chi\rangle_{t,V}$ (shaded region in **(B)**) yields an uncertainty in this prediction, as shown by the shaded region. Points indicate the independent measurements of η_{app} from the macroscopic pressure drop.

particular, as a first step toward this goal, we will neglect the third term in what follows and examine the influence of the first two terms. Importantly, all the components of these first two terms are controlled or can be directly determined in our experiments. In particular, we directly compute $\langle \chi \rangle_{t,V}$ by averaging $\langle \chi \rangle_t$ over the imaged area of each pore, and then averaging over all the imaged pores. As anticipated, the overall rate of added dissipation increases as a greater fraction of pores becomes unstable (Fig. 3.10B, symbols), consistent with a power-law scaling $\langle \chi \rangle_{t,V} = A_x(\mathrm{Wi}/\mathrm{Wi}_c - 1)^{\alpha_x}$. We fit $A_x = 279 \pm 1\ \mathrm{W/m^3}$ and $\alpha_x = 2.6 \pm 0.4$, as shown by the green curve in Fig. 3.10 (shaded regions show error in fit).

Incorporating this empirical relationship for $\langle \chi \rangle_{t,V}$ in our simplified form of Eq. 3.10 then yields a final prediction for the dependence of the apparent viscosity η_{app} on the imposed Wi_I (Fig. 3.10C, green curve) that is derived directly from our pore-scale imaging of the unstable flow fluctuations. Remarkably, this prediction shows excellent agreement with the macroscopic pressure drop measurements (Fig. 3.10C, symbols) without employing any fitting parameters. This agreement confirms that the anomalous increase in the macroscopic flow resistance is primarily due to the added dissipation arising from the flow fluctuations generated by pore-scale elastic turbulence.

A simple picture for the sigmoidal variation of η_{app} with flow rate, observed in our experiments (Fig. 3.1B) as well as in numerous previous studies,[12,44,123,149–151] thereby emerges. At low flow rates, corresponding to $\mathrm{Wi}_I < \mathrm{Wi}_{c,min}$, all of the pores in the medium are laminar and steady over time; thus, $\eta_{\mathrm{app}} = \eta(\dot{\gamma}_I)$. As flow rate is increased, Wi_I eventually exceeds $\mathrm{Wi}_{c,min} \approx 2.6$ in our experiments, causing an increasing fraction of pores to become unstable. The added viscous dissipation due to the flow fluctuations in these pores then causes η_{app} to increasingly exceed $\eta(\dot{\gamma}_I)$ (Fig. 3.10C, 8^{th}–12^{th} points). Eventually, as

Wi_I exceeds $\mathrm{Wi}_{c,max} \approx 4.4$ in our experiments, all of the pores are unstable. Further increases in Wi_I do not appreciably generate additional flow fluctuations, and η_{app} saturates (Fig. 3.10C, last point). The steepness of the increase of η_{app} with flow rate therefore reflects the distribution of the different Wi_c; while these values depend on the complex 3D geometry of each pore and are challenging to predict *a priori*,[76] reducing the polydispersity of the medium likely sharpens the distribution of Wi_c and thus steepens the increase in η_{app}, consistent with the results of studies in 2D obstacle arrays.[108] As the flow rate is increased further, we expect that η_{app} eventually converges back to $\eta(\dot{\gamma}_I)$, reflecting the increased relative influence of viscous dissipation from the base laminar flow—although strain history effects, inertia, and chain scission will likely also play a role in this regime, imparting new complexities to the flow.

3.4.8 Origin of the peak in $\eta_{\mathrm{app}}\,(\mathrm{Wi}_I)$

The power balance quantified by Eq. 3.9 yields a peak in $\eta_{\mathrm{app}}\,(\mathrm{Wi}_I)$, in good agreement with the experimental measurements, as shown in Fig. 3.10C. As described below, this peak reflects the Wi_I-dependence of the dissipation rate of chaotic flow fluctuations $\langle\chi\rangle_{t,V} \sim (\mathrm{Wi}_I/\mathrm{Wi}_c - 1)^{\alpha_x}$. In particular, to have a peak in $\eta_{\mathrm{app}}\,(\mathrm{Wi}_I)$ at $\mathrm{Wi}_I = \mathrm{Wi}_p > \mathrm{Wi}_c$,

$$
\begin{aligned}
0 &= \frac{\mathrm{d}}{\mathrm{d}(\mathrm{Wi}_I)}\left(\frac{\langle\chi\rangle_{t,V}}{(Q/A)^2}\right)_{\mathrm{Wi}_p} \\
0 &= \frac{\mathrm{d}}{\mathrm{d}(\mathrm{Wi}_I)}\left(\frac{(\mathrm{Wi}_I - \mathrm{Wi}_c)^{\alpha_x}}{\mathrm{Wi}_I^{2/(\alpha_n-\alpha_s)}}\right)_{\mathrm{Wi}_p} \\
\implies \mathrm{Wi}_p &= \frac{2\mathrm{Wi}_c}{2 - \alpha_x(\alpha_n - \alpha_s)}.
\end{aligned}
\tag{3.11}
$$

where in the second line we have applied the definition of the Weissenberg number and the measured rheological relationships shown in Fig. A.2, which yield $Q \sim \dot{\gamma}_I \sim \mathrm{Wi}_I^{1/(\alpha_n-\alpha_s)}$. Thus, we expect that the measured apparent viscosity will anomalously increase beyond the Darcian baseline for $\mathrm{Wi} > \mathrm{Wi}_c$ and will peak when $\mathrm{Wi} = \mathrm{Wi}_p$ as given above. Fitting our experimental data yields $\mathrm{Wi}_c = 2.6, \alpha_x = 2.6, \alpha_n = 1.23, \alpha_s = 0.934$, yielding a predicted peak at $\mathrm{Wi}_I = \mathrm{Wi}_p = 4.4$, in excellent agreement with our measured $\mathrm{Wi}_{c,max} = 4.4$. For even larger $\mathrm{Wi}_I > \mathrm{Wi}_p$, the dissipation rate due to chaotic flow fluctuations $\langle\chi\rangle_{t,V}$ does not increase with Wi_I as quickly as $(Q/A)^2$, and our analysis suggests that η_{app} decays back to η — indicating that the viscous dissipation associated with the base laminar flow increasingly dominates, although strain history effects, inertia, and chain scission will likely also play a role in this regime. Investigating these high Wi_I effects, and more generally investigating the underpinnings of the dependence of $\langle\chi\rangle_{t,V}$ on Wi_I, will be a useful direction for future research.

3.4.9 Upper bound estimate for the contribution from strain history effects

Motivated by our observation that most of the unstable flow fluctuations are slow (on time scales longer than λ), we develop an upper bound estimate of the last term in Eq. 3.9:

$$\eta_{\mathrm{app}}(\dot{\gamma}_I) = \eta(\dot{\gamma}_I) + \frac{k\langle\chi\rangle_{t,V}}{(Q/A)^2} + \frac{k\langle\xi\rangle_{t,V}}{(Q/A)^2}, \tag{3.12}$$

where the last term ξ is defined analogously to reflect strain history effects. In general, this is history dependent, but we expect that it will be bounded by the steady state extensional viscosity expected for the polymer solution. In particular, the additional polymer contri-

bution to extensional viscosity $\eta_{e,p}$ can provide at most a viscous dissipation of $\eta_{e,p}\dot{\varepsilon}^2$, and hence:

$$\frac{k\langle\xi\rangle_{t,V}}{(Q/A)^2} < \frac{k\langle\eta_{e,p}\dot{\varepsilon}^2\rangle_{t,V}}{(Q/A)^2}, \tag{3.13}$$

where as a strict upper bound, we take Tr $\longrightarrow$ 1000 or $\eta_{e,p} \sim 10^3\eta_0$.[171] Following previous work,[12,35] we estimate the characteristic extensional rate as $\dot{\varepsilon} \approx Q/(\varphi_V A)/D_p \sim 0.1$ to 0.6 s^{-1} in our experiments, where D_p is the mean bead diameter. Given that our measurements of Hencky strain indicate negligible extension in the pore bodies, we approximate the fraction of the total volume over which the maximal extension takes place as $d_t^3/\left(d_t^3 + d_b^3\right)$, where $d_t = 0.16D_p$ and $d_b = 0.24D_p$ are the pore throat and body diameters for a bead packing, respectively. Thus, we estimate:

$$\begin{aligned}\langle\eta_{e,p}\dot{\varepsilon}^2\rangle_{t,V} &\sim \left(10^3\eta_0\right)\left[Q/(\varphi_V A)/D_p\right]^2\left[d_t^3/\left(d_t^3 + d_b^3\right)\right] \\ &\sim 0.6 \text{ to } 20 \text{ W/m}^3.\end{aligned} \tag{3.14}$$

The entire term of Eq. 3.13 is then $\sim$ 0.6 at all tested Wi_I. Adding this term as an upper bound to the model of Eq. 3.9 gives the green region in Figure 3.11. The actual additional contribution of polymer-induced extensional viscous dissipation should fall somewhere in this region, since Hencky strains are unlikely to actually reach this infinite extension limit. This neglected contribution of polymer extensional viscosity in the pore throats can thus likely account for the $\sim$ 10% discrepancy between our model in 3.9 and the peak in the apparent viscosity. Quantifying the exact role of this term requires modeling the full strain

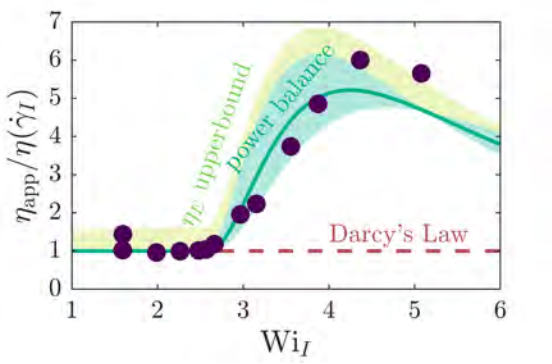

Figure 3.11: Upper bound estimate of excess extensional viscous dissipation. Reproduction of Fig. 3.10C, with added region to indicate upper bound expectation for the role of excess extensional viscous dissipation due to polymer elongation, as detailed in section 3.4.9.

history of polymers in the unstable flow field, and will be an important direction for future work.

3.5 Conclusions

Though well documented,[12,44,123,149–151] the anomalous flow resistance exhibited by polymer solutions in porous media has evaded explanation for over half a century. Many have speculated that this phenomenon is due to the onset of elastic turbulence, given that elastic instabilities have been reported to generate increased flow resistance in a range of simplified geometries.[44,80,111,152–155] However, a quantitative link between the associated flow fluctuations in a porous medium—if they exist—and the macroscopic flow resistance has remained elusive. Indeed, whether elastic turbulence even arises in disordered 3D porous media has been recently called into question.[15] Our experiments help to resolve this uncertainty by providing the first visualization of elastic turbulence in disordered 3D porous

media. Furthermore, by quantitatively linking the pore-scale features of elastic turbulence to macroscopic transport, our work establishes that the energy dissipated by unstable pore-scale fluctuations generates the anomalous increase in flow resistance. More broadly, our findings that the pore-scale transition to elastic turbulence is a continuous non-equilibrium phase transition akin to the intermittent transition to inertial turbulence, and that the resulting dissipation similarly controls macroscopic transport behavior, highlight the connections between these distinct forms of turbulence.

For simplicity, our analysis does not consider the full polymer strain history in 3D. Instead, motivated by the observations that the flow is quasi-steady and does not appreciably accumulate strain over a polymer relaxation time, we use a generalized Newtonian fluid model that successfully captures $\approx 90\%$ of the measured peak in the flow resistance, as well as the overall sigmoidal shape of $\eta_{\text{app}}(\dot{\gamma}_I)$. This close agreement suggests that while local polymer extension generates unstable flow fluctuations, the resulting viscous dissipation of the fluid itself is the primary contributor to the overall flow resistance—not the polymer extensional viscosity, as is often thought to be the case.[34–38] Similar behavior has been considered in analyses of elasto-inertial turbulence, where polymer stretching is thought to be highly transient and localized.[174] However, we do observe slight discrepancies between our model prediction and the pressure drop measurements, particularly at the largest flow rates tested (last two points in Fig. 3.10C); we anticipate that strain history effects play a non-negligible role in this regime, as suggested by a calculation of the added contribution due to the steady state extensional viscosity (Fig. 3.11). Incorporating these effects into our analysis will be an important next step.

We expect our results to particularly impact geological applications involving polymer

solution flows in porous media, given that polymers with relaxation times λ as long as ~ 10 s[44] are regularly used to aid the removal of trapped non-aqueous liquids from subsurface formations during groundwater remediation[32] and oil recovery[21,123]. Our results suggest that elastic turbulence may arise in these settings: we find that the transition to unstable flow occurs for $\mathrm{Wi} \gtrsim \mathrm{Wi}_c \approx \lambda\dot{\gamma}_I \sim 1$, corresponding to interstitial shear rates $\dot{\gamma}_I$ and flow speeds Q/A exceeding $\sim 0.1\ \mathrm{s}^{-1}$ and $\sim 0.1\ \mu\mathrm{m\ s}^{-1}$, respectively[1] —well within the range encountered in the field. Thus, by deepening fundamental understanding of how macroscopic transport behavior depends on imposed flow conditions and solution properties, our analysis yields guidelines for predicting and controlling polymer solution flows in such settings. Moreover, because such flows also play key roles in determining separation performance in filtration[147] and chromatography,[148] improving heat and mass transfer in microfluidic devices,[152,175,176] and enabling extrusion-based manufacturing,[177] we expect these results to inform a broader range of applications.

3.6 Supplementary Movie Captions

The movies corresponding to data in this chapter can be found with the online version of Browne and Datta, 2021 (DOI: 10.1126/sciadv.abj2619)[3], and are duplicated in the repository at https://github.com/cabrowne/dissertation-movies.

Movie 3.1: Velocity field of example pore (pore B) just below onset of instability ($\dot{\gamma}_I = 2.6\ \mathrm{s}^{-1}$; $\mathrm{Wi}_I = 2.6$). Applied flow is left to right. Each frame is 4 min apart (720x speed). Arrows indicate the vector field, and colors indicate velocity magnitude as measured by particle image velocimetry (PIV). Velocities do not change appreciably over time above the error of PIV.

Movie 3.2: Velocity field of example pore (pore B) above onset of instability ($\dot{\gamma}_I = 7.3\ \mathrm{s}^{-1}$; $\mathrm{Wi}_I = 3.6$). Applied flow is left to right. Each frame is 4 min apart (720x speed). Arrows indicate the vector field, and colors indicate velocity magnitude as measured by particle image velocimetry (PIV). Velocities exhibit strong spatio-temporal fluctuations, consistent with the onset of an elastic instability.

Movie 3.3: Fluctuating velocity field of example pore (pore B) near cusp of instability ($\dot{\gamma}_I = 4.8\ \mathrm{s}^{-1}$; $\mathrm{Wi}_I = 3.2$). Applied flow is left to right. Each frame is 4 min apart (720x speed). Colors indicate fluctuating velocity magnitude as measured by particle image velocimetry (PIV). Right shows kymograph of fluctuating velocity field for an example column of pixels (marked by red lines). Puffs of fluctuations decay in time.

Movie 3.4: Fluctuating velocity field of example pore (pore B) well above onset of instability ($\dot{\gamma}_I = 9.7\ \mathrm{s}^{-1}$; $\mathrm{Wi}_I = 3.9$). Applied flow is left to right. Each frame is 4 min apart (720x speed). Colors indicate fluctuating velocity magnitude as measured by particle im-

age velocimetry (PIV). Right shows kymograph of fluctuating velocity field for an example column of pixels (marked by red lines). Fluctuations are sustained in time.

Movie 3.5: Fluctuating velocity field of example pore (pore B) well above onset of instability ($\dot{\gamma}_I = 9.7\ \mathrm{s}^{-1}$; $\mathrm{Wi}_I = 3.9$) shown at high time resolution. Applied flow is left to right. Each PIV frame averaged over over 1/6 s. Video shown at 5x speed. Colors indicate fluctuating velocity magnitude as measured by particle image velocimetry (PIV). Right shows kymograph of fluctuating velocity field for an example column of pixels (marked by red lines). Fluctuations are sustained in time.

They turned to the port together and saw the green world rising to meet their ship. "I wonder what it thinks of us?"

Ray Bradbury, Here there by Tygers

4

Harnessing resistance

Many key environmental, industrial, and energy processes—such as remediation of contaminated groundwater aquifers,[32,122] recovery of oil from subsurface reservoirs,[21,123] and extraction of heat from geothermal reservoirs[124]—rely on the injection of a fluid into a subsurface porous medium. Such media are formed by sedimentary processes, often leading to vertically-layered strata of distinct pore sizes oriented along the direction of macroscopic

flow.[178,179] The permeability differences between these strata cause uneven fluid partitioning across them, with preferential flow through higher permeability regions and "bypassing" of lower permeability regions.[124,180] This flow heterogeneity reduces the efficacy of contaminant remediation, oil recovery, and heat extraction from bypassed regions—necessitating the development of new ways to spatially homogenize the flow.

Low-molecular weight polymer additives have a long history of use in such applications to increase the injected fluid viscosity and thereby suppress instabilities, like viscous fingering, at immiscible (e.g., water-oil) interfaces.[21,32,123] However, this process of conformance control still suffers from the issue of uneven partioning of flow across different strata. Quantitatively, the superficial velocity in a given stratum i is given by Darcy's law, representing each stratum as a homogeneous medium with uniformly-disordered pores of a single mean size: $U_i \equiv Q_i/A_i = (\Delta P/L)k_i/\eta_{\text{app}}$, where Q_i is the volumetric flow rate through the stratum, ΔP is the pressure drop across a length L of the parallel strata, A_i and k_i are the cross-sectional area and permeability of the stratum, respectively, and η_{app} is the "apparent viscosity" of the polymer solution quantifying the macroscopic resistance to flow through the tortuous pore space. For low-molecular weight polymer additives, η_{app} is given by the dynamic shear viscosity η of the solution, and is typically not strongly dependent on flow rate. Therefore, differences in k_i result in differences in U_i between strata—leading to uneven partitioning of the flow across the entire stratified medium.

This chapter has been adapted from unpublished work by Christopher A. Browne, Richard B. Huang, Callie W. Zheng, and Sujit S. Datta. **Author Contributions:** C.A.B. performed all experiments; C.A.B. and R.B.H. developed the 2-layer parallel resistor model; C.A.B. and C.W.Z. developed the n-layer parallel resistor model; C.A.B. and S.S.D. designed the experiments, analyzed the data, discussed the results, and wrote the manuscript. S.S.D. designed and supervised the overall project.

Conversely, the apparent viscosity of a high-molecular weight polymer solution *can* depend on flow rate. For many such solutions, η_{app} strongly increases above a threshold flow rate in a homogeneous porous medium, even though η of the bulk solution decreases with increasing shear rate.[12,34–38,44,123,149–151,181] Our direct visualization of the flow in a homogeneous medium (chapter 3 [3]) established that this anomalous increase reflects the onset of a purely-elastic flow instability arising from the buildup of polymer elastic stresses during transport.[1,2,15,44,54,76–78,90,105,111,120,152–158] In particular, this instability leads to "elastic turbulence", in which the flow exhibits chaotic fluctuations reminiscent of inertial turbulence, despite the vanishingly small Reynolds numbers Re[14,80,154]—contributing added viscous dissipation that can generate this anomalous increase in η_{app}.[3] In a stratified medium, this flow rate-dependence of $\eta_{app,i}$ in each stratum may provide an avenue to break the proportionality between k_i and U_i, potentially mitigating the uneven partitioning of the flow across strata. However, this possibility remains unexplored; indeed, it is still unknown how the onset of elastic turbulence and associated increase in $\eta_{app,i}$ arise in each stratum.

In this chapter, **we demonstrate that elastic turbulence can indeed help homogenize flow in stratified porous media**. Using pore-scale confocal microscopy and macro-scale imaging of passive scalar transport, we visualize the flow in a model porous medium with two distinct strata, imposing a constant flow rate Q through the entire medium. For low Q, the flow in both strata is laminar, leading to the typical uneven partitioning of flow across the strata. Strikingly, for Q above a threshold value Q_1, elastic turbulence arises solely in the higher permeability stratum and fluid is redirected to the lower permeability stratum, helping to homogenize the flow. Above an even larger threshold Q_2, elastic turbulence also arises in this lower permeability stratum, suppressing this flow redirection—leading to a

window of flow rates at which this homogenization is optimized. Guided by these findings, we develop a parallel-resistor model that treats each stratum i as a homogeneous medium with specified A_i, k_i, and therefore, $\eta_{\text{app},i}$, all coupled at the inlet and outlet. This model quantitatively captures the overall pressure drop across the stratified medium as well as the observed flow redirection with varying Q. It also reveals the underlying cause of this redirection. In particular, above Q_1, preferential flow causes elastic turbulence to arise solely in the higher permeability stratum. The corresponding increase in the resistance to flow, as quantified by $\eta_{\text{app},i}$, redirects flow towards the lower permeability stratum. Above Q_2, the onset of elastic turbulence and corresponding increase in $\eta_{\text{app},i}$ in the lower permeability stratum redirects flow back towards the higher permeability stratum—yielding the experimentally-observed optimum in flow homogenization. Finally, we generalize this model, establishing the operating conditions at which this homogenization is optimized for porous media with arbitrarily many strata. Thus, our work provides a new approach to homogenize fluid and passive scalar transport in heterogeneous porous media. Since many naturally-occurring media are stratified, we anticipate these findings to be broadly useful in environmental, industrial, and energy processes.

4.1 Materials and Methods

To investigate the spatial distribution of flow in a stratified porous medium, we use imaging at two different length scales (Figure 4.1 A): macro-scale ($\sim$ 100′s pores) and pore-scale ($\sim$ 1 pore).

To characterize the macro-scale partitioning of flow, we fabricate an unconsolidated stratified porous medium in a Hele-Shaw assembly (§A.3). We 3-D print an open-faced rectangular cell, filled with spherical borosilicate glass beads of distinct diameters arranged in parallel strata of equal cross-sectional areas $A_C \approx A_F \approx A/2$. We tamp down the beads for 30 min to form a dense random packing with a porosity $\varphi_V \sim 0.4$[182] and screw the whole assembly shut with an overlying acrylic sheet cut to size, sandwiching a thin sheet of polydimethylsiloxane to provide a watertight seal. We impose a constant flow rate Q to introduce the test fluid—either the polymer solution or the polymer-free solvent, which acts as a Newtonian control. We measure the fully-developed pressure drop ΔP across the medium and determine the permeability via Darcy's law using experiments with pure glycerol, yielding $k = 270\ \mu\text{m}^2$, and an estimated permeability ratio between the strata of $\tilde{k} \equiv k_C/k_F \approx 26$ (§A.3). We then visualize the macro-scale scalar transport by the fluid by introducing a step change in the concentration of a dilute dye and record the infiltration of the dye front using a DSLR camera (§A.3.1). To track the progression of the dye as it is advected by the flow, we determine the "breakthrough" curve halfway along the length of the medium ($x = L/2$) by measuring the dye intensity C averaged across the entire medium cross-section, normalized by the difference in intensities of the final dye-saturated and initial dye-free medium, C_f and C_0, respectively: $\tilde{C} \equiv \left(\langle C\rangle_y - \langle C_0\rangle_y\right) / \left(\langle C_f\rangle_y - \langle C_0\rangle_y\right)$. Repeating this procedure for individual strata (subscript i) and tracking the variation of the stream-wise position X_i at which $\tilde{C}_i = 0.5$ with time provides a measure for the superficial velocity $U_i = \mathrm{d}X_i/\mathrm{d}t$ in each stratum.

To gain insight into the pore-scale physics, we use experiments in consolidated microfluidic assemblies (§A.4). We pack spherical borosilicate glass beads in square quartz capil-

laries, densify them by tapping, and lightly sinter the beads—resulting in a dense random packing with $\varphi_V \approx 0.41$.[183] We fabricate three different media: a homogeneous coarse medium (glass bead diameter $d_p = 300$ to 355 μm), a homogeneous fine medium ($d_p = 125$ to 155 μm), and a stratified medium with parallel coarse and fine strata, each composed of the same beads used to make the homogeneous media, again with equal cross-section areas, $\tilde{A} \approx 1$.[6,184] We again measure the fully-developed pressure drop ΔP across each medium, and determine the permeability via Darcy's law using experiments with pure water, yielding $k_C = 79$ and $k_F = 8.6$ μm^2 for the homogeneous coarse and fine media, respectively, and $k = 32$ μm^2 for the entire stratified medium—in reasonable agreement with our previous measurements of similar media[183] and with the prediction of the established Kozeny-Carman relation[185] (§A.4). The permeability ratio between the two strata is then $\tilde{k} \equiv k_C/k_F \approx 9$. For both assemblies, we define a characteristic shear rate of the entire medium $\dot{\gamma}_I \equiv Q/\left(A\sqrt{\varphi_V k}\right)$ as the ratio between the characteristic pore flow speed $Q/(\varphi_V A)$ and length scale $\sqrt{k/\varphi_V}$,[137,160] which range from $\dot{\gamma}_I \approx 0.2$ to 26 s^{-1} in all our experiments.

The polymer solution is a Boger fluid comprised of dilute ($c = 300$ ppm $\approx 0.5c^*$) of high molecular weight (18 MDa) partially hydrolyzed polyacrylamide (HPAM) dissolved in a viscous aqueous solvent (Formulation B A.1). To visualize the flow, we additionally seed our polymer solution with a dilute suspension of fluorescent tracer particles and inject the solution through the sintered 3D media at constant flow rate Q using *Harvard Apparatus* syringe pumps (§A.4.1). We monitor the flow after equilibration ($>$ 1 hour) using a *Nikon* A1R+ laser scanning confocal fluorescence microscope at various zooms (§A.4.2). We represent the movies thus obtained by intensity-averaging images over a time

scale $\approx$ 2.5 μm/ (Q/A), producing particle pathlines that well-approximate the instantaneous flow streamlines since the Péclet number remains above $\mathrm{Pe} > 10^5 \gg 1$.

4.2 Polymer solutions homogenize flow above threshold Weissenberg number

To image the macroscopically-uneven partitioning of flow between strata, we use our Hele-Shaw model stratified porous medium. First, we impose a low flow rate corresponding to $\mathrm{Wi}_I = 1.4$. We observe preferential flow through the coarse stratum, as indicated by the fast infiltration of dye through the coarse layer and slow infiltration of dye through the fine stratum (Figure 4.1B, movie 4.1). We monitor the dye concentration $\tilde{C}$ over time t at the midpoint $x = L/2$ of the porous medium (with a pore volume for half way through the medium $t_{\mathrm{PV},1/2} = A(L/2)/Q$). The distinct infiltration of dye through each stratum produces two disperse steps in the dye breakthrough to this point: the first jump from $\tilde{C} = 0$ to 0.4 at $t/t_{\mathrm{PV}} \approx 0.1$ to 0.3 corresponds to the relatively compact dye front moving through the coarsest layer, and the second gradual jump from $\tilde{C} = 0.4$ to 0.6 at $t/t_{\mathrm{PV}} \approx 0.3$ to 2 corresponds to the more diffuse dye front moving through the fine layer, which continues after the conclusion of the video (dark green line in Figure 4.1C). We then quantify the uneven partitioning of flow using the superficial velocity in each stratum, which we measure by tracking the position of the center of the disperse dye front ($\tilde{C} = 0.5$, averaged over the height of each stratum) over time, giving a superficial velocity of $U_C = 130$ μm/s in the coarse stratum and a 13x slower $U_F = 10$ μm/s in the fine stratum, giving a fairly

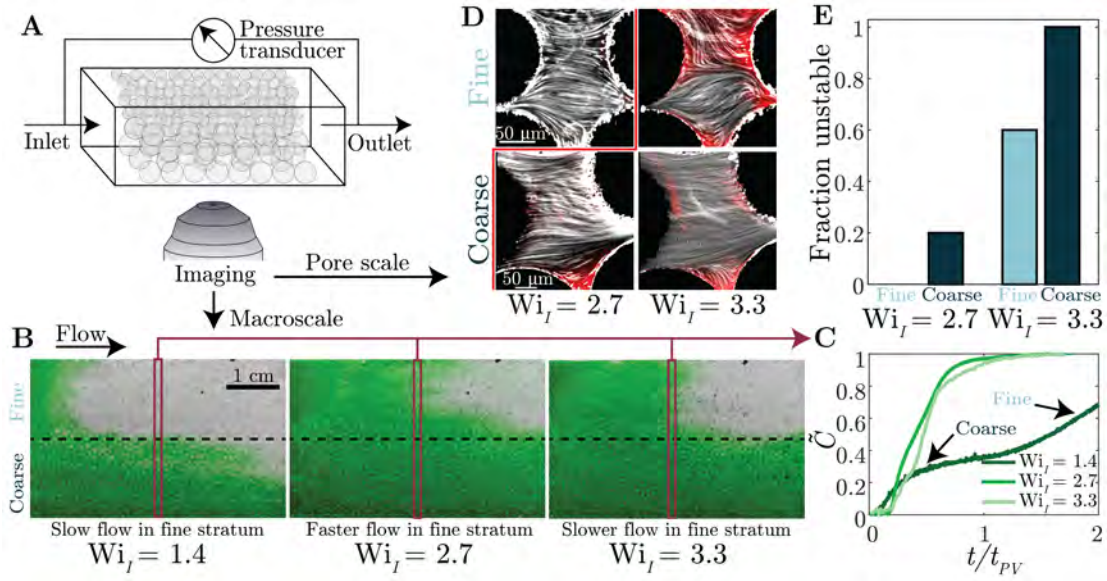

Figure 4.1: Flow homogenization between strata coincides with onset of elastic turbulence in only the coarse stratum. **A** Model stratified porous media with two strata of distinct glass bead sizes allows simultaneous pressure drop measurements and imaging at the macroscale or pore-scale. **B** Passive scalar transport visualized with a step change in dye through Hele-Shaw model stratified porous medium. Images at $t/t_{PV} = 0.5$ show farther progress of the dye from through the the coarse (bottom) than the fine (top) stratum. **C** Dye concentration $\tilde{C}$ at midpoint of medium $x = L/2$ shows fastest infiltration of the fine stratum for the intermediate $\mathrm{Wi}_I = 2.7$. **D** Streamline images of representative pores in microfluidic model stratified porous medium show that this homogenized partitioning of flow coincides with development of elastic turbulence only in the coarse stratum. Red overlay shows standard deviation in pixel intensity over course of video to indicate regions of large flow variation. The lessened homogenization effect at higher $\mathrm{Wi}_I = 3.3$ coincides with the onset of elastic turbulence in both strata. **E** Fraction of 10 observed pores in each stratum with unstable flow, defined using clear streamline crossing over 5 minute videos (Movies 3.4 and 3.5).

heterogeneous flow partitioning of $U_F/U_C = 0.075$ (Figure 4.3C). We observe similar behavior with a Newtonian control, using the same solvent without the addition of polymers, producing a similar relative flow difference of $U_F/U_C = 0.063$ even at a higher applied absolute flow rate of $Q = 35$ mL/hr (Movie 4.2). Hence, at low Wi_I, polymer solutions recapitulate the uneven partitioning of flow across strata characteristic of Newtonian fluids.

To investigate how increased elasticity alters this flow partitioning by injecting our polymer solution at a higher $\mathrm{Wi}_I = 2.7$ (matching $Q = 35$ mL/hr with the Newtonian solvent

control). Surprisingly, the uneven partitioning of flow is markedly reduced: the dye front infiltrates the fine stratum 2x faster (compared to the Newtonian baseline), nearly keeping pace with the infiltration of the coarse stratum. (Figure 4.1B, movie 4.3). We similarly see the distinct waves in the dye concentration $\tilde{C}$ merge into one continuous increase. The superficial velocity in each stratum further indicates that this faster flow through the fine stratum $U_F = 70$ μm/s (2x faster than the Newtonian baseline) is accompanied by slower flow through the coarse stratum $U_C = 540$ μm/s (1.1x slower than the Newtonian baseline), producing a 2.4x homogenizing improvement in the flow partitioning $\tilde{U}_F/\tilde{U}_C = 0.14$. Further increasing the flow rate $\mathrm{Wi}_I = 3.3$ ($Q = 45$ mL/hr) produces a less pronounced flow homogenization (Figure 4.1B, movie 4.4), delaying infiltration of the finest stratum (Figure 4.1C) and reducing the homogenization in flow partitioning ($\tilde{U}_F/\tilde{U}_C = 0.11$), suggesting that an intermediate Wi_I can provide optimal flow homogenization.

To gain insight into the physical origin of this flow homogenization, we use our microfluidic model stratified porous medium to directly image the flow at the pore-scale. We image 10 pores in each of the strata continuously for 5 min using confocal microscopy to produce streamline videos. At the moderate $\mathrm{Wi}_I = 2.7$—coinciding with flow homogenization—all pores in the fine stratum exhibit stable, steady flow: characterized by streamlines that do not change over the coarse of the video (Movie 4.5; representative pore shown in figure 4.1D). Surprisingly, however, 20% of the observed pores in the coarse layer exhibit unstable flow at the same macroscopically applied Wi_I, characterized by streamline motion and crossing over the coarse of the video (Figure 4.1E). We further highlight regions of unstable flow with a red overlay of the standard deviation of intensity projection on the streamline images. At the higher $\mathrm{Wi}_I = 3.3$—coinciding with reduced performance in flow

homogenization—pores in both strata exhibit unstable flow, shown by streamline crossing in the videos (Movie 4.6) and regions of red in the deviation overlay on streamline images (Figure 4.1D). Of the observed pores, 60% in the fine stratum and 100% in the coarse stratum are unstable (Figure 4.1E). We recently demonstrated this flow instability leads to elastic turbulence, and the viscous dissipation associated with shear fluctuations produces an increase in η_{app},[3] suggesting that differences in flow resistance between strata may underpin this flow homogenization.

How do differences in this pore-scale flow instability relate to macroscopic differences in superficial velocity between strata? To quantitatively understand this link between pore-scale flow instabilities and macroscopic flow redirection, we develop a simplified parallel resistor model, which treats the stratified medium as two independent homogeneous media coupled at the inlet and outlet but without cross flow. For the developed flow, the time averaged pressure drop $\langle \Delta P \rangle_t$ must be equal across both strata, so the imposed constant flow Q must partition into the coarse Q_C and fine Q_F strata according to their resistance to flow:

$$\langle \Delta P \rangle_t / \Delta L = \eta_{app,C} Q_C / (A_C k_C) = \eta_{app,F} Q_F / (A_F k_F) . \tag{4.1}$$

Recent measurements demonstrate that the onset of elastic turbulence in individual pores of a homogeneous medium produces excess viscous dissipation associated with shear fluctuations, leading to an increase in the macroscopic apparent viscosity η_{app} that grows as more pores become unstable.[3] In a stratified medium, it is unclear how this increase $\eta_{app,i}$ depends on the permeability of each stratum, so we first measure this dependence in homogeneous porous media of different grain sizes.

4.3 Apparent viscosity does not depend on grain size of porous medium

We inject our polymer solution into the two microfluidic model homogeneous porous media, each with a permeability matching the coarse or fine strata of the microfluidic stratified porous medium. We measure the time-averaged pressure drop $\langle \Delta P \rangle_t$, reported as the apparent viscosity $\eta_{\text{app}} \equiv k\left(\langle \Delta P \rangle_t / \Delta L\right) / \left(Q/A\right)$ (Fig.4.2A). At low Wi_I, the apparent viscosity equals the polymer shear viscosity $\eta_{\text{app}} = \eta\left(\dot{\gamma}_I\right)$, in agreement with Darcy's law. Above a threshold Wi_c, the apparent viscosity rises sharply, paralleling previous reports.[12,44,123,149–151] Though frequently attributed to extensional viscosity effects,[34–38] our recent work demonstrated that this resistance is instead dominated by the onset of elastic turbulence, which adds viscous dissipation *via* chaotic fluctuations in the strain rate field.[3] Intriguingly, both the coarse (dark blue points) and fine media (light blue points) deviate at the same Wi_c and produce the same η_{app} over the tested Wi_I range. To understand the similarity in excess resistance between media of different permeability, we directly image the pore-scale flow with confocal microscopy.

We monitor the flow in 10 pores in the fine medium for five minutes each after allowing the flow to equilibrate for one hour. As observed in the coarse medium,[3] at low Weissenberg numbers $\text{Wi}_I < 2.6$ the flow in the fine medium is stable and laminar in all pores (Movie 4.7). At higher Weissenberg numbers $\text{Wi}_I > 2.6$ the flow in some pores begins to fluctuate, as indicated by the crossing and dynamic evolution of the streamlines (Movie 4.8). Though each pore again has a different onset condition Wi_c, both the magnitude of fluctuations and number of unstable pores increases with Wi_I. To directly compute the excess viscous dissipation associated with this fluctuating flow field, we measure

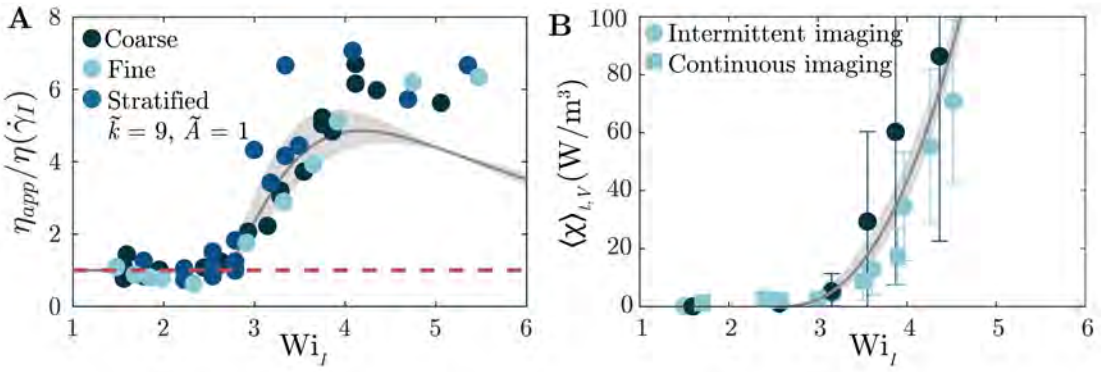

Figure 4.2: Elastic turbulence produces similar rise in apparent viscosity for porous media of different permeabilities and heterogeneities. A Pressure drop measurements show that the increase in apparent viscosity occurs above the onset of elastic turbulence is well characterized by Wi_I for homogeneous porous media of different grain sizes and for a heterogeneous porous medium with two strata, matching expectations for an effective homogeneous medium. Blue line is theory given by measured $\langle\chi\rangle_{t,V}$ in both homogeneous media. **B** Medium-averaged viscous dissipation associated with flow fluctuations $\langle\chi\rangle_{t,V}$ shows a general functional dependence on Wi_I for homogeneous media of different grain sizes. Error bars represent one standard deviation between pores. Shaded region represents error in power law fit.

the instantaneous 2D fluid velocities $\mathbf{u}$ *via* particle image velocimetry (PIV).[186] Subtracting off the mean flow in each pixel gives the fluctuating velocity field $\mathbf{u}' = \mathbf{u} - \langle\mathbf{u}\rangle_t$, from which we compute the fluctuating component of the fluctuating strain rate tensor $\mathbf{s}' = (\nabla\mathbf{u}' + \nabla\mathbf{u}'^{\mathrm{T}})/2$. The local viscous dissipation associated with the fluctuating flow field is then given directly by $\langle\chi\rangle_t = \eta\langle\mathbf{s}' : \mathbf{s}'\rangle_t$, which can be estimated from the 2D fields.[172,173] Figure 4.1C shows the spatial map of this viscous dissipation in an example pore in the coarse medium and the fine medium at different applied Wi_I. The spatial structure, magnitude, and critical onset condition of this dissipation varies from pore to pore, though it remains unclear how the disorder of the 3D pore space determines this "porous individualism." Averaging the dissipation across the 10 pores imaged continuously in the fine medium provides an estimate for the macroscopic flow resistance due to this instability that arises heterogeneously in each pore $\langle\chi\rangle_{t,V}$ (Fig. 4.1D, green squares). We additionally

compute this dissipation in the fine medium following the same long-duration intermittent imaging procedure used in chapter 3 (2 s every 4 min over the course of 1 hour, §A.4.2), which follows the same trend (Fig. 4.1D, green circles). The added viscous dissipation of fluctuations begins to grow sharply above $\mathrm{Wi}_c \approx 2.6$. Intriguingly, despite the difference in confining pore length scale set by the grain size, the excess dissipation in the fine medium matches the dissipation from the coarse medium (Fig. 4.1D purple points, reproduced from fig. 3.10). The best fit power law $\langle \chi \rangle_{t,V} = A_x(\mathrm{Wi}_I/\mathrm{Wi}_c - 1)^{\alpha_x}$, with $A_x = 176 \pm 1$ and $\alpha_x = 2.4 \pm .3$, is shown by the blue line, with the fit error indicated by the blue shaded region. We hypothesize that this collapse is due to the source of the instability, which is driven by localized microscopic polymer extension at length scales much smaller than the pore size. The resulting dissipation at the pore scale $\langle \chi \rangle_t$ depends only on the fluctuating strain rate field $\mathbf{s}'$, which has no characteristic length scale. Thus, while the grain size and permeability of different media seem to influence the absolute onset conditions, these differences seem to be captured naturally in Wi_I.

To relate this microscopic viscous dissipation to the macroscopic pressure drop and apparent viscosity, we use our previously derived power balance model (Eq. 3.10 in §3.4):

$$\frac{\langle \Delta P \rangle_t}{\Delta L} \equiv \frac{\eta_{\mathrm{app}}(Q/A)}{k} \approx \underbrace{\frac{\eta(\dot{\gamma}_I)(Q/A)}{k}}_{\text{Darcy's law}} + \underbrace{\frac{\langle \chi \rangle_{t,V}}{(Q/A)}}_{\text{Fluctuations}} + \left\{ \begin{array}{c} \text{Strain} \\ \text{history} \\ \text{effects} \end{array} \right\}. \tag{4.2}$$

Though in principle the full strain history of the advected polymer stresses contributes to the macroscopic resistance, we neglect it for simplicity, motivated by measurements in the coarse medium (§3.11). Plotting just the first two terms on the right hand side of equation 4.2 yields the grey line in Figure 1B (grey shaded region indicates error from fit of $\langle \chi \rangle_{t,V}$),

agreeing quite well with the independent pressure drop measurements in both media. At higher Wi_I the first two terms on the right hand side of equation 4.2 predict 80% of the peak resistance, the difference likely due to the neglected strain history effects; incorporation of this term is an important direction for future work. Thus, the generation of elastic turbulence—and the functional form of the resulting excess resistance with Weissenberg number—does not seem to depend on the permeability of a porous medium. We thus use this measured apparent viscosity $\eta_{\mathrm{app},i}$ as an input for to our parallel resistor model for each stratum i of a heterogeneous porous medium.

4.4 Apparent viscosity in a porous medium with two strata

We numerically solve equations 4.2 and 4.1 along with mass conservation ($Q = Q_F + Q_C$) to obtain the net pressure drop $\langle \Delta P \rangle_t$ for an imposed total flow rate Q. The net apparent viscosity for the entire stratified system can then be estimated for a range of stratified systems with different permeability ratios $\tilde{k}$, all with equal cross-sectional areas ($\tilde{A} = 1$) (Fig. 4.3A). We validate that our model depends on relative permeabilities $\tilde{k}$ and areas $\tilde{A}$, but not absolute values (§A.6). We further denote the point where the coarse and fine strata hit the critical Weissenberg number $\mathrm{Wi}_c = 2.6$ with upward and downward triangular markers respectively. Surprisingly, our model indicates that the apparent viscosity for a stratified medium does not deviate strong from the homogeneous medium expectation (here given identically by $\tilde{k} = 1$). The smooth increase in apparent viscosity closely mirrors that of the homogeneous medium, increasing permeability ratio provides only a modest shift to lower Wi_I, converging for $\tilde{k} \gtrsim 100$. In all cases the coarse layer becomes unstable first, producing an uptick in the apparent viscosity at $\mathrm{Wi}_I < 2.6$, and the fine layer reaches the instability

only at higher Wi_I, matching our experimental observations of the pore scale instability in the $\tilde{k} = 9$ sintered stratified medium (Figure 4.1 D and E).

We can validate this model prediction for apparent viscosity using pressure drop measurements in the $\tilde{k} = 9$ sintered stratified medium. At low Weissenberg numbers, the apparent viscosity again equals the shear viscosity, in agreement with Darcy's Law, but deviates sharply above a threshold Weissenberg number of $\mathrm{Wi}_c \approx 2.6$, closely following the measurements for the homogeneous porous media in agreement with our model prediction (navy blue points in figure 4.2 A), with a slight shift to lower Wi_I and the anticipated under-prediction of the peak due to our neglect of strain history effects. Thus, despite the strong heterogeneity and uneven partitioning of the flow, the apparent viscosity measured from the pressure drop follows a similar trend to that of an effective homogeneous medium, but agrees more quantitatively with the predictions of our parallel resistor model (reproduced in part for model comparison in 4.3 A and B). We see similar behavior varying the area ratio between the strata $\tilde{A} = A_C/A_F$ (maintaining a constant $\tilde{k} = 9$). As expected, this matches the homogeneous medium model for $\tilde{A} = 0$ and converges as $\tilde{A} \to \infty$ (Fig. 4.2B). For area ratios in the range $\tilde{A} \approx 0$ to 0.1, the instability onsets first in the coarse layer at progressively lower Wi_I, but again with only a minor contribution to elevated resistance until the fine layer becomes unstable.

4.5 Flow redirection in a porous medium with two strata

Our validated parallel resistor model can then reveal how this onset of the instability in the coarse layer at lower Wi_I redirects flow towards the fine layer. For a Newtonian fluid, the partitioning of the flow between strata is set by Darcy's law, and since the viscosity is a

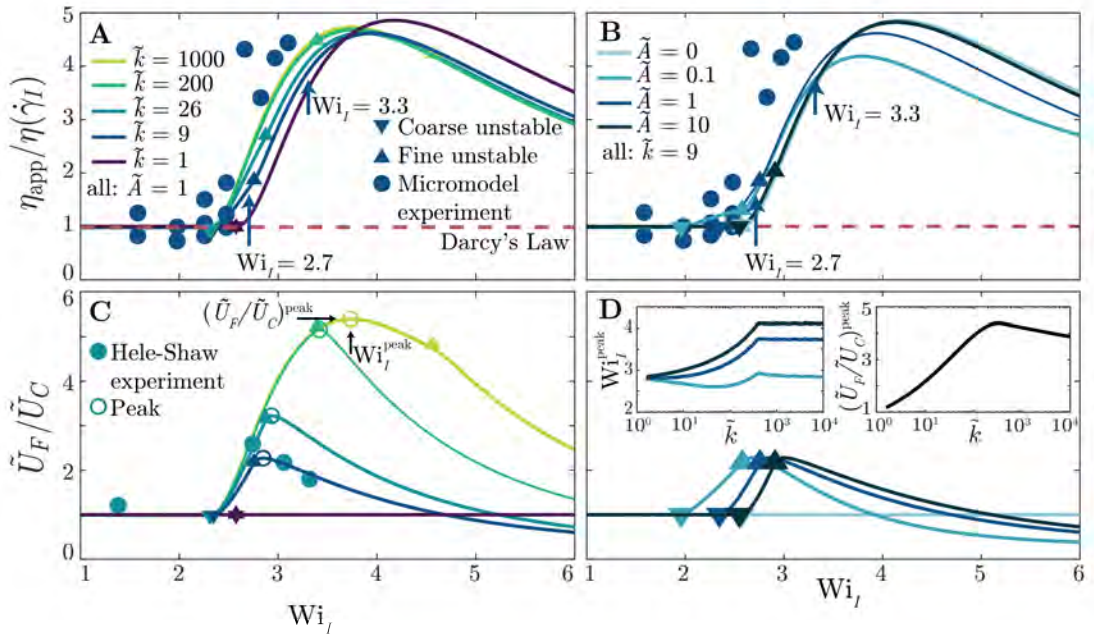

Figure 4.3: Parallel resistor model suggests that the instability redirects flow in a stratified porous media to mitigate excess resistance. **A** Parallel resistor model recapitulates modest shift to lower Wi_I for high permeability ratios, converging for $\tilde{k} \gtrsim 200$. **B** Varying area ratio displays similar modest shifts to lower Wi_I, with the strongest deviation around $\tilde{A} \approx 0.1$. **C** Parallel resistor model reveals that the apparent viscosity is insensitive to stratification because flow is redirected strongly to the low permeability layer to minimize excess resistance. **D** Adjusting the area ratios alters the position ($\mathrm{Wi}_I^{\mathrm{peak}}$) but not the magnitude ($\left(\tilde{U}_F/\tilde{U}_C\right)^{\mathrm{peak}}$) of the peak redirection (insets).

constant this yields a constant $(U_F/U_C)_{\text{Newt}} = \tilde{A}^{-1}\tilde{k}^{-1}$. For our shear thinning fluid, we can modify this expectation with $\eta\dot{\gamma}_{I,i}^{\alpha_s-1}$ in each layer i, again giving a constant partition of $(U_F/U_C)_{\text{lam}} = \tilde{A}^{-1/(1+\alpha_s)}\tilde{k}^{-(1-\alpha_s/2)/(1+\alpha_s)}$. For low Wi_I, where our polymer solution's apparent viscosity is well characterized by the shear viscosity, the computed partitioning of the flow $\tilde{U}_F/\tilde{U}_C \equiv (U_F/U_C)\,/\,(U_F/U_C)_{\text{lam}}$ matches the expected constant (Fig. 4.3C and D). Once the coarse layer becomes unstable, however, the partitioning of flow increases sharply, indicating that differential increases in the flow rate are being redirected to the fine layer. This differential redirection occurs because the differential resistance in the coarse layer now includes the excess resistance provided by elastic turbulence in the second term on the right hand side of equation 4.2, while the fine layer has the same differential resistance set by Darcy's Law alone. The much higher excess resistance in the coarse layer redirects the flow towards the fine layer, and hence contributes only minimally to adding additional resistance. When the flow in the fine layer eventually becomes unstable, the redirected flow speed peaks and declines as the flow in the fine layer now also experiences the elevated resistance. At very high Wi_I, this begins to redirect flow further into the coarse layer, though it is unclear how far our model can be extrapolated past $\text{Wi}_I > 5$. We can track the peak position ($\text{Wi}_I^{\text{peak}}$), which depends on both $\tilde{k}$ and $\tilde{A}$ (Fig. 4.3D left inset), though the height height of the peak ($\left(\tilde{U}_F/\tilde{U}_C\right)^{\text{peak}}$) does not change with $\tilde{A}$ (Fig. 4.3D right inset). Thus, though the excess resistance of polymer solutions in a stratified medium is generally well approximated by a homogeneous medium model, the partitioning of flow speed between strata depends strongly on the stratification and the onset of elastic turbulence in coarser strata. Experiments in the $\tilde{k} = 26$ unconsolidated stratified porous medium quantitatively match the predicted peak in flow redirection (teal blue points in figure 4.3 C).

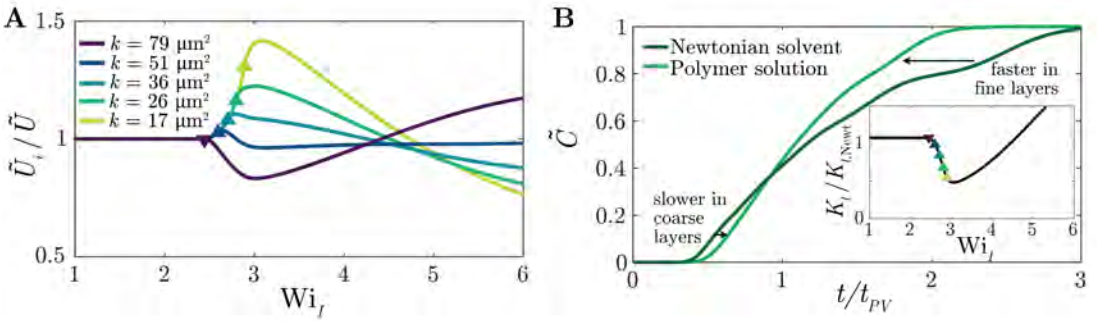

Figure 4.4: Flow homogenization in n-layered stratified media. **A** In an example 5-layer system (schematized in inset), flow is redirected to finer strata after the coarsest layer becomes unstable. Flow redirects back away from each layer when it becomes unstable. **B** Breakthrough curve in 5-layer medium for polymer solution at $\mathrm{Wi}_I = 3.2$ and Newtonian fluid at same flow rate, indicating that intermediate Wi_I can appreciably homogenize the flow. **C** Characterization of homogenization using an effective longitudinal dispersion coefficient indicates a minimum dispersion (optimal homogenization) around $\mathrm{Wi}_I \approx 3.2$, shortly after the finest layer reaches the onset of the instability.

Thus, our parallel resistor model reveals that at a range of intermediate Wi_I, elastic turbulence arises only in the coarse stratum, producing an increase in apparent viscosity only in the coarse stratum; this elevated resistance to flow redirects flow towards the fine stratum, resulting in the observed homogenization of superficial velocities and hence transport of passive scalars.

4.6 Parallel resistor model for a heterogeneous porous medium with n strata

To test if this homogenization extends more generally to multi-layered systems, we apply our parallel resistor model to a porous medium with an arbitrary number of strata. We set the pressure drop in all n strata equal (Eq. 4.1) and numerically solve these $n - 1$ equations simultaneously with a mass balance $Q = \Sigma_n Q_i$.

For an example 5-layer medium with a lognormal permeability distribution ($k = 79\ \mu m^2$, 51 μm^2, 36 μm^2, 26 μm^2),[178] the proportion of the superficial velocity in each of the finer

strata $\tilde{U}_i/\tilde{U}$ (again normalized by the laminar expectation) increases as expected after the coarsest layer becomes unstable (blue square, figure 4.4A), and peaks shortly after that layer becomes unstable as well (blue circles). Because of this redirection, the flow in the entire stratified medium can be partially homogenized at intermediate Wi_I. A theoretical breakthrough curve is generated using the velocity in a layer U_i, along with longitudinal dispersion in a homogeneous medium:[187]

$$C = 0.5\left(1 - \mathrm{erf}\left(\left(1 - \frac{t}{t_{PV}}\right) / \left(2\sqrt{\frac{K_{l,i}}{U_i L}}\sqrt{\frac{t}{t_{PV}}}\right)\right)\right). \tag{4.3}$$

The single layer longitudinal dispersion coefficient is given by $K_{l,i} = D(1/\tau + 0.5\mathrm{Pe}^{1.2})$ for Peclet numbers $\mathrm{Pe} = U_i d_{p,i}/D < 605$ and $K_{l,i} = D(1/\tau + 1.8\mathrm{Pe})$ for $\mathrm{Pe} > 605$.[188] We use typical values for tortuosity $\tau = 2$, molecular diffusion coefficient for a small molecule $D = 10^{-6}$ cm^2/s, and the grain size in each layer $d_{p,i}$ estimated from the permeability using the Kozeny-Carman relation.[185] For a Newtonian fluid, (light green line, fig. 4.4B), all strata are laminar, and the breakthrough is heterogeneous: coarser strata are infiltrated quickly in less than a pore volume, but the vanishingly small flow speeds in the finer strata take hundreds of pore volumes to infiltrate fully ($t/t_{PV} = 2.5$ for 90% of breakthrough). A polymer solution at the same flow rate ($\mathrm{Wi}_I = 3.2$, where the finest layer has just reached the onset of the instability) slightly slows infiltration of the coarsest two strata, while significantly accelerating the infiltration of the finest three strata ($t/t_{PV} = 1.8$ for 90% of breakthrough, dark blue, fig. 4.4B). This $\sim 1.4\times$ improvement can be captured by an effective dispersion coefficient $K_{l,\mathrm{eff}}$ by fitting the total breakthrough curve to a single error function,[180] which characterizes the width of the injection front, here dominated by mean flow speed differences between strata. We compare the simulated effective dispersion for

our polymer solution at different Wi_I to a Newtonian fluid at the same flow rate $K_{l,\mathrm{Newt}}$. At low Wi_I the polymer solution matches the dispersion of the Newtonian fluid, since all strata are laminar (fig. 4.4C). Once the coarsest layer becomes unstable, the effective dispersion drops relative to the Newtonian fluid, indicating a more compact injection front due to increased flow through finer strata (dark blue square, fig. 4.4C). The effective dispersion continues decreasing until the finest layer becomes unstable around $\mathrm{Wi}_I \approx 3$, curbing the redirection until the effective dispersion hits a minimum at $\mathrm{Wi}_I \approx 3.2$ and then increases, eventually exceeding the Newtonian fluid, indicating that the excess resistance in the finest strata makes the flow even more heterogeneous at these extreme Wi_I. Numerically solving on a range of different media with differing numbers of strata and permeabilities yields quantitatively different reductions in $K_{l,\mathrm{eff}}$, but generally produce a minimum in the range $\mathrm{Wi}_I \approx 2.5$ to 4 for the selected polymer rheology. Understanding the origin of this fairly insensitive minimum condition, and how the position and magnitude of the minimum is shaped by polymer solution rheology, will be important next steps for designing polymer solutions for particular reservoir flooding operations.

4.7 Conclusions

Our work provides the first characterization of elastic turbulence in stratified porous media. We demonstrate through pressure drop measurements and confocal microscopy that elastic turbulence arises in homogenous media of different grain sizes at the same Wi_I, and producing a quantitatively similar excess flow resistance $\langle \chi \rangle_{t,V}$. For a stratified medium, the uneven partitioning of flow causes the coarsest layer (highest permeability) to reach the critical onset Wi_c first. Surprisingly, however, this does not lead to an early increase in apparent

viscosity: instead, flow is redirected towards finer strata (lower permeability) to minimize the excess resistance associated with elastic turbulence in the coarsest layer. This redirection of flow towards low permeability strata significantly alters the transport of passive scalars. Dye infiltration experiments show how operating near the onset of elastic turbulence in the finest layer can greatly homogenize the flow between strata, in agreement with theoretical expectations.

While our experiments consider a single polymer solution, the generation of elastic turbulence and the magnitude of excess flow resistance $\langle \chi \rangle_{t,V}$ may vary with polymer concentration, molecular weight, and solvent composition. The relative role of strain history effects, neglected here, may also begin to play an important role for different formulations or in different regimes of Wi_I. Understanding how these differences in excess resistance alter the partitioning of flow and resulting scalar transport in stratified media remains an important direction for future work.

The reported homogenization of flow between strata in layered porous media may greatly influence the transport of passive scalars through environmental porous media, where heterogeneous flow between strata can often limit injection processes.[180] Examples include oil recovery, pump-and-treat groundwater remediation, where this homogenization may improve sweep efficiencies by providing faster infiltration of low permeability strata. Such homogenization may also provide more uniform delivery of oxidants to contaminants for in situ degradation in aquifers, or higher contact areas for heat transfer during geothermal energy extraction. A deeper understanding of elastic turbulence in stratified media can thus inform a range of energy and environmental applications.

4.8 Movie captions

The movies corresponding to data in this chapter can be found in the repository at https://github.com/cabrowne/dissertation-movies.

Movie 4.1: Scalar transport visualized with step change in dye. Polymer solution formulation B injected at $Q = 3$ mL/hr. Video shown at 2500× real time. Field of view 3 cm tall.

Movie 4.2: Scalar transport visualized with step change in dye. Pure solvent of formulation B (no polymer) injected at $Q = 35$ mL/hr. Video shown at 210× real time. Field of view 3 cm tall.

Movie 4.3: Scalar transport visualized with step change in dye. Polymer solution formulation B injected at $Q = 35$ mL/hr. Video shown at 210× real time. Field of view 3 cm tall.

Movie 4.4: Scalar transport visualized with step change in dye. Polymer solution formulation B injected at $Q = 45$ mL/hr. Video shown at 120× real time. Field of view 3 cm tall.

Movie 4.5: Streamlines of flow in stratified medium ($\tilde{k} \approx 9\,\tilde{A} \approx 1$) in 10 pores in coarse layer (top, scale bar 100 μm) and 10 pores in fine layer (bottom, scale bar 50 μm) at $\mathrm{Wi}_I = 2.7$, just below expected onset of instability in fine layer. Red line demarcates pores labeled stable or unstable by clear crossing of streamlines over time. Videos shown at 25x real time.

Movie 4.6: Streamlines of flow in stratified medium ($\tilde{k} \approx 9\,\tilde{A} \approx 1$) in 10 pores in coarse

layer (top, scale bar 100 μm) and 10 pores in fine layer (bottom, scale bar 50 μm) at $\mathrm{Wi}_I = 3.3$, above the expected onset of instability in fine layer. Red line demarcates pores labeled stable or unstable by clear crossing of streamlines over time. Videos shown at 25x real time.

Movie 4.7: Streamline of flow in an example pore in fine homogeneous medium ($k = 8.6\ \mu\mathrm{m}^2$) at $\mathrm{Wi}_I = 2.4$. The flow is stable in time, indicated by streamlines that do not change over the course of the 5 min real time video. Video is shown at 33x real time. Field of view is 157 μm.

Movie 4.8: Streamline of flow in an example pore in fine homogeneous medium ($k = 8.6\ \mu\mathrm{m}^2$) at $\mathrm{Wi}_I = 3.6$. The flow is stable in time, indicated by streamlines that do not change over the course of the 5 min real time video. Video is shown at 6x real time. Field of view is 157 μm.

Nothing makes me so happy as to observe nature and to paint what I see.

Le Douanier Henri Rousseau

5

Outlook and future directions

We have now seen how polymer solutions can produce elastic instabilities in 3D, disordered porous media. In the successive expansions and contractions of a porous medium, retention of polymer memory produce a surprising bistability in the stationary pore-scale flow state. In 3D disordered media, we demonstrate that elastic turbulence does arise, despite previous suggestions that the inherent disorder may suppress the instability.[15] However,

this disorder produces a distribution of pore-scale onset conditions Wi_c, allowing unstable and laminar pores coexist. By adapting approaches from the inertial turbulence literature, we showed that the pore-scale viscous dissipation caused by chaotic fluctuations directly leads to the anomalous increase in flow resistance, resolving an over-50-year-old puzzle.[12] We then demonstrated that the onset of this instability and concomitant rise in flow resistance is general across porous media of different grain sizes. Finally, we demonstrated how understanding and modeling this flow resistance can be leveraged to control and direct the flow in new ways. In particular, we demonstrated that elastic turbulence arises in individual layers of a stratified porous medium, representative of many key environmental applications; our modeling efforts allow us to design flow conditions where excess resistance in high permeability strata can redirect flow to lower permeability strata, homogenizing transport of solutes or heat.

Overall, the results of this dissertation suggest the tantalizing possibility that many modeling techniques developed for inertial turbulence can be stolen and adapted for elastic turbulence. These modeling approaches may thus provide new avenues to achieve similar enhancements in momentum, mass, and heat transport in applications where turbulence is inaccessible ($\mathrm{Re} \ll 1$), like flows in environmental porous media, packed bed reactors, chromatography columns, and microfluidics. As a final note, I outline here the current work I have been involved in to begin answering two remaining open questions. First, how are these findings generalized to polymer solutions of different concentrations? Second, how do these chaotic fluctuations translate to enhanced solute mixing?

5.1 Generalization across polymer solution formulations

The polymer formulations used in this dissertation serve as excellent test fluids, with elevated solvent viscosity to reduce shear-thinning and refractive-index matching to render our model 3D porous media transparent for imaging. However, in many applications these solvents or polymers may be incompatible—e.g. in groundwater aquifers, the solvent should be pure freshwater. Thus, to provide more general models for to allow for design of polymer solutions for specific engineering applications, we are currently working to generalize our models across a range of polymer solutions. Thus far, we have tested the role of polymer concentration , suggesting that the concentration relative to overlap C/C^* is one key parameter that affects excess flow resistance.

We formulate 6 polymer solutions using the same solvent as our formulation B (§A.1), but with varying concentrations of 18 MDa HPAM. Figure 5.1 shows the shear rheology for 300, 400, 600, 1000, and 2000 ppm solutions. Two solutions prepared at 50 and 150 ppm did not exhibit a significant enough elastic stress N_1 to warrant detailed testing. We inject the polymer solutions into the same coarse medium used in chapter 3, cleaning the medium between solutions using flushes of IPA and ultrapure milliQ water. We impose a constant flow rate using Harvard Apparatus pumps (§A.4), and measure the pressure drop across the medium after the pressure signal has fully equilibrated (typically $\gtrsim$ 1 hr). We

The work presented in this subsection is based on unpublished work by Christopher A. Browne, Richard B. Huang, and Sujit S. Datta. **Author Contributions:** R.B.H. conducted all experiments on solution generality. C.A.B, R.B.H., and S.S.D. designed the experiments, analyzed the data, and discussed the results. S.S.D. designed and supervised the overall projects.

then report the time averaged pressure drop as a relative apparent viscosity:

$$\frac{\eta_{\text{app}}}{\eta(\dot{\gamma})} = \frac{k}{\eta(\dot{\gamma})}\frac{A}{Q}\frac{\langle \Delta P \rangle_t}{\Delta L}. \tag{5.1}$$

Vertical error bars represent the combined propagated error of the standard deviation of ΔP in time and the error in our shear viscosity measurements. Horizontal error bars represent the combined propagated error of our first normal stress difference and shear stress measurements.

Figure 5.2 shows that all solutions exhibit an increase in apparent viscosity from the Darcy's law expectation above a threshold $\text{Wi}_c \approx 2$ to 3. For low concentrations $c = 300$ and 400 ppm, this rise in apparent viscosity seems to follow a similar rise, peaking around $\approx$ 6 to 7$\times$ the Darcy's law expectation. However, for higher concentrations $c = 600$, 1000, and 2000 ppm, the growth is delayed, reaching the same $\approx$ 6 to 7$\times$ rise only at much higher $\text{Wi}_I \approx 4$ to 7. Intriguingly, this deviation seems to begin at roughly the overlap concentration of our formulation B polymer solution $c^* \approx 600$, suggesting that this change in resistance may be caused by the transition from a dilute to semi-dilute solution.

To further explore what causes this softening of the rise in excess resistance, we directly image the flow of the 2000 ppm solution using confocal microscopy. Above $\text{Wi}_I \approx 3$, we again see the onset of an elastic instability characterized by sustained streamline crossing. In many pores, however, we see the surprising formation of dead zones, where the flow is extremely slow moving and thus lacks strong fluctuations. Similar dead zones have been observed in 2D pillar arrays when the polymer concentration is semi-dilute,[109,111] further suggesting a transition at $C \sim C^*$. These dead zones are thought to arise because of shear-banding, which is known to arise in semi-dilute polymer solutions.[189–191] We hypothesize

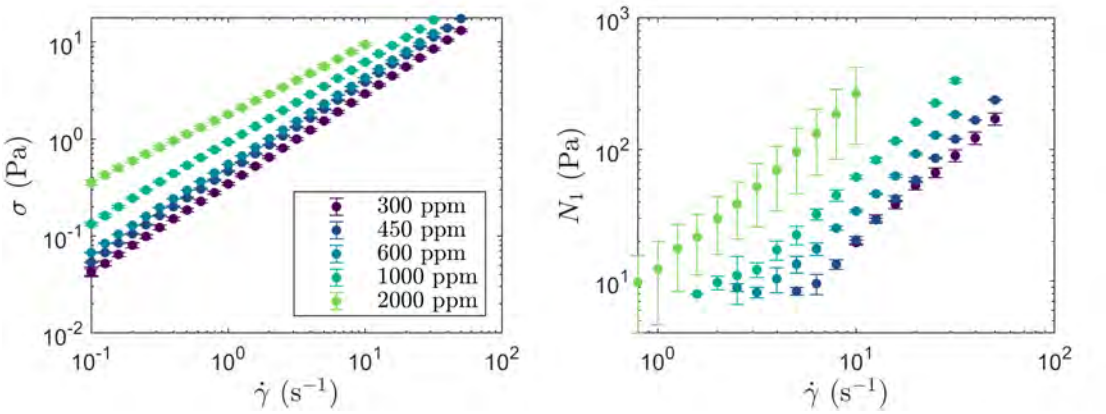

Figure 5.1: Shear stress and first normal stress difference for concentration series of formulation B.

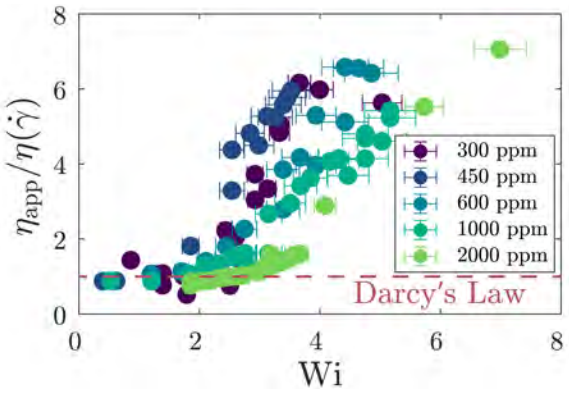

Figure 5.2: Apparent viscosity of various HPAM concentrations in solvent formulation B. Low concentrations seems to follow same rise in apparent viscosity, while higher concentrations $C \gtrsim 600$ ppm $\approx C^*$ show a softened rise in apparent viscosity, only reaching the same magnitude at higher Wi_I.

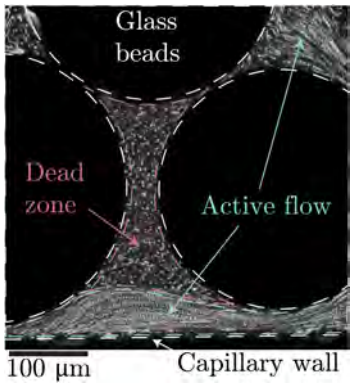

Figure 5.3: Streamline micrographs of dead zones formed by shear-banding. Formulation B with 2000 ppm HPAM at $\mathrm{W}i_I = 5.7$ exhibits regions of low flow in many pores.

that these dead zones effectively reduce the volume of the pore space that is "actively" experiencing chaotic fluctuations. The growth in excess resistance may then be estimated with an effective prefactor $\alpha\langle\chi\rangle_{t,V^*}/(Q/A)^2$, where V^* represents and average of χ over the active volume, and $\alpha \equiv V^*/V$ gives the effective reduction in active pore space. Our ongoing work is testing this hypothesis quantitatively using techniques developed in chapter 3.

Future work will further explore how the onset, spatiotemporal structure, and excess flow resistance of elastic turbulence are altered in solutions of different solvent composition, salinity, and polymer chemistry, architecture, and molecular weight.

5.2 Enhanced mixing in 3D porous media

Flow chemistry is critically important in diverse applications, ranging from the production of pharmaceuticals,[192–194] specialty chemicals,[195–197] biofuels,[198] and functional nanomaterials,[199] to sustainability and waste treatment processes,[32,200–213] separations,[192–194] electrochemistry,[214] and "green" chemistry.[198,215–217] These applications typically involve the flow of fluids containing reactants through confining spaces: e.g., smooth-walled microfluidic reactors[195,218,219] or porous media, such as packed beds,[195,200–203] chromatography columns,[192–194] and catalyst supports.[196,197] Reactive flows in porous media also arise in many biogeochemical and biomedical processes.[32,204–213] In all these cases, the typical confining length scales $L \sim 0.1$ to 100 μm are much larger than the $\sim$ nm molecular scales necessary to alter intrinsic chemical kinetics,[220–222] and the reactants act as passive scalars in the flow—the dynamics of chemical reactions are therefore controlled by the coupling between fluid flow, reactant advection and diffusion, and intrinsic reaction kinetics.

Moreover, the underlying flows are typically laminar: the Newtonian fluids used have dynamic shear viscosities $\eta \sim 1$ to 100 mPa-s and density $\rho \sim 1\,\mathrm{g/cm^3}$, and move with flow speeds $U \sim 0.01$ to 100 μm/s, yielding low Reynolds numbers $\mathrm{Re} \equiv \rho UL/\eta \sim 10^{-7}$ to 10. As a result, reaction rates are *diffusion-limited*, which for typical small molecule diffusivities $D \sim 10^{-7}$ to 10^{-5} $\mathrm{cm^2/s}$ can give reaction completion times as large as several days. Approaches to overcoming this limitation have been suggested for microfluidic re-

The work presented in this subsection is based on unpublished work by Christopher A. Browne, Reinier van Buel, Holger Stark, and Sujit S. Datta. **Author Contributions:** C.A.B. conducted all experiments. C.A.B, and S.S.D. designed the experiments, analyzed the data, and discussed the results. C.A.B., R.v.B., H.S., and S.S.D. developed the theory and wrote the text. S.S.D. designed and supervised the overall project.

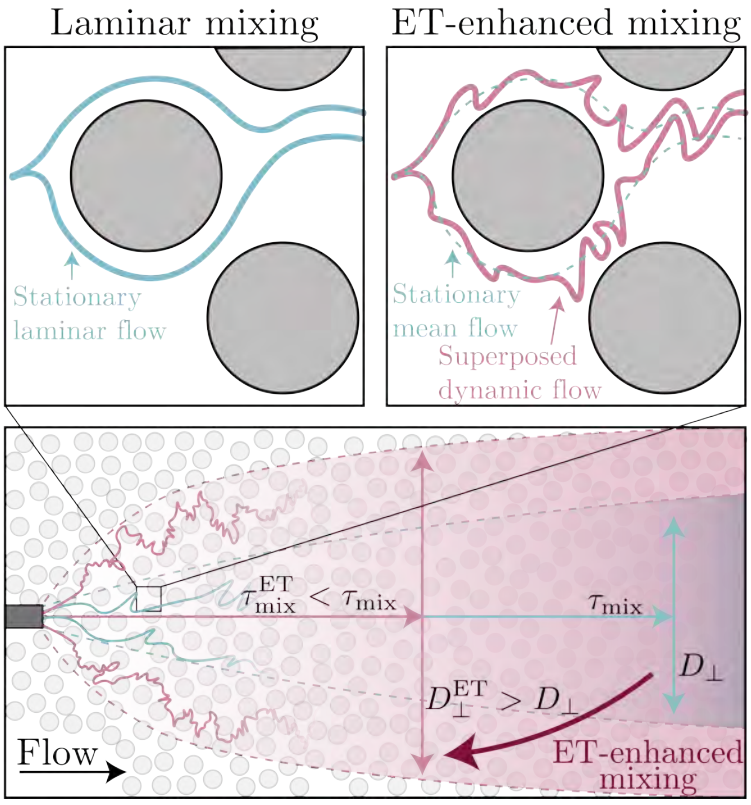

Figure 5.4: Schematic of ET-enhanced mixing in a porous reactor. For laminar flows, geometric disorder can provide some mixing of the reactant-containing fluid at large scales (blue lines). We hypothesize that *elastic turbulence* (ET) further generates chaotic mixing at the sub-pore scale (red lines), thereby reducing mixing time τ_{mix} and increasing dispersion $D_\perp$ of the reactants, thereby speeding reaction kinetics and increasing yield.

actors e.g., by performing reactions in "segmented flow" using droplets or in complex microfluidic geometries that drive small-scale fluid mixing.[223–228] However, while successful in some cases, these approaches often have limited applicability because they (i) require an additional decantation step after reaction to remove the reactive droplet phase from the immiscible carrier phase; and (ii) require a carefully controlled flow geometry, and hence are incompatible with many applications where the flow geometry cannot be controlled, e.g. in packed-bed reactors,[195,200–203] chromatography columns,[192–194] catalyst supports,[196,197] and environmental porous media.[32,204–214] Therefore, a new method of improving the speed of chemical reactions in confined geometries would be of direct importance to a variety of environmental, industrial, and medical applications.

As we have seen in the previous chapters, high molecular weight polymer additives can give rise to fascinating flow instabilities.[13,76,77,155,156,229] These chaotic flow fluctuations cause nearby fluid elements to continually separate from each other as they are advected. Thus, despite the negligible influence of inertial forces, the flow exhibits many similarities to conventional inertial turbulence observed in Newtonian fluids at high $\mathrm{Re} \gg 1$.

For unconfined flows at high $\mathrm{Re} \gg 1$, it is well-known that inertial turbulence can strongly enhance fluid mixing and thereby speed up chemical reactions.[230–232] In this case, the chaotic flow field advects nearby fluid elements away from each other, with a separation that grows exponentially in time at a rate γ typically given by the largest finite-time Lyapunov exponent (FTLE).[233–236] Often, (fluid) momentum diffusion is more rapid than (scalar) mass diffusion, as quantified by the Schmidt number $\mathrm{Sc} \equiv \eta/(\rho D) > 1$, giving the so-called "Batchelor regime". Indeed, for the ET flows we consider in this proposal, $\mathrm{Sc} \sim 10^3$ to 10^7. In this case, solute mixing is mediated by successive stretching and folding

of fluid lamellae, analogous to the process of kneading dough,[237] eventually resulting in a smallest lamellae width set by the competition between mass diffusion and fluid stretching, known as the Batchelor scale $\ell_B \sim \sqrt{D/\gamma}$—leading to established scalings for the solute concentration distribution that can be used to predict reaction kinetics in flows with chemical reactants.[223]

For elastic turbulence at low $\mathrm{Re} \ll 1$ and high $\mathrm{Wi} > \mathrm{Wi}_c$, the chaotic flow is thought to similarly lead to enhancements in solute mixing, as described by numerical simulations.[131,238,239] Experiments in weakly-confined geometries have confirmed this expectation, demonstrating that in many cases, the predictions of Batchelor mixing apply—in this case, with the FTLE γ set by a characteristic polymer relaxation time λ.[152,240–246] Thus, elastic turbulence has been explored for enhanced heat and mass transport in diverse contexts.[148,152,154,162,164,238,239,246–257] However, it remains unexplored how this enhancement in mixing couples with the natural mixing induced by a disordered 3D porous medium.

Even for laminar flows, when they are in porous media composed of disordered granular packings, the structural heterogeneity of the pore space can also give rise to chaotic Batchelor mixing over large multi-pore length scales.[258–268] In particular, the steady, laminar flow past different grains successively stretches and folds fluid lamellae (blue lines in Fig. 5.4)—in this case, with the large-scale FTLE γ set by the inverse of the pore-scale advection time $\approx d/U$, where d and U are the characteristic grain diameter and flow speed, respectively. Thus, this heterogeneity-induced deformation of fluid elements can enhance mixing compared to flows in more uniform channels. Nevertheless, when used for flow chemistry, this approach is still inherently limited by slow diffusion of reactants at the pore scale. We conjecture that elastic turbulence can overcome the limitations of laminarity to promote

mixing at the pore scale as well.

5.2.1 Preliminary results

As a first step to test this idea, we have directly visualized solute mixing in the presence of elastic turbulence. We fabricate a coarse 3D porous medium following our earlier protocol (§A.4), except in a rectangular quartz capillary $A \approx 4\text{ mm} \times 2\text{ mm}$. We then glue in two 14 gauge needles ($\approx$ 2mm outer diameter) to introduce co-flowing streams. We introduce identical solutions (either polymer solution formulation B §A.1.1 or the corresponding pure solvent), one stream with a fluorescent dye (solute) and one without (solute-free), as schematized in Fig. 5.5B. We use initial dye concentrations of $c_0 = 200$ to 500 ppb of rhodamine red-X (Succinimidyl Ester, 5-isomer *Thermo Fischer*). As a calibration, we use constant confocal settings (laser power 14, gain 45, offset 0, images collected in a similar capillary setup and imaging depth as porous medium experiments with the same 4x objective, pixel size, frame rate, and frame size) on a concentration dilution series of this dye, we observe that the collected laser intensity (ranging from 0 to 4095 as a 16-bit image) scales linearly with dye concentration, allowing us to convert local fluorescent intensity I directly with local concentration c (notably the fluorescence intensity is a strong function of solvent, as shown by the same measurement for rhodamine red in water—green line Fig. 5.5C). Using the fully-mixed concentration $0.5c_0$, we define a normalized concentration $\tilde{c} \equiv c/(0.5c_0 - 1)$ which is $\tilde{c} = 1$ in the dyed stream, $\tilde{c} = -1$ in the un-dyed stream, and tends to $\tilde{c} \to 0$ for complete mixing. All further measurements are reported in terms of $\tilde{c}$.

We then image the pore space using confocal microscopy to characterize the spreading of the solute plume over space and time, at different length scales. We image at a plane $\sim$ 200

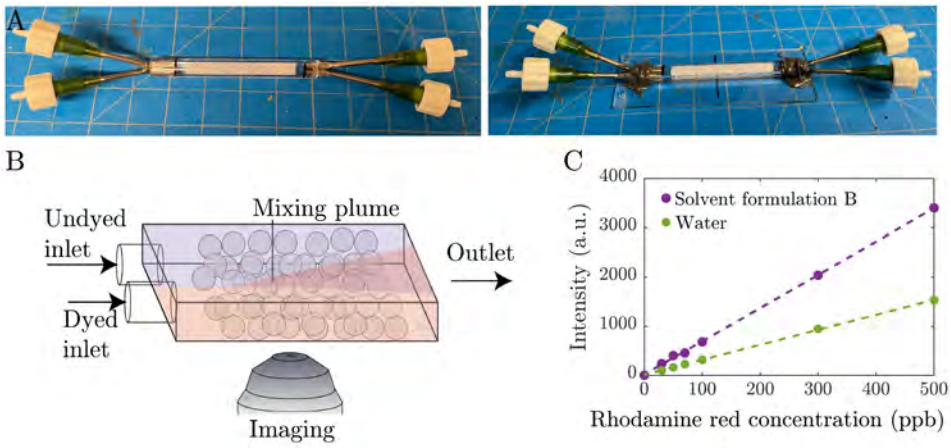

Figure 5.5: Setup to test the role of elastic turbulence on solute mixing. A photographs of capillary setup. After a small amount of 5 min epoxy is used to hold the needles in place, 24 hour marine weld is used to create a water-tight seal. **B** Schematic of dye plumes to be tracked by confocal microscopy. **C** Empirical relation of measured fluorescence intensity to rhodamine red concentration taken at the same laser and collection settings as all experiments in this section.

μm above the bottom capillary wall using the a 4x objective, galvano scanner at 1024×1024 pixels, 3.09 μm/pixel, and 0.5 fps for intervals of 3 min. We image sequentially down the length of the medium, with 90% frame overlap and stitch the images by averaging pixels in the overlapping area (Fig. 5.6A). Over the length of the medium, the initially distinct streams (black $\tilde{c} = -1$ and yellow $\tilde{c} = 1$) mix to produce an intermediate concentration (blue to green $\tilde{c} \approx 0$). Looking at an individual frame $\sim 1/3$ of the length from the inlet, we can see the pore-scale dynamics of mixing (Fig. 5.6B and C). At a low $\mathrm{Wi}_I = 1.9$ the flow is laminar, and mixing occurs by dispersion within the disordered medium, characterized by large lamellae of high dye concentration formed by fluid folding (white ellipses). At a higher $\mathrm{Wi}_I = 4.4$, above the onset of elastic turbulence, the pore-scale lamellae appear more blurred (white ellipses), and some pores near the interface are clearly closer to the fully mixed (compare shift from yellow to green-blue in pores with red ellipses). A clue to the origin of these two effects is revealed by the standard deviation of dye concentration

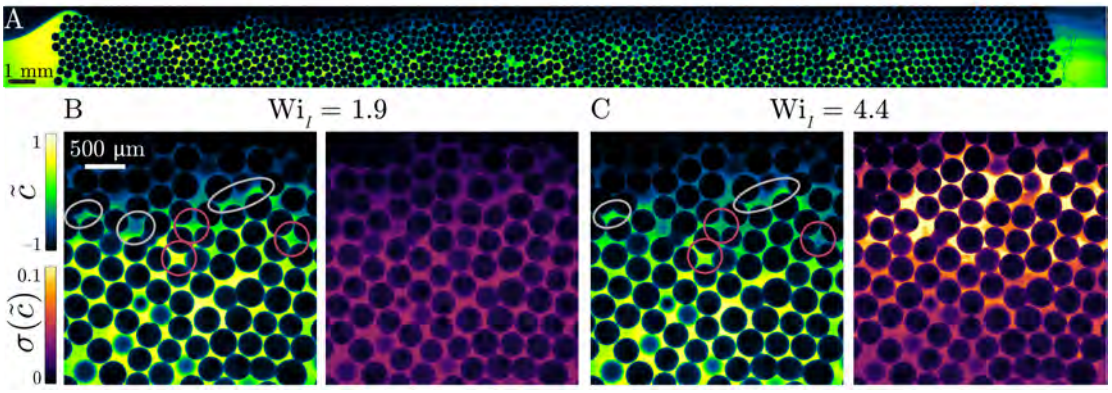

Figure 5.6: Macro-scale imaging tracks mixing in a 3D porous medium. **A** Stitched images show mixing of two initially distinct dye concentrations (black-navy $\tilde{c} = -1$ and white-yellow $\tilde{c} = 1$) to an intermediate $\tilde{c} \approx 0$ (blue-green). Time-averaged concentration $\langle \tilde{c} \rangle_t$ below ($\mathrm{Wi}_I = 1.9$ in **B**) and above ($\mathrm{Wi}_I = 4.4$ in **C**) the onset of elastic turbulence show how some pores are better mixed (red ellipses). Standard deviation of concentration $\sigma(\tilde{c})$ reveals strong temporal fluctuations in dye concentration above the onset of elastic turbulence.

over the course of the 3 min video: the flow exhibits must stronger local fluctuations in dye concentration at the higher $\mathrm{Wi}_I = 4.4$ (more yellow-white in fig. 5.6C than in B).

Consistent with the Batchelor picture of chaotic mixing, our pore-scale imaging at high time resolution (30 fps on resonant scanner) also revealed that this enhanced mixing is generated by the successive folding of solute lamellae into the bulk solute-free fluid, mediated by elastic turbulence (Fig. 5.7A). Kymographs show how flow fluctuations drive the folding of dye lamellae in time (Fig. 5.7B–C). The temporal power spectrum of these fluctuations exhibits a power law decay, indicating that a broad spectrum of chaotic dye concentration fluctuations (Fig. 5.7D). Similarly, the spatial power spectrum of these pore-scale fluctuations reproduces the predicted Batchelor scaling (Fig. 5.7E),[269] and the distribution of dye within the pore over time follows a gamma distribution, as expected in Batchelor mixing (Fig. 5.7F).[258]

These results suggest the tantalizing possibility that the pore-scale mixing induced by

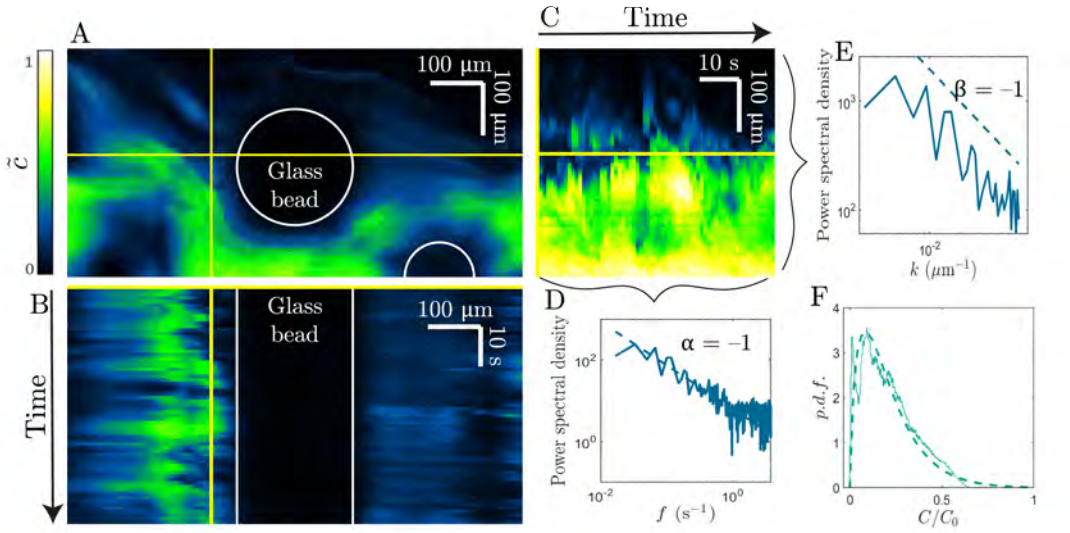

Figure 5.7: Elastic turbulence drives chaotic concentration fluctuations at pore-scale, consistent with Batchelor picture of mixing. A Instantaneous image of dye concentration for $\mathrm{Wi}_I = 4.4$ at pore-scale taken at 30 fps on resonant scanner. **B–C** Elastic turbulence drives fluctuations in dye concentration in both space and time. **D** A broad spectrum of observed concentrations over time indicate that the fluctuations are chaotic. **E** Power-law scaling for spatial spectrum in concentration reproduces expected Batchelor scaling of $\beta = -1$. **F** distribution of concentrations over space and time consistent with a gamma distribution, as expected for Batchelor-regime mixing.

elastic turbulence in a porous medium can be understood using the same formalism used in traditional inertial turbulence. Future work is needed to understand how this pore-scale mixing translates to macroscopic mixing, and how this couples with the natural dispersive mixing of a porous medium. We hypothesize that the effects of large-scale mixing in porous media due to structural disorder and the effects of pore-scale mixing due to ET will operate jointly—as schematized by the red lines in Fig. 5.4—thereby improving the overall efficiency of scalar mixing and reactive flows in porous media.

A

Materials and Methods

This appendix describes in more details on the solution formulations, experimental setups, and computational processing details helpful for replication and extension of this work.

A.1 Polymer solutions

We use two different polymer solution formulations throughout this dissertation. For experiments in the SLA printed channels (chapter 2), we use **formulation A** following previous work.[14,85,97,154] For experiments in our 3D porous media setup (chapters 3, 4, and 5), we use **formulation B**, which we have tuned to precisely match the refractive index of glass beads $n \approx 1.4786$. All solutions are used within two months of preparation. All solutions are prepared by dissolving $M_w = 18$ MDa hydrolyzed polyacrylamide (HPAM; 30% carboxylated monomers, *Polysciences*) in ultrapure *milliPore* water and then diluting with other solvents (glycerol, DMSO) and solutes (NaCl, fluorescent dyes, fluorescent tracer particles).

Formulation A is comprised of a 300 ppm solution of $M_w = 18$ MDa HPAM and 1 wt.% NaCl (*Sigma Aldrich*) dissolved in 10 wt.% ultrapure *milliPore* water, and 89 wt.% glycerol (*Sigma Aldrich*).

Formulation B is comprised of 300 ppm solution of $M_w = 18$ MDa HPAM and 1% NaCl (*Sigma Aldrich*) dissolved in 6 wt.% ultrapure *milliPore* water, 82.6 wt.% glycerol (*Sigma Aldrich*) and 10.4 wt.% dimethyl sulfoxide (DMSO; *Sigma Aldrich*) to obtain a solution whose refractive index is precisely matched to that of the glass beads $n = 1.479 \approx 1.4786$

A.1.1 Rheology and characterization

We characterize all flow properties using shear rheology measurements of a 1 mL sample of the polymer solution. We use a cone-plate geometry in an *Anton Paar* MCR301 rheometer, using a 1° 5 cm diameter cone set at a 50 μm gap. We measure the shear stress σ and first

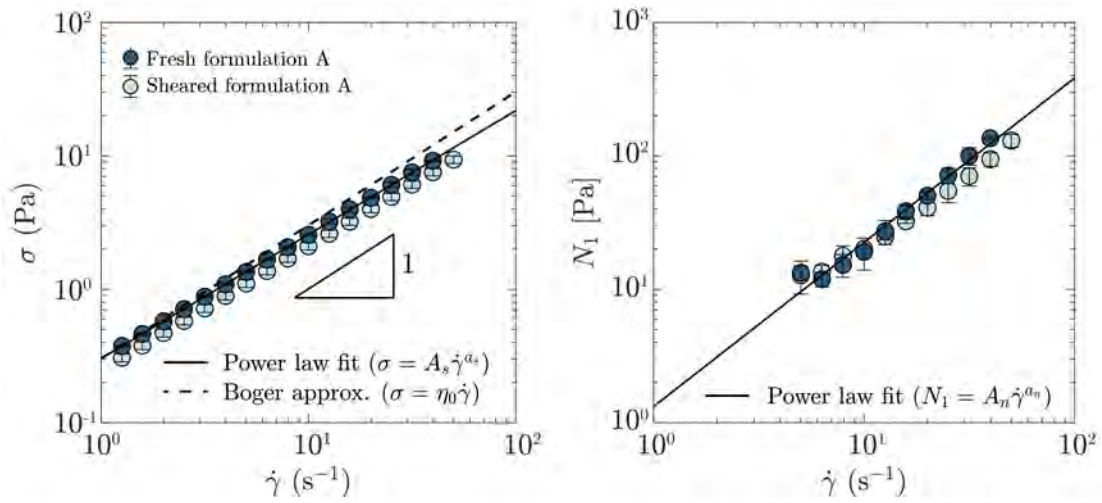

Figure A.1: Bulk rheology measurements of the shear stress and first normal stress difference as a function of shear rate for the polymer solution formulation B used in chapter 2. Data are taken before (dark blue) and after (light blue) a porous media flow experiment (at the highest tested flow rate $Q = 5$ mL/hr), showing that polymers are not appreciably degraded by the unstable flow[270]. Error bars represent standard deviation over five replicate rheological measurements. Fresh polymer solutions are prepared for each experiment, and all dimensionless quantities described in the text are calculated using rheology on fresh samples.

normal stress difference N_1 over a range of shear rates $\dot{\gamma} = 0.1\ \text{s}^{-1}$ to $100\ \text{s}^{-1}$, which spans the range of wall shear rates $\dot{\gamma}_w$ encountered in our SLA printed channels and the range of characteristic interstitial shear rates $\dot{\gamma}_I$ encountered during the flow experiments in porous media (Figures A.1 and A.2). To assess reproducibility, we collect data from at least four different samples, and find identical results for all four samples (standard deviation shown by error bars). Both the shear stress and first normal stress difference vary with shear rate according to power laws $\sigma(\dot{\gamma}) \approx A_s(\dot{\gamma})^{\alpha_s}$ and $N_1(\dot{\gamma}) \approx A_n(\dot{\gamma})^{\alpha_n}$, where σ and N_1 have units of Pa and $\dot{\gamma}$ has units of s^{-1} (Table A.1). The shear stress varies approximately linearly with shear rate in both cases, indicating that shear thinning effects are small due to the high viscosity of the background solvent ($\beta = \eta_s/\eta_0 = 0.6$ for formulation A and 0.5 for formulation B).

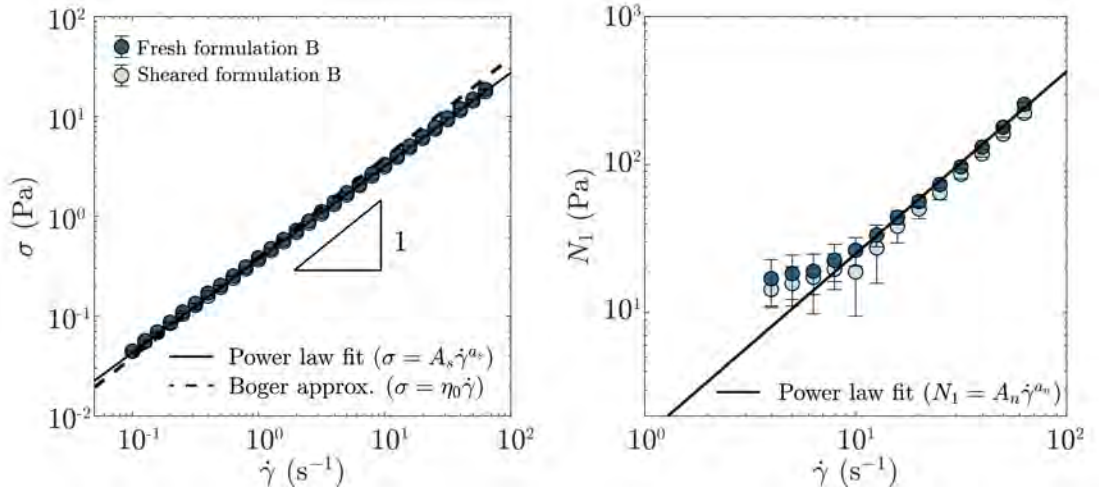

Figure A.2: Bulk rheology measurements of the shear stress and first normal stress difference as a function of shear rate for the polymer solution formulation B used in chapter 3. Data are taken before (dark blue) and after (light blue) a porous media flow experiment (at the highest tested flow rate $Q = 5$ mL/hr), showing that polymers are not appreciably degraded by the unstable flow[270]. Error bars represent standard deviation over four replicate rheological measurements. A power law fit for shear stress $\sigma(\dot{\gamma}) \approx A_s(\dot{\gamma})^{\alpha_s}$ gives $A_s \approx 0.369(8)$ Pa $\cdot$ s$^{1+\alpha_s}$, $\alpha_s \approx 0.934(7) \pm 0.001$. A power law fit for the first normal stress difference $N_1(\dot{\gamma}) \approx A_n(\dot{\gamma})^{\alpha_n}$ gives $A_n \approx 1.46(3)$ Pa $\cdot$ s$^{1+\alpha_n}$, $\alpha_n \approx 1.23(1) \pm 0.04$.

Quantity	Formulation A (Ch. 2)	Formulation B (Ch.3)	Formulation B (Ch.4&5)
A_s	0.310 ± 0.002 Pa $\cdot$ s$^{\alpha_s}$	0.369 Pa $\cdot$ s$^{\alpha_s}$	0.3428 ± 0.0002 Pa $\cdot$ s$^{\alpha_s}$
α_s	0.922 ± 0.004	0.934 ± 0.001	0.931 ± 0.001
A_n	0.85 ± 0.24 Pa $\cdot$ s$^{\alpha_n}$	1.46 Pa $\cdot$ s$^{\alpha_n}$	1.16 ± 0.03 Pa $\cdot$ s$^{\alpha_n}$
α_n	1.38 ± 0.09	1.23 ± 0.04	1.25 ± 0.02
η_0	0.319 Pa $\cdot$ s	0.419 Pa $\cdot$ s	0.419 Pa $\cdot$ s
η_s	0.197 Pa $\cdot$ s	0.230 Pa $\cdot$ s	0.230 Pa $\cdot$ s
$\beta = \eta_s/\eta_0$	0.6	0.5	0.5

Table A.1: Rheology fit parameters to power-law stress relationships $\sigma(\dot{\gamma}) \approx A_s(\dot{\gamma})^{\alpha_s}$ and $N_1(\dot{\gamma}) \approx A_n(\dot{\gamma})^{\alpha_n}$. Zero shear viscosity defined using the lowest tested wall shear rate ($\dot{\gamma}_w$ Ch.2) or interstitial shear rate ($\dot{\gamma}_I$ otherwise).

To assess possible degradation of polymers due to unstable flow in the porous media,[270] we also characterize the rheology of the same polymer solution before and after performing flow experiments at the highest flow rate tested, $Q = 5$ mL/hr. We do not find observable variation in the shear rheology (light blue symbols Figs. A.1 and A.2), indicating that polymer degradation due to the unstable flow is minimal.

We use shear rheology of the diluted polymer solution formulation B to characterize molecular properties. In particular, shear rheology measurements of a dilution series at different polymer concentrations c (Fig. A.4) yield the pure solvent viscosity $\eta_s = 0.226 \pm 0.009$ Pa · s and the intrinsic viscosity $[\eta] = (3 \pm 1) \times 10^{-4}$ ppm^{-1}. This quantity directly yields an estimate of the polymer overlap concentration c^* as established previously:[271] $c^* \approx 0.77/[\eta] = 600 \pm 300$ ppm, and therefore, our experiments use a dilute polymer solution at ≈ 0.5 times the overlap concentration. We also use this quantity to estimate the mean polymer radius of gyration R_g using the relation $c^* \approx (M_w/V)/N_A$, where M_w is the polymer molecular weight, $V = 4\pi R_g^3/3$ is the volume occupied by a single polymer molecule, and N_A is Avogadro's number,[272] yielding $R_g \approx 220$ nm. We independently verify this estimate using dynamic light scattering (DLS) of a dilute 10 ppm HPAM solution in the same index-matched solvent used in the flow experiments; we measure a mean hydrodynamic radius R_h ranging from 40 to 320 nm, which corresponds to $R_g \approx 160$ to 210 nm using the shape factor $\rho \equiv R_g/R_h \approx 1.3$ to 1.7 established previously.[273]

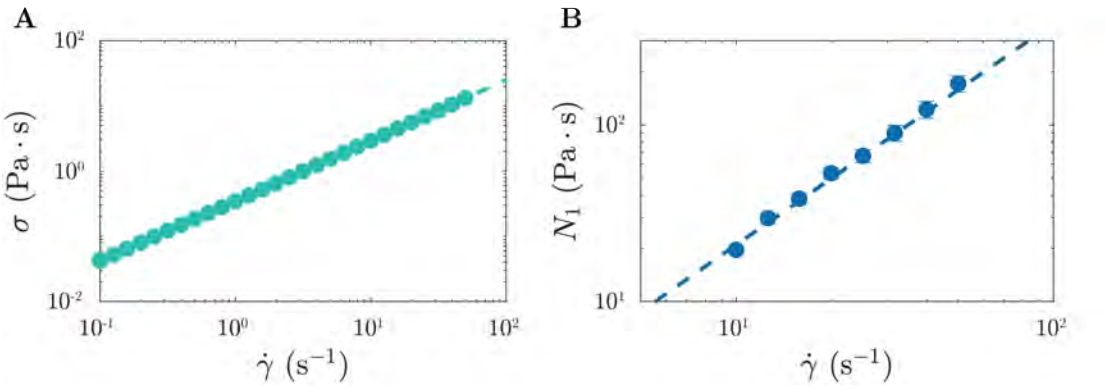

Figure A.3: Bulk rheology measurements of the shear stress and first normal stress difference as a function of shear rate for the polymer solution used in chapters 4 and 5. Error bars represent standard deviation over four replicate rheological measurements. A power law fit for shear stress $\sigma(\dot{\gamma}) \approx A_s(\dot{\gamma})^{\alpha_s}$ gives $A_s = 0.3428 \pm 0.0002$ Pa · s$^{\alpha_s}$ with $\alpha_s = 0.931 \pm 0.001$. A power law fit for the first normal stress difference $N_1(\dot{\gamma}) \approx A_n(\dot{\gamma})^{\alpha_n}$ gives $A_n = 1.16 \pm 0.03$ Pa · s$^{\alpha_n}$ with $\alpha_n = 1.25 \pm 0.02$.

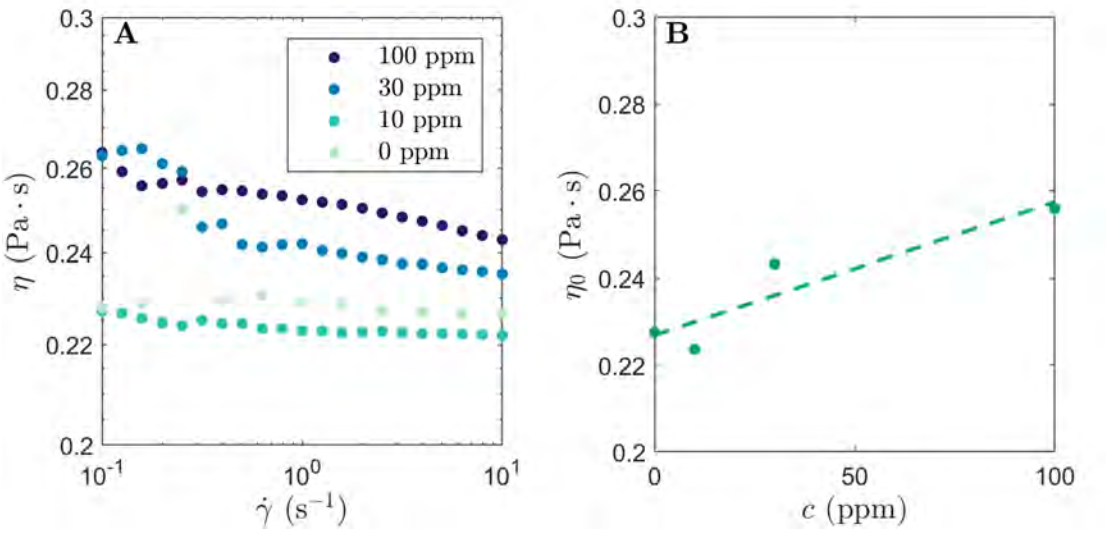

Figure A.4: Bulk rheology measurement of the solution intrinsic viscosity. A Shear viscosity measurements of polymer solution diluted with pure solvent. **B** Fit of the measured zero-shear viscosity η_0 with concentration c gives $\eta_0/\eta_s = 1 + [\eta]c$ where the pure solvent viscosity is $\eta_s = 0.226 \pm 0.009$ Pa · s and the intrinsic viscosity is $[\eta] = (3 \pm 1) \times 10^{-4}$ ppm^{-1}.

A.2 SLA printed channel fabrication

To fabricate each device used in chapter 2, we 3D-print the open-faced channel with a FormLabs Form 2 stereolithography printer, using a proprietary clear polymeric resin (FLGPCL04) composed of methacrylate oligomers and photoinitiators. We then glue inlet and outlet tubing directly into 3D-printed connectors designed to minimize perturbation of the polymers away from the pores. Finally, as shown in figure 3.1, the whole assembly is screwed shut using a clear acrylic sheet laser-cut to size and placed on top of a thin strip of polydimethylsiloxane (PDMS), which provides a water-tight seal.

A.2.1 SLA printed channel flow control

The polymer solution is injected through the porous medium at a fixed volumetric flow rate Q using a syringe pump (Harvard Apparatus PHD 2000). The time required to inject a single pore throat volume is then given by $\tau_{pv} \equiv V_{pv}/Q$, where we define the pore throat volume as the void volume between the beginning and end of a pair of opposing hemi-cylinders, $V_{pv} = D_p WH - \pi D_p^2 H/4$. In our experiments at sufficiently large Q, we find that unstable fluctuations begin after $\approx 10\tau_{pv}$ and continue to develop over a time scale of $\approx 40\tau_{pv}$, after which it reaches a dynamic equilibrium in which the statistical properties of the flow in chapter 2 do not appreciably change. Our flow visualization measurements are thus taken $\approx 300\tau_{pv}$ after initiating the flow to ensure that the unstable state is fully developed.

A.2.2 SLA printed channel imaging

To visualize the flow, we invert and mount each assembled device on a Nikon A1R inverted laser-scanning confocal microscope. For imaging, we use a green laser with an excitation wavelength of 488 nm and detection in the range 500 to 550 nm, which enables us to identify the individual fluorescent particles. We employ resonant scanning, in which the laser is raster scanned over each pixel sequentially, with a CFI60 Plan Apochromat Lambda 4x objective lens with 0.2 numerical aperture. This setup enables us to continually raster a field of view of 2127 μm by 2127 μm. We acquire fluorescence images every 33 ms (30 frames per second), from an optical slice of 17.9 μm thickness in the center of the channel height. To visualize the pathlines of the individual tracer particles, we average successive frames for $10\tau_{pv}$, yielding the micrographs shown in figures 2.3, 2.5, 2.6, 2.7, and 2.8. The particles can be considered faithful tracers of the streamlines because tracer particle advection dominates over diffusion, as described by the particle-scale Péclet number $\mathrm{Pe} \equiv (Q/A)D_p/\mathcal{D} > 10^5 \gg 1$, where $\mathcal{D} = k_B T/3\pi\eta_0 D_t = 6 \times 10^{-3}\ \mu\mathrm{m}^2/s$ is the Stokes-Einstein particle diffusivity. We thus refer to the particle pathline measurements as fluid streamlines throughout chapter 2.

A.3 Hele-Shaw chamber fabrication

To characterize the macro-scale partitioning of flow in chapter 4, we fabricate an unconsolidated stratified porous medium in a Hele-Shaw assembly. We 3-D print an open-faced rectangular cell with span-wise (y-direction) cross-sectional area $A = 3\ \mathrm{cm} \times 0.4\ \mathrm{cm}$ and stream-wise (x-direction) length $L = 5\ \mathrm{cm}$ using a clear methacrylate-based resin

(FLGPCL04, *Formlabs Form3*, see §A.2). To ensure an even distribution of flow at the boundaries, we use three inlets and outlets equally-spaced along the cross-section. We then fill the cell with spherical borosilicate glass beads of distinct diameters arranged in parallel strata using a temporary partition, with bead diameters $d_p = 1000$ to 1400 μm (*Sigma Aldrich*) and 212 to 255 μm (*Mo-Sci*) for the coarse (subscript C) and fine (subscript F) strata, respectively. The strata have equal cross-sectional areas $A_C \approx A_F \approx A/2$ and thus the area ratio $\tilde{A} \equiv A_C/A_F \approx 1$. Steel mesh with a 150 μm pore size cutoff placed over the inlet and outlet tubing prevents the beads from exiting the cell. We tamp down the beads for 30 min to form a dense random packing with a porosity $\varphi_V \sim 0.4$[182]. We then screw the whole assembly shut with an overlying acrylic sheet cut to size, sandwiching a thin sheet of polydimethylsiloxane to provide a watertight seal.

Flow control For all macro-scale experiments, we use a *Harvard Apparatus* PHD 2000 syringe pump to first introduce the test fluid—either the polymer solution or the polymer-free solvent, which acts as a Newtonian control—at a constant flow rate Q for at least one pore volume $t_{PV} \equiv \varphi_V AL/Q$ before imaging to ensure an equilibrated starting condition.

Permeability Because the permeability of a homogeneous porous medium or an isolated stratum in a stratified medium varies as $\sim d_p^2$, we estimate the permeability of each strata within th Hele-Shaw assembly by scaling k_C and k_F with the differences in bead size accordingly—yielding $k \approx 440$ μm^2 ($\tilde{k} \approx 26$) for the entire stratified medium, in reasonable agreement with the measured $k = 270$ μm^2 for the entire medium. For both assemblies, we define a characteristic shear rate of the entire medium $\dot{\gamma}_I \equiv Q/\left(A\sqrt{\varphi_V k}\right)$ as the ratio between the characteristic pore flow speed $Q/(\varphi_V A)$ and length scale $\sqrt{k/\varphi_V}$,[137,160] which range from $\dot{\gamma}_I \approx 0.2$ to 26 s^{-1} in all our experiments.

A.3.1 Hele-Shaw chamber imaging

We visualize the macro-scale scalar transport by the fluid by introducing a step change in the concentration of a dilute dye (0.1 wt.% green food coloring, *McCormick*) and record the infiltration of the dye front using a DSLR camera (*Sony* α6300). To track the progression of the dye as it is advected by the flow, we determine the "breakthrough" curve halfway along the length of the medium ($x = L/2$) by measuring the dye intensity C averaged across the entire medium cross-section, normalized by the difference in intensities of the final dye-saturated and initial dye-free medium, C_f and C_0, respectively: $\tilde{C} \equiv \left(\langle C \rangle_y - \langle C_0 \rangle_y\right) / \left(\langle C_f \rangle_y - \langle C_0 \rangle_y\right)$. Repeating this procedure for individual strata (subscript i) and tracking the variation of the stream-wise position X_i at which $\tilde{C}_i = 0.5$ with time provides a measure for the superficial velocity $U_i = \mathrm{d}X_i/\mathrm{d}t$ in each stratum.

A.4 3D porous media fabrication

We pack spherical borosilicate glass beads (*Mo-Sci*) in square quartz capillaries ($A = 3.2$ mm$\times$ 3.2 mm; *Vitrocom*), densify them by tapping, and lightly sinter the beads for 1 to 3 min at 1000—resulting in a dense random packing with $\varphi_V \approx 0.41$ and tortuosity ≈ 2, as we previously measured using confocal microscopy.[183,274] To control and characterize flow in the pore space, we glue inlet and outlet tubing into the inlet and outlet of the medium, respectively, with valves for pressure taps.[183] We fabricate three different media: a homogeneous coarse medium (glass bead diameter $d_p = 300$ to 355 µm; pore throat diameter $d_t \approx 0.16 d_p \approx 52$ µm; chapter 3), a homogeneous fine medium ($d_p = 125$ to 155 µm; $d_t \approx 22$ µm; chapter 4), and a stratified medium with parallel coarse and fine strata (Chap-

ter 3), each composed of the same beads used to make the homogeneous media, again with equal cross-section areas, $\tilde{A} = A_C/A_F \approx 1$.[6,184] The length of the medium along the imposed flow direction is $\Delta L = 8.1$ cm (coarse), $\Delta L = 2.8$ cm (fine) $\Delta L = 2.3$ cm (stratified).

Pressure drop We measure the pressure drop across the medium ΔP using an *Omega PX26* differential pressure transducer, averaging measurements obtained over 60 min; the temporal fluctuations in these measurements are minimal, and as a result, the corresponding error bars in reported pressure drop and apparent viscosity figures are smaller than the symbol size (or else are shown).

Permeability For each medium, we determine the permeability via Darcy's law using experiments with pure water, yielding $k_C = 79$ and $k_F = 8.6$ μm^2 for the homogeneous coarse and fine media, respectively—in reasonable agreement with our previous measurements of similar media[183] and with the prediction of the established Kozeny-Carman relation.[185] The measured permeability for the entire stratified porous medium is $k = 32$ μm^2, in reasonable agreement with the relation $k \approx \tilde{A}k_C + (1-\tilde{A})k_F \approx 44$ μm^2, obtained by considering the strata as separated homogeneous media providing parallel resistance to flow. The permeability ratio between the two strata is then $\tilde{k} \equiv k_C/k_F \approx 9$. Because the permeability of a homogeneous porous medium or an isolated stratum in a stratified medium varies as $\sim d_p^2$, we estimate the permeability of each strata within the Hele-Shaw assembly by scaling k_C and k_F with the differences in bead size accordingly—yielding $k \approx 440$ μm^2 ($\tilde{k} \approx 26$) for the entire stratified medium, in reasonable agreement with the measured $k = 270$ μm^2 for the entire medium. For both assemblies, we define a characteristic shear rate of the entire medium $\dot{\gamma}_I \equiv Q/\left(A\sqrt{\varphi_V k}\right)$ as the ratio between the characteristic pore

Parameter	Coarse porous medium (Ch. 3)	Fine porous medium (Ch. 4)
d_p	300–355 (μm)	125–155 (μm)
d_t	55 (μm)	22 (μm)
k	79 (μm^2)	8.6 (μm^2)
ΔL	8.1 (cm)	2.8 (cm)

Table A.2: Parameters of coarse (Ch. 3) and fine (Ch. 4 sintered 3D porous media. Glass bead diameter d_p, mean pore throat size d_t, measured permeability k, and length ΔL. All porous media have cross sectional area set by the quartz capillary $A = 3.2$ mm $\times$ 3.2 mm.

flow speed $Q/(\varphi_V A)$ and length scale $\sqrt{k/\varphi_V}$,[137,160] which range from $\dot{\gamma}_I \approx 0.2$ to 26 s^{-1} in all our experiments.

A.4.1 3D sintered media flow control

For all pore-scale experiments, before each experiment, we infiltrate the medium to be studied first with isopropyl alcohol (IPA) to prevent trapping of air bubbles and then displace the IPA by flushing with water. We then displace the water with the miscible polymer solution, seeded with 5 ppm of fluorescent carboxylated polystyrene tracer particles (*Invitrogen*), $D_t = 200$ nm in diameter. This solution is injected into the medium at a constant Q using *Harvard Apparatus* syringe pumps—a PHD 2000 for $Q > 1$ mL/hr or a pico elite for $Q < 1$ mL/hr—for at least 3 hours to reach an equilibrated state before flow characterization. After each subsequent change in Q, the flow is given 1 hour to equilibrate before imaging.

A.4.2 3D porous media imaging

To visualize the pore-scale flow in situ, we seed the polymer solution with 5 ppm of fluorescent carboxylated polystyrene tracer particles (*Invitrogen*), $D_t = 200$ nm in diameter.

We monitor the flow in individual pores using a *Nikon* A1R+ laser scanning confocal fluorescence microscope with a 488 nm excitation laser and a 500-550 nm sensor detector; the tracer particles have excitation between 480 and 510 nm with an excitation peak at 505 nm, and emission between 505 and 540 nm with an emission peak at 515 nm. These particles are faithful tracers of the underlying flow field since the Péclet number remains above $\mathrm{Pe} \equiv (Q/A)D_t/\mathcal{D} > 10^5 \gg 1$, where $\mathcal{D} = k_B T/3\pi\eta D_t = 6 \times 10^{-3}$ $\mu\mathrm{m}^2/\mathrm{s}$ is the Stokes-Einstein particle diffusivity. We then visualize the flow using a 10× objective lens with a variable field of view and temporal resolution—159 μm by 159 μm at 60 frames per second for pores $d_p = 125$ to 155μm, and 318 μm by 318 μm at 30 frames per second for pores $d_p = 300$ to 355μm—with the confocal resonant scanner and a constant spatial resolution of 0.62 μm from an optical slice of 8 μm thickness at a depth of $\sim$ 100's of μm within the medium. We represent the movies thus obtained by intensity-averaging images over a time scale $\approx$ 2.5 μm/ (Q/A), producing particle pathlines that well-approximate the instantaneous flow streamlines. To visualize the pore space, we also dye the solution with 0.5 ppm of rhodamine red dye, which has an excitation wavelength between 480 and 600 nm with an excitation peak at 560 nm, and emission between 550 and 700 nm with an emission peak at 580 nm. The dyed pore space is imaged using a 561 nm excitation laser, and detected with a 570–620 nm sensor. Choice of these fluorescent markers allows us to image both the pore space and the dynamic flow within it at high resolution, with no observable cross talk or bleed through on the laser channels.

Imaging routine We have two imaging procedures to access flow changes over different timescales. To monitor long-time spectral characteristics of the flow, we monitor the flow **continuously** for a single 10 min interval. To monitor the slow changes in the flow field

over time, we instead record the flow in **intermittently** in 2 s intervals every 4 min for 60 min.

For chapter 3, we image nine pores randomly chosen near the inlet of the medium and ten pores randomly chosen near the outlet using the intermittent imaging protocol; we do not observe noticeable differences in the results obtained depending on position along the medium. Of the 19 pores imaged, 12 exhibit a well-defined critical Wi_c below which the pore-scale flow is stable and laminar, above which the pore-scale flow is unstable. For the other 7 pores ($\approx$ 37%) we cannot determine a clear Wi_c within the range of Wi explored in our experiments; thus, the analysis in Figs. 3.5E–F omits these pores. The analysis in Fig. 3.10, however, does not. For chapter 4 we image 10 pores in the middle of the medium using the intermittent imaging procedure and 10 pores in the middle using the continuous imaging procedure. We see no appreciable difference in the measured $\langle \chi \rangle_{t,V}$ between these two protocols (Fig. 4.2).

A.5 Analysis of pore-scale flow

A.5.1 Processing of PIV data

We track the two-dimensional instantaneous velocity field within each pore with particle image velocimetry (PIV) using PIVLab.[186] We iterate PIV down to a final spatial discretization $\Delta x = 7.74$ μm (coarse) or $\Delta x = 12.43$ μm (fine). For our intermittent imaging protocol, we observe minimal fluctuations over the course of each 2 s interval, so we average the velocity field obtained in each such interval to give a quasi-steady snapshot of the velocity field at each time point separated by 4 min, $\mathbf{u}(\mathbf{x}, t) \equiv (u(\mathbf{x}, t), v(\mathbf{x}, t))$ where the position vector $\mathbf{x} \equiv (x, y)$. For our continuous imaging protocol, we instead average only

over 3 frames (100 ms) to minimize PIV noise, but retain high frequency spectral data.

Velocity fluctuations In our analysis of the pore-scale flow, the root mean square velocity of a pixel is calculated as the temporal root mean square of the magnitude of the fluctuation from the temporal mean,[275] $u_{\mathrm{rms}}(\mathbf{x}) = \left(\langle||\mathbf{u}(\mathbf{x},t) - \langle\mathbf{u}(\mathbf{x},t)\rangle_t||^2\rangle_t\right)^{1/2}$. We normalize this quantity by the velocity magnitude averaged over time and space (over all pixels) for each pore, $\langle u\rangle_{t,\mathbf{x}} = \langle\langle||\mathbf{u}(\mathbf{x},t)||\rangle_t\rangle_{\mathbf{x}}$. To quantify velocity fluctuations arising from unstable flow, we compute the velocity fluctuations $\mathbf{u}'(\mathbf{x},t) = \mathbf{u}(\mathbf{x},t) - \langle\mathbf{u}(\mathbf{x},t)\rangle_t$.

Velocity gradients This fluctuation field enables us to calculate the velocity gradient tensor associated with flow fluctuations, $s'_{ij} = \partial u'_i/\partial x_j$, pixel-by-pixel. In general, to compute the discrete derivatives, we use the central difference method, in which the derivative of f with respect to x evaluated around $x = x_0$ is given by

$$\left(\frac{\partial f}{\partial x}\right)_{x_0} \approx \frac{1}{2}\left(\frac{f(x_0+\Delta x) - f(x_0)}{\Delta x} + \frac{f(x_0) - f(x_0-\Delta x)}{\Delta x}\right).$$

On the boundaries of data sets, this central difference is replaced with the forward or backward finite difference (first or second term respectively).

A.5.2 Distributions of key flow parameters

To characterize the distribution of key flow parameters in the porous medium in the stable laminar case, we use our PIV measurements well below the onset of elastic turbulence (at $\dot{\gamma}_I = 0.48\ \mathrm{s}^{-1}$) to determine the base laminar flow field throughout the pore space. We then estimate the shear rate $\dot{\gamma} = \left(\partial u_i/\partial x_j + \partial u_j/\partial x_i\right)/3$ using the in-plane component $\dot{\gamma} \approx \partial u/\partial y + \partial v/\partial x$, since our 2D PIV cannot resolve out-of-plane velocity components. This approximation then allows us to estimate the magnitude of the spatially-varying Weis-

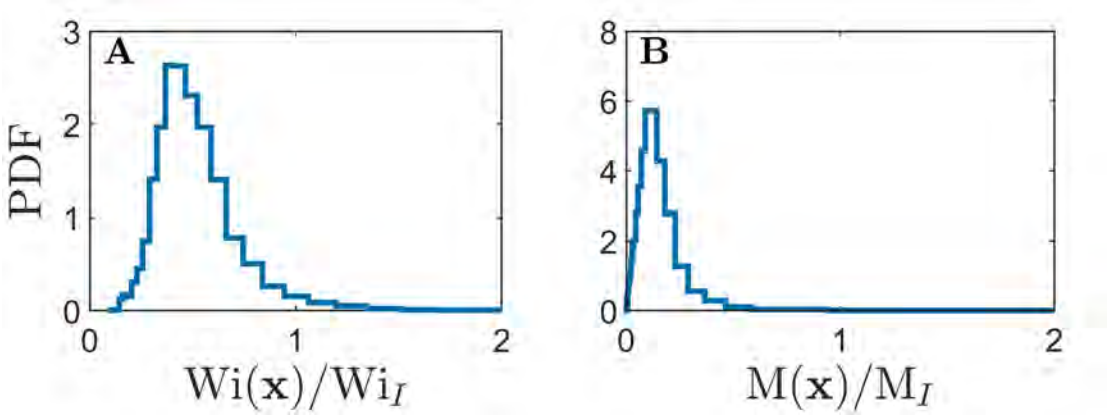

Figure A.5: Distributions of flow parameters for 19 imaged pores in the laminar steady flow regime. **(A)** The local Wi is broadly distributed; the characteristic macroscopically-defined Wi_I represents the upper bound of this distribution. **(B)** The local M is also broadly distributed; the characteristic macroscopically-defined M_I represents the upper bound of this distribution.

senberg number $\mathrm{Wi}(\mathbf{x}) \equiv N_1\big(\dot{\gamma}(\mathbf{x})\big)/2\sigma\big(\dot{\gamma}(\mathbf{x})\big)$ pixel-by-pixel using the rheologically-measured N_1 and σ. The distribution of the measured $\mathrm{Wi}(\mathbf{x})$ for 19 imaged pores is shown in Fig. A.5A. As shown by the data, the characteristic interstitial Weissenberg number $\mathrm{Wi}_I \equiv N_1(\dot{\gamma}_I)/2\sigma(\dot{\gamma}_I)$ defined using imposed macroscopic flow conditions and macroscopic characteristics of the porous medium represents the upper limit of this distribution.

Elastic instabilities have been studied in a range of simplified geometries, and are typically parametrized using the Weissenberg number. Thus, we also parametrize the different flow rates tested primarily using the Weissenberg number; however, we note that the onset of unstable flow due to streamline curvature can be described using a linear stability analysis of the Stokes equation for a viscoelastic fluid.[76,77] This analysis indicates that the largest destabilizing term, which leads to the generation of unstable flow locally, is proportional to $\mathrm{M} \equiv \sqrt{\mathrm{Wi} \cdot \mathrm{De}}$, where the Deborah number $\mathrm{De} \equiv \lambda(\dot{\gamma})||\mathbf{u}||\kappa$ compares the polymer relaxation time λ to the flow time scale $(||\mathbf{u}||\kappa)^{-1}$ and κ is a measure of the local streamline

curvature.[154] In this picture, elastic stresses build up in the flow, generating elastic turbulence when M exceeds a critical value M_c, found to be $\approx$ 6 to 20 in experiments performed in diverse simplified geometries.[2,76–79,154,276] Thus, the transition to elastic turbulence could also be parameterized using a characteristic interstitial $M_I \equiv \sqrt{\frac{N_1(\dot{\gamma}_I)}{\eta_0 \dot{\gamma}_I} \cdot \lambda(\dot{\gamma}_I)(Q/A)\kappa_I}$, again defined using imposed macroscopic flow conditions and macroscopic characteristics of the porous medium; here the characteristic streamline curvature is set by the pore length scale, with $\kappa_I = 1/\left(2\sqrt{\varphi k}\right)$. We again use our measurements of the spatially-varying shear rate $\dot{\gamma}(\mathbf{x})$, as well as direct measurements of the spatially-varying local streamline curvature $\kappa(\mathbf{x})$, to compute the spatially-varying $M(\mathbf{x}) = \sqrt{\mathrm{Wi}\,(\mathbf{x}) \cdot \mathrm{De}\,(\mathbf{x})}$, pixel-by-pixel. The distribution of the measured $M(\mathbf{x})$ for all 19 imaged pores is shown in Fig. A.5B. As shown by the data, the characteristic interstitial M_I defined using imposed macroscopic flow conditions and macroscopic characteristics of the porous medium represents the upper limit of this distribution. For our experiments, M_I ranges from 3.3 to 8.1. The range of $M_{c,i}$ at which pores become unstable is measured to be $\approx$ 5.5 to 7.9, in good agreement with the range of $\approx$ 6 to 20 observed in simplified geometries.

A.5.3 Determination of pore-scale critical Weissenberg number

To determine the critical Weissenberg number in each pore, we first plot the fraction of time unstable F_t for each pore. To superpose the plots, we shift each curve by the Wi_{50}, defined by the point where $F_t = 0.5$, linearly interpolating between data points as needed: this procedure enables us to avoid noise in the limits $F_t \approx 0$ and $F_t \approx 1$. We define a constant shift of $\mathrm{Wi}_c = \mathrm{Wi}_{50} - 0.35$ (Table A.3), which minimizes the error in the power law fit $F_t \sim (\mathrm{Wi}_I/\mathrm{Wi}_c - 1)^{\alpha_f}$, where the exponent $\alpha_f \approx 0.4 \pm 0.1$ is obtained from

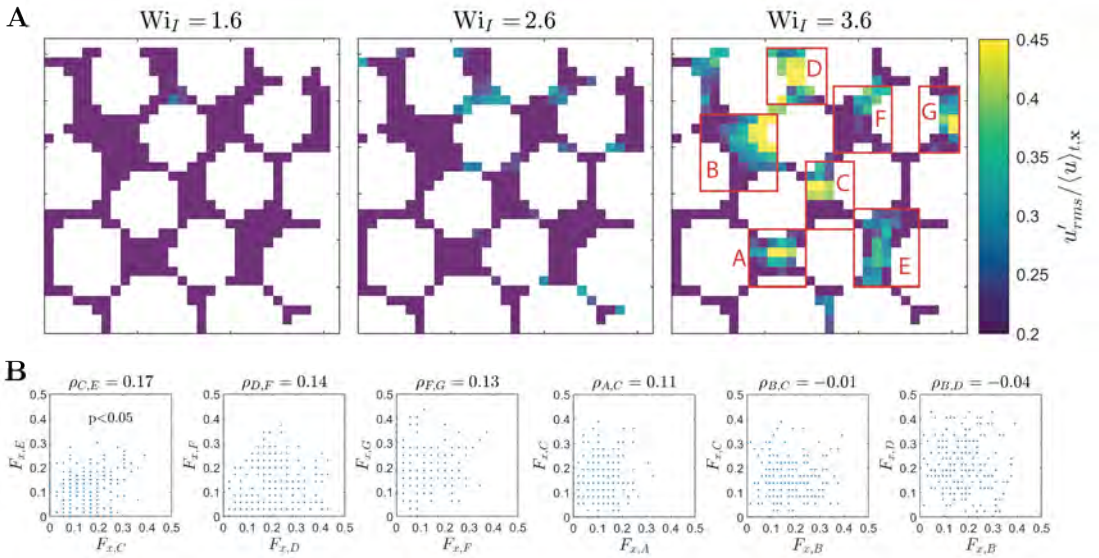

Figure A.6: Evaluating the possible role of flow correlations between neighboring pores. **A** Multi-pore imaging at three different flow rates indicates that localized regions of unstable flow (blue, green, yellow) coexist amidst regions of stable flow (purple). **B** To quantify possible correlations in the flow across neighboring pores, we measure the temporal variation of the instantaneous fraction of space $F_{x,i}$ that is unstable ($u'/\langle u \rangle_{t,\mathbf{x}} > 0.2$, where $\langle u \rangle_{t,\mathbf{x}}$ is taken over the entire multi-pore field of view) in each pore i, and assess the correlation between the different $F_{x,i}$ at each time, indicated by each blue point in the panels shown. The pore labels i are indicated in the third panel of **A**. The Pearson correlation coefficients obtained from the data for pores i and j are indicated by $\rho_{i,j}$. Only one pair of neighboring pores (C and E) shows a statistically significant correlation ($p < 0.05$, two-tailed t-test), but only with a weak correlation of $\rho_{C,E} = 0.17$; all other pairs of pores show no significant correlation in flow state. Thus, unstable pores may be weakly correlated to their closest neighbors, but these unstable regions are fairly independent from pores further away — supporting our finding of "porous individualism" in which different pores become unstable at different imposed flow conditions.

the best fit across all pores. Pores where Wi_c is ambiguous are omitted from this fit and the distribution shown in Fig. 2E-F.

A.6 Numerical solver

To model the flow between strata in chapter 4, flow is always compared between two strata. Equations 4.1, 4.2 and mass conservation $Q = Q_C + Q_F$ are solved numerically by generating an array of shear rates, inserted into 4.2. For each input shear rate $\dot{\gamma}_{I,C}$and exact pressure

Pore name	x (mm)	y (mm)	Wi_c
A	58.52	2.99	2.62
B	60.55	2.79	3.11
C	59.88	0.65	3.56
D	1.36	2.34	3.53
E	1.55	2.04	3.13
F	1.02	1.94	3.94
G	1.31	1.78	2.90
H	60.93	3.05	3.23
I	59.93	2.30	3.13
J	59.74	1.71	3.11
K	59.82	1.01	3.92
L	59.57	0.70	4.02
M	61.10	1.01	-
N	0.65	2.65	-
O	1.55	1.55	-
P	1.24	1.35	-
Q	1.47	1.06	-
R	1.03	0.91	-
S	60.18	2.71	-
T	17.33	1.41	-
U	18.10	2.50	-

Table A.3: Additional data on pores selected for imaging. Locations of the 19 pores (labeled A–S) selected at random throughout the medium for imaging and PIV. Positions are in reference to an arbitrary reference fiducial point. For pores with a well-defined onset, the fit Wi_c is given (see section A.5.3). Pores T and U are imaged continuously at select flow rates for Figs. 3.3 and 3.4 only. Locations for pores T and U are in reference to a different arbitrary reference fiducial point.

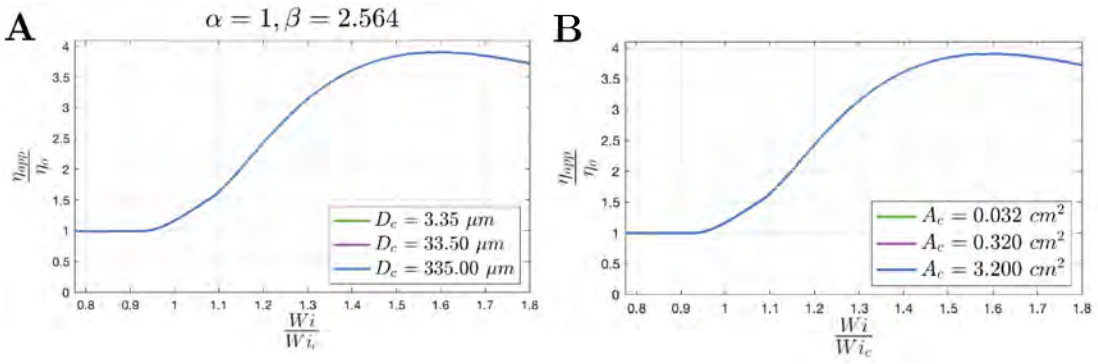

Figure A.7: Model insensitivity to absolute k_i and A_i A Modeled apparent viscosity for varying coarse layer grain diameter **B** varying coarse layer cross-sectional areas, both holding a constant area ratio of $\alpha = 1$ and permeability ratio of $\kappa = 6.6$.

output $\langle \Delta P_C \rangle_t$ in the coarse layer, the pressure in the fine layer $\langle \Delta P_F \rangle_t = \Delta P_C$ is matched by linear interpolation to give an estimate for the shear rate $\dot{\gamma}_{I,F}$ *via* Eq. 4.2. Comparing the coarsest layer against the remaining fine strata pairwise ensures that each output shear rate $\dot{\gamma}_{I,F}$ corresponds to the same input shear rate in the coarsest layer. The flow rate in each layer $Q_i = \dot{\gamma}_{I,i}\sqrt{\varphi_V k_i} A_i$ is calculated to yield the imposed constant total flow rate $Q = \Sigma Q_i$ and corresponding interstitial conditions $\dot{\gamma}_I$ and Wi_I. We confirm that the model is insensitive to particular absolute permeabilities and cross-sectional areas by computing the pressure drop across a 2-layer stratified system, varying permeability and cross-sectional areas and holding the area and permeability ratio constant A.7.

A.7 Other polymer flow effects in SLA channels

For simplicity, in this dissertation I have neglected several flow phenomena that sometimes arise for polymer solutions: namely, polymer surface adsorption, flow-induced chain migration, wall slip, and shear banding. The channel dimensions, pore sizes, solvent concentrations, and polymer concentrations used throughout this dissertation help minimize these

effects in order to isolate the influence of polymer elasticity and memory by minimizing these other phenomena, as quantified below. These phenomena may arise in other polymer solutions and geometries, and investigating the combined role of these phenomena is an important direction for continued work.

A.7.1 Surface adsorption

The first effect—polymer adsorption to the solid surfaces and eventual blockage of pore throats—has been documented for media with small pores.[40,41,277–279] However, this effect typically influences flow behavior in media having pore throats much smaller than those explored in our work: the steady state thickness of adsorbed polymers is on the order of polymer molecular dimensions, and for the HPAM polymer used in our experiments, this thickness is $\sim$ 100 nm.[280] Since the thickness of this adsorbed layer is over three orders of magnitude smaller than the smallest channel dimension $L_c = 400$ μm in our SLA channels, we do not expect this adsorption layer to appreciably impact the flow. Furthermore, pore blockage is typically exacerbated by the bridging of elongated polymers across the pore throats;[279] however, the fully-elongated contour length of the HPAM polymer is $NL_{mon} \approx 40$ μm, where N is the degree of polymerization and L_{mon} is the monomer Kuhn length. Since this fully-elongated contour length is an order of magnitude smaller than the smallest channel dimension L_c or throat size L_t, we again do not expect polymer blockage of the pore throats to play a considerable role in our experiments.

A.7.2 Flow-induces chain migration and wall slip

Similarly, while flow-induced chain migration and wall slip frequently arise in confined flows of polymer solutions, they give rise to polymer concentration inhomogeneities over length scales $\sim$ 0.1 to 10μm,[281] one to three orders of magnitude smaller than L_c or L_t. We estimate this length scale by balancing the influence of chain diffusion with elastic normal stresses:[282] $L_d = \frac{9\sqrt{\pi}}{128}\frac{N_1-N_2}{nk_BT}h^*R_g$, where n is the polymer number density in the bulk solution, k_BT is thermal energy, and R_g is the polymer radius of gyration. To determine an upper bound for L_d, we take the value of the first normal stress difference N_1 at the maximal shear rate using our shear rheology measurements, and take the second normal stress difference N_2 to be zero. The parameter $h^* = \frac{\zeta}{\eta_s}\sqrt{\frac{H}{36\pi^3k_BT}} = 0.07$ quantifies hydrodynamic interactions, where η_s is the shear viscosity of the background solvent, $H \approx k_BT/2R_g^2$ is a characteristic polymer spring constant, $\zeta \approx 4H\lambda$ is the monomer hydrodynamic friction coefficient, and λ is the polymer relaxation time estimated using shear rheology as described in Section 2. Using these values, we obtain $L_d \approx 20R_g = 4$ μm—in reasonable agreement with measurements that indicate $L_d \approx NL_{mon}/3 \approx 14$ μm.[283] These estimated values are one to two orders of magnitude smaller than L_c; thus, we do not expect flow-induced migration to appreciably impact the flow.

Polymer wall slip can play a key role when the flow channel has dimensions approaching molecular dimensions, and for concentrated polymer solutions with a high viscosity ratio $\beta \equiv \eta_0/\eta_s$, where η_0 is the maximal solution shear viscosity and η_s is the shear viscosity of the background solvent. However, in our experiments, L_c is three orders of magnitude larger than R_g, and our polymer solution is dilute, with $\beta = 1.7$ close to one. Indeed, an upper bound for the length scale over which wall slip occurs L_s can be estimated[189] as $L_s \leq$

$\beta R_g = 330$ nm. This value is over three orders of magnitude smaller than L_c; thus, we do not expect that wall slip appreciably impacts the flow. Further, we can use this length scale to estimate an upper bound for the wall slip speed U_s using the wall shear rate $\dot{\gamma}$ in the pore throat at the highest flow rate tested in our experiments; we calculate $U_s \leq L_s\dot{\gamma} \approx 7$ $\mu m/s$, over two orders of magnitude smaller than the characteristic flow speeds explored in our experiments. This estimate again suggests that wall slip does not appreciably impact the flow.

A.7.3 Shear-banding

Shear-banding of polymers often arises during the flow of concentrated polymer solutions. However, our experiments probe the case of dilute polymer solutions, in which polymer overlap likely does not influence flow behavior and in which shear banding is not expected to occur.[189] This expectation is further supported by our shear rheology measurements: over the experimental range of shear rates, our measurements of rate-controlled shear rheology indicate that the shear stress varies approximately linearly with shear rate, with a shear thinning exponent ≈ 0.92; by contrast, shear banding typically occurs for solutions in which the shear stress varies non-monotonically with imposed shear rate.[190,191] We therefore do not expect that shear banding plays an appreciable role in our experiments.

References

[1] Christopher A Browne, Audrey Shih, and Sujit S Datta. Pore-scale flow characterization of polymer solutions in microfluidic porous media. *Small*, 16(9):1903944, 2019. doi: https://doi.org/10.1002/smll.201903944.

[2] Christopher A Browne, Audrey Shih, and Sujit S Datta. Bistability in the unstable flow of polymer solutions through pore constriction arrays. *Journal of Fluid Mechanics*, 890, 2020.

[3] Christopher A. Browne and Sujit S. Datta. Elastic turbulence generates anomalous flow resistance in porous media. *Science Advances*, 7:eabj2619, 2021.

[4] Christopher A Browne, Daniel B Amchin, Joanna Schneider, and Sujit S. Datta. Infection percolation: A dynamic network model of disease spreading. *Frontiers in Physics*, 9:171, 2021.

[5] Manish Kumar, Soroush Aramideh, Christopher A Browne, Sujit S Datta, and Arezoo M Ardekani. Numerical investigation of multistability in the unstable flow of a polymer solution through porous media. *Physical Review Fluids*, 6(3):033304, 2021.

[6] Nancy B Lu, Amir A Pahlavan, Christopher A Browne, Daniel B Amchin, Howard A Stone, and Sujit S Datta. Forced imbibition in stratified porous media. *Physical Review Applied*, 14(5):054009, 2020.

[7] Nancy B Lu, Christopher A Browne, Daniel B Amchin, Janine K Nunes, and Sujit S Datta. Controlling capillary fingering using pore size gradients in disordered media. *Physical Review Fluids*, 4(8):084303, 2019.

[8] Margaret G O'Connell, Nancy B Lu, Christopher A Browne, and Sujit S Datta. Cooperative size sorting of deformable particles in porous media. *Soft matter*, 15 (17):3620–3626, 2019.

[9] John C Wyngaard. *Turbulence in the Atmosphere*. Cambridge University Press, 2010.

[10] Ricard Alert, Jaume Casademunt, and Jean-François Joanny. Active turbulence. *Annual Review of Condensed Matter Physics*, 13, 2021.

[11] GV Vinogradov and VN Manin. An experimental study of elastic turbulence. *Kolloid-Zeitschrift und Zeitschrift für Polymere*, 201(2):93–98, 1965.

[12] RJ Marshall and AB Metzner. Flow of viscoelastic fluids through porous media. *Industrial & Engineering Chemistry Fundamentals*, 6(3):393–400, 1967.

[13] Victor Steinberg. Elastic turbulence: An experimental view on inertialess random flow. *Annual Review of Fluid Mechanics*, 53:27–58, 2021.

[14] L. Pan, A. Morozov, C. Wagner, and P. E. Arratia. Nonlinear elastic instability in channel flows at low Reynolds numbers. *Phys. Rev. Lett.*, 110(17):174502, 2013.

[15] Derek M Walkama, Nicolas Waisbord, and Jeffrey S Guasto. Disorder suppresses chaos in viscoelastic flows. *Physical Review Letters*, 124(16):164501, 2020.

[16] Robert Byron Bird, Robert Calvin Armstrong, and Ole Hassager. *Dynamics of polymeric liquids. Vol. 1: Fluid mechanics*. John Wiley and Sons, Inc., 1987.

[17] R Byron Bird, Warren E Stewart, and Edwin N Lightfoot. *Transport Phenomena*. John Wiley and Sons, Inc., 1960.

[18] Jennifer Segui. Non-newtonian fluids: The pouring ketchup quandary, Apr 2013. URL https://www.comsol.com/blogs/non-newtonian-fluids-the-pouring-ketchup-quandary/.

[19] William Walter Graessley. *Polymeric liquids and networks: dynamics and rheology*. Garland Science, 2008.

[20] Matthew T Balhoff and Karsten E Thompson. A macroscopic model for shear-thinning flow in packed beds based on network modeling. *Chemical Engineering Science*, 61(2):698–719, 2006.

[21] Kenneth S Sorbie. *Polymer-Improved Oil Recovery*. Springer Science & Business Media, 2013.

[22] Y Du, L Guan, et al. Field-scale polymer flooding: lessons learnt and experiences gained during past 40 years. In *SPE International Petroleum Conference in Mexico*. Society of Petroleum Engineers, 2004.

[23] Demin Wang, Huifen Xia, Shuren Yang, Gang Wang, et al. The influence of visco-elasticity on micro forces and displacement efficiency in pores, cores and in the field. In *SPE EOR Conference at Oil & Gas West Asia*. Society of Petroleum Engineers, 2010.

[24] Demin Wang, Gang Wang, Huifen Xia, et al. Large scale high visco-elastic fluid flooding in the field achieves high recoveries. In *SPE Enhanced Oil Recovery Conference*. Society of Petroleum Engineers, 2011.

[25] BB Sandiford et al. Laboratory and field studies of water floods using polymer solutions to increase oil recoveries. *Journal of Petroleum Technology*, 16(08):917–922, 1964.

[26] Malcolm J Pitts, Tom A Campbell, Harry Surkalo, Kon Wyatt, et al. Polymer flood of the rapdan pool, saskatchewan, canada. *SPE Reservoir Engineering*, 10(03):183–186, 1995.

[27] Bing Wei, Laura Romero-Zerón, and Denis Rodrigue. Oil displacement mechanisms of viscoelastic polymers in enhanced oil recovery (eor): a review. *Journal of Petroleum Exploration and Production Technology*, 4(2):113–121, 2014.

[28] ECM Vermolen, MJT Van Haasterecht, SK Masalmeh, et al. A systematic study of the polymer visco-elastic effect on residual oil saturation by core flooding. In *SPE EOR Conference at Oil and Gas West Asia*. Society of Petroleum Engineers, 2014.

[29] DS Roote. Technology status report: in situ flushing. *Ground Water Remediation Technology Analysis Center (available at http://www. gwrtac. org)*, 1998.

[30] Steven W Giese and Susan E Powers. Using polymer solutions to enhance recovery of mobile coal tar and creosote dnapls. *Journal of contaminant hydrology*, 58(1-2): 147–167, 2002.

[31] Mohamed IM Darwish, John E McCray, Peter K Currie, and Pacelli LJ Zitha. Polymer-enhanced dnapl flushing from low-permeability media: An experimental study. *Groundwater Monitoring & Remediation*, 23(2):92–101, 2003.

[32] Megan M Smith, Jeff AK Silva, Junko Munakata-Marr, and John E McCray. Compatibility of polymers and chemical oxidants for enhanced groundwater remediation. *Environmental science & technology*, 42(24):9296–9301, 2008.

[33] Dwight L Dauben and DE Menzie. Flow of polymer solutions through porous media. *Journal of Petroleum Technology*, 19(08):1065–1073, 1967.

[34] G Chauveteau and M Moan. The onset of dilatant behaviour in non-inertial flow of dilute polymer solutions through channels with varying cross-sections. *Journal de Physique Lettres*, 42(10):201–204, 1981.

[35] Simon J Haward and Jeffrey A Odell. Viscosity enhancement in non-newtonian flow of dilute polymer solutions through crystallographic porous media. *Rheologica acta*, 42(6):516–526, 2003.

[36] JA Odell and SJ Haward. Viscosity enhancement in non-newtonian flow of dilute aqueous polymer solutions through crystallographic and random porous media. *Rheologica acta*, 45(6):853–863, 2006.

[37] Nematollah Zamani, Igor Bondino, Roland Kaufmann, and Arne Skauge. Effect of porous media properties on the onset of polymer extensional viscosity. *Journal of Petroleum Science and Engineering*, 133:483–495, 2015.

[38] Arne Skauge, Nematollah Zamani, Jørgen Gausdal Jacobsen, Behruz Shaker Shiran, Badar Al-Shakry, and Tormod Skauge. Polymer flow in porous media: Relevance to enhanced oil recovery. *Colloids and Interfaces*, 2(3):27, 2018.

[39] Chun Huh, Gary Arnold Pope, et al. Residual oil saturation from polymer floods: laboratory measurements and theoretical interpretation. In *SPE Symposium on Improved Oil Recovery*. Society of Petroleum Engineers, 2008.

[40] A Zaitoun, N Kohler, et al. Two-phase flow through porous media: effect of an adsorbed polymer layer. In *SPE Annual Technical Conference and Exhibition*. Society of Petroleum Engineers, 1988.

[41] A Zaitoun, H Bertin, D Lasseux, et al. Two-phase flow property modifications by polymer adsorption. In *SPE/DOE improved oil recovery symposium*. Society of Petroleum Engineers, 1998.

[42] G Chauveteau, M Moan, and A Magueur. Thickening behaviour of dilute polymer solutions in non-inertial elongational flows. *Journal of non-newtonian fluid mechanics*, 16(3):315–327, 1984.

[43] Jonathan Mitchell, Kyle Lyons, Andrew M Howe, and Andrew Clarke. Viscoelastic polymer flows and elastic turbulence in three-dimensional porous structures. *Soft matter*, 12(2):460–468, 2016.

[44] Andrew Clarke, Andrew M Howe, Jonathan Mitchell, John Staniland, Laurence A Hawkes, et al. How viscoelastic-polymer flooding enhances displacement efficiency. *SPE Journal*, 21(03):675–687, 2016.

[45] Guido Boffetta, Antonio Celani, and Stefano Musacchio. Two-dimensional turbulence of dilute polymer solutions. *Physical review letters*, 91(3):034501, 2003.

[46] Yonggang Liu and Victor Steinberg. Single polymer dynamics in a random flow. In *Macromolecular Symposia*, volume 337, pages 34–43. Wiley Online Library, 2014.

[47] Charles M Schroeder, Hazen P Babcock, Eric SG Shaqfeh, and Steven Chu. Observation of polymer conformation hysteresis in extensional flow. *Science*, 301(5639): 1515–1519, 2003.

[48] Charles M Schroeder, Rodrigo E Teixeira, Eric SG Shaqfeh, and Steven Chu. Characteristic periodic motion of polymers in shear flow. *Physical review letters*, 95(1): 018301, 2005.

[49] Rodrigo E Teixeira, Hazen P Babcock, Eric SG Shaqfeh, and Steven Chu. Shear thinning and tumbling dynamics of single polymers in the flow-gradient plane. *Macromolecules*, 38(2):581–592, 2005.

[50] GK Batchelor. The stress generated in a non-dilute suspension of elongated particles by pure straining motion. *Journal of Fluid Mechanics*, 46(4):813–829, 1971.

[51] DV Boger. Viscoelastic flows through contractions. *Annual review of fluid mechanics*, 19(1):157–182, 1987.

[52] A Mongruel and M Cloitre. Extensional flow of semidilute suspensions of rod-like particles through an orifice. *Physics Of Fluids*, 7(11):2546–2552, 1995.

[53] A Mongruel and M Cloitre. Axisymmetric orifice flow for measuring the elongational viscosity of semi-rigid polymer solutions. *Journal of non-newtonian fluid mechanics*, 110(1):27–43, 2003.

[54] LE Rodd, JJ Cooper-White, DV Boger, and Gareth Huw McKinley. Role of the elasticity number in the entry flow of dilute polymer solutions in micro-fabricated contraction geometries. *Journal of Non-Newtonian Fluid Mechanics*, 143(2-3):170–191, 2007.

[55] Francesco Del Giudice, Simon J Haward, and Amy Q Shen. Relaxation time of dilute polymer solutions: A microfluidic approach. *Journal of Rheology*, 61(2):327–337, 2017.

[56] SJ Haward. Microfluidic extensional rheometry using stagnation point flow. *Biomicrofluidics*, 10(4):043401, 2016.

[57] Thomas J Ober, Simon J Haward, Christopher J Pipe, Johannes Soulages, and Gareth H McKinley. Microfluidic extensional rheometry using a hyperbolic contraction geometry. *Rheologica Acta*, 52(6):529–546, 2013.

[58] Gabriel Juarez and Paulo E Arratia. Extensional rheology of dna suspensions in microfluidic devices. *Soft Matter*, 7(19):9444–9452, 2011.

[59] François Ingremeau and Hamid Kellay. Stretching polymers in droplet-pinch-off experiments. *Physical Review X*, 3(4):041002, 2013.

[60] Shaurya Sachdev, Aswin Muralidharan, and Pouyan E Boukany. Molecular processes leading to "necking" in extensional flow of polymer solutions: Using microfluidics and single dna imaging. *Macromolecules*, 49(24):9578–9585, 2016.

[61] Leidy Nallely Jimenez, Jelena Dinic, Nikhila Parsi, and Vivek Sharma. Extensional relaxation time, pinch-off dynamics, and printability of semidilute polyelectrolyte solutions. *Macromolecules*, 51(14):5191–5208, 2018.

[62] Anna V Walter, Leidy N Jimenez, Jelena Dinic, Vivek Sharma, and Kendra A Erk. Effect of salt valency and concentration on shear and extensional rheology of aqueous polyelectrolyte solutions for enhanced oil recovery. *Rheologica Acta*, 58(3-4): 145–157, 2019.

[63] Gerald G Fuller, Cheryl A Cathey, Brent Hubbard, and Beth E Zebrowski. Extensional viscosity measurements for low-viscosity fluids. *Journal of Rheology*, 31(3): 235–249, 1987.

[64] Cheryl A Cathey and Gerald G Fuller. Uniaxial and biaxial extensional viscosity measurements of dilute and semi-dilute solutions of rigid rod polymers. *Journal of non-newtonian fluid mechanics*, 30(2-3):303–316, 1988.

[65] David A Hoagland and RK Prud'Homme. Hydrodynamic chromatography as a probe of polymer dynamics during flow through porous media. *Macromolecules*, 22 (2):775–781, 1989.

[66] Hays S Rye, Jonathan M Dabora, Mark A Quesada, Richard A Mathies, and Alexander N Glazer. Fluorometric assay using dimeric dyes for double-and single-stranded dna and rna with picogram sensitivity. *Analytical biochemistry*, 208(1): 144–150, 1993.

[67] Nerayo P Teclemariam, Victor A Beck, Eric SG Shaqfeh, and Susan J Muller. Dynamics of DNA polymers in post arrays: Comparison of single molecule experiments and simulations. *Macromolecules*, 40(10):3848–3859, 2007.

[68] Orin L Hemminger, Pouyan E Boukany, Shi-Qing Wang, and LJ Lee. Flow pattern and molecular visualization of dna solutions through a 4: 1 planar microcontraction. *Journal of Non-Newtonian Fluid Mechanics*, 165(23-24):1613–1624, 2010.

[69] Thomas T Perkins, Douglas E Smith, and Steven Chu. Single polymer dynamics in an elongational flow. *Science*, 276(5321):2016–2021, 1997.

[70] Douglas E Smith and Steven Chu. Response of flexible polymers to a sudden elongational flow. *Science*, 281(5381):1335–1340, 1998.

[71] S Gerashchenko, C Chevallard, and V Steinberg. Single-polymer dynamics: Coil-stretch transition in a random flow. *EPL (Europhysics Letters)*, 71(2):221, 2005.

[72] Nicolas François, David Lasne, Yacine Amarouchene, Brahim Lounis, and Hamid Kellay. Drag enhancement with polymers. *Physical review letters*, 100(1):018302, 2008.

[73] Nicolas François, Yacine Amarouchene, Brahim Lounis, and Hamid Kellay. Polymer conformations and hysteretic stresses in nonstationary flows of polymer solutions. *EPL (Europhysics Letters)*, 86(3):34002, 2009.

[74] Lea Rems, Durgesh Kawale, L James Lee, and Pouyan E Boukany. Flow of dna in micro/nanofluidics: From fundamentals to applications. *Biomicrofluidics*, 10(4): 043403, 2016.

[75] Charles M Schroeder. Single polymer dynamics for molecular rheology. *Journal of Rheology*, 62(1):371–403, 2018.

[76] Peyman Pakdel and Gareth H McKinley. Elastic instability and curved streamlines. *Physical Review Letters*, 77(12):2459, 1996.

[77] Gareth H McKinley, Peyman Pakdel, and Alparslan Öztekin. Rheological and geometric scaling of purely elastic flow instabilities. *Journal of Non-Newtonian Fluid Mechanics*, 67:19–47, 1996.

[78] J Zilz, RJ Poole, MA Alves, D Bartolo, B Levaché, and A Lindner. Geometric scaling of a purely elastic flow instability in serpentine channels. *Journal of Fluid Mechanics*, 712:203–218, 2012.

[79] Simon J. Haward, Gareth H. McKinley, and Amy Q. Shen. Elastic instabilities in planar elongational flow of monodisperse polymer solutions. *Scientific Reports*, 6: 33029, 2016.

[80] Alexander Groisman and Victor Steinberg. Elastic turbulence in a polymer solution flow. *Nature*, 405(6782):53–55, 2000.

[81] JRA Pearson. Instability in non-newtonian flow. *Annual Review of Fluid Mechanics*, 8(1):163–181, 1976.

[82] RG Larson. Flow-induced mixing, demixing, and phase transitions in polymeric fluids. *Rheologica Acta*, 31(6):497–520, 1992.

[83] Francisco J Galindo-Rosales, Laura Campo-Deaño, Patrícia C Sousa, Vera M Ribeiro, Mónica SN Oliveira, Manuel A Alves, and Fernando T Pinho. Viscoelastic instabilities in micro-scale flows. *Experimental Thermal and Fluid Science*, 59: 128–139, 2014.

[84] PC Sousa, FT Pinho, MSN Oliveira, and MA Alves. Purely elastic flow instabilities in microscale cross-slot devices. *Soft matter*, 11(45):8856–8862, 2015.

[85] B. Qin and P. E. Arratia. Characterizing elastic turbulence in channel flows at low Reynolds number. *Physical Review Fluids*, 2(8):083302, 2017.

[86] Ann Muggeridge, Andrew Cockin, Kevin Webb, Harry Frampton, Ian Collins, Tim Moulds, and Peter Salino. Recovery rates, enhanced oil recovery and technological limits. *Philosophical Transactions of the Royal Society A: Mathematical, Physical and Engineering Sciences*, 372(2006):20120320, 2014.

[87] KW Koelling and Robert Krafft Prud'homme. Instabilities in multi-hole converging flow of viscoelastic fluids. *Rheologica acta*, 30(6):511–522, 1991.

[88] Alfredo Lanzaro and Xue-Feng Yuan. Effects of contraction ratio on non-linear dynamics of semi-dilute, highly polydisperse PAAm solutions in microfluidics. *Journal of Non-Newtonian Fluid Mechanics*, 166(17-18):1064–1075, 2011.

[89] Stephen Kenney, Kade Poper, Ganesh Chapagain, and Gordon F Christopher. Large deborah number flows around confined microfluidic cylinders. *Rheologica Acta*, 52(5):485–497, 2013.

[90] VM Ribeiro, PM Coelho, FT Pinho, and MA Alves. Viscoelastic fluid flow past a confined cylinder: Three-dimensional effects and stability. *Chemical Engineering Science*, 111:364–380, 2014.

[91] Alfredo Lanzaro, Zhuo Li, and Xue-Feng Yuan. Quantitative characterization of high molecular weight polymer solutions in microfluidic hyperbolic contraction flow. *Microfluidics and Nanofluidics*, 18(5-6):819–828, 2015.

[92] Shelly Gulati, Susan J Muller, and Dorian Liepmann. Flow of dna solutions in a microfluidic gradual contraction. *Biomicrofluidics*, 9(5):054102, 2015.

[93] Xueda Shi, Stephen Kenney, Ganesh Chapagain, and Gordon F Christopher. Mechanisms of onset for moderate mach number instabilities of viscoelastic flows around confined cylinders. *Rheologica Acta*, 54(9-10):805–815, 2015.

[94] Xueda Shi and Gordon F Christopher. Growth of viscoelastic instabilities around linear cylinder arrays. *Physics of Fluids*, 28(12):124102, 2016.

[95] Alfredo Lanzaro, Daniel Corbett, and Xue-Feng Yuan. Non-linear dynamics of semi-dilute PAAm solutions in a microfluidic 3d cross-slot flow geometry. *Journal of Non-Newtonian Fluid Mechanics*, 242:57–65, 2017.

[96] Simon J Haward, Kazumi Toda-Peters, and Amy Q Shen. Steady viscoelastic flow around high-aspect-ratio, low-blockage-ratio microfluidic cylinders. *Journal of Non-Newtonian Fluid Mechanics*, 254:23–35, 2018.

[97] Boyang Qin, Paul F. Salipante, Steven D. Hudson, and Paulo E. Arratia. Upstream vortex and elastic wave in the viscoelastic flow around a confined cylinder. *Journal of Fluid Mechanics*, 864:R2, 2019. doi: 10.1017/jfm.2019.73.

[98] Manish Kumar, Jeffrey S Guasto, and Arezoo M Ardekani. Transport of complex and active fluids in porous media. *Journal of Rheology*, 66(2):375–397, 2022.

[99] Alfredo Lanzaro. *Microscopic flows of aqueous polyacrylamide solutions: a quantitative study*. PhD thesis, The University of Manchester (United Kingdom), 2011.

[100] Alfredo Lanzaro and Xue-Feng Yuan. A quantitative analysis of spatial extensional rate distribution in nonlinear viscoelastic flows. *Journal of Non-Newtonian Fluid Mechanics*, 207:32–41, 2014.

[101] Peter Szabo, JM Rallison, and EJ Hinch. Start-up of flow of a fene-fluid through a 4: 1: 4 constriction in a tube. *Journal of non-newtonian fluid mechanics*, 72(1):73–86, 1997.

[102] Lucy E Rodd, Timothy P Scott, David V Boger, Justin J Cooper-White, and Gareth H McKinley. The inertio-elastic planar entry flow of low-viscosity elastic fluids in micro-fabricated geometries. *Journal of Non-Newtonian Fluid Mechanics*, 129(1):1–22, 2005.

[103] Barnin Khomami and Luis D Moreno. Stability of viscoelastic flow around periodic arrays of cylinders. *Rheologica acta*, 36(4):367–383, 1997.

[104] K Arora, R Sureshkumar, and B Khomami. Experimental investigation of purely elastic instabilities in periodic flows. *Journal of non-newtonian fluid mechanics*, 108 (1-3):209–226, 2002.

[105] Francisco J Galindo-Rosales, Laura Campo-Deaño, FT Pinho, E Van Bokhorst, PJ Hamersma, Mónica SN Oliveira, and MA Alves. Microfluidic systems for the analysis of viscoelastic fluid flow phenomena in porous media. *Microfluidics and Nanofluidics*, 12(1-4):485–498, 2012.

[106] Atul Varshney and Victor Steinberg. Elastic wake instabilities in a creeping flow between two obstacles. *Physical Review Fluids*, 2(5):051301, 2017.

[107] Manish Kumar and Arezoo M Ardekani. Elastic instabilities between two cylinders confined in a channel. *Physics of Fluids*, 33(7):074107, 2021.

[108] Andrew M Howe, Andrew Clarke, and Daniel Giernalczyk. Flow of concentrated viscoelastic polymer solutions in porous media: effect of mw and concentration on elastic turbulence onset in various geometries. *Soft Matter*, 11(32):6419–6431, 2015.

[109] Durgesh Kawale, Gelmer Bouwman, Shaurya Sachdev, Pacelli LJ Zitha, Michiel T Kreutzer, William R Rossen, and Pouyan E Boukany. Polymer conformation during flow in porous media. *Soft Matter*, 13(46):8745–8755, 2017.

[110] Durgesh Kawale, Jishnu Jayaraman, and Pouyan E Boukany. Microfluidic rectifier for polymer solutions flowing through porous media. *Biomicrofluidics*, 13(1): 014111, 2019.

[111] Durgesh Kawale, Esteban Marques, Pacelli LJ Zitha, Michiel T Kreutzer, William R Rossen, and Pouyan E Boukany. Elastic instabilities during the flow of hydrolyzed polyacrylamide solution in porous media: Effect of pore-shape and salt. *Soft Matter*, 13(4):765–775, 2017.

[112] Kapil K Talwar and Bamin Khomami. Flow of viscoelastic fluids past periodic square arrays of cylinders: inertial and shear thinning viscosity and elasticity effects. *Journal of Non-Newtonian Fluid Mechanics*, 57(2-3):177–202, 1995.

[113] S De, J Van Der Schaaf, Niels G Deen, JAM Kuipers, EAJF Peters, and JT Padding. Lane change in flows through pillared microchannels. *Physics of Fluids*, 29(11): 113102, 2017.

[114] S De, P Krishnan, J van der Schaaf, JAM Kuipers, EAJF Peters, and JT Padding. Viscoelastic effects on residual oil distribution in flows through pillared microchannels. *Journal of colloid and interface science*, 510:262–271, 2018.

[115] B Sadanandan and Radhakrishna Sureshkumar. Global linear stability analysis of viscoelastic flow through a periodic channel. *Journal of non-newtonian fluid mechanics*, 122(1-3):55–67, 2004.

[116] S De, S Das, JAM Kuipers, EAJF Peters, and JT Padding. A coupled finite volume immersed boundary method for simulating 3d viscoelastic flows in complex geometries. *Journal of Non-Newtonian Fluid Mechanics*, 232:67–76, 2016.

[117] S De, JAM Kuipers, EAJF Peters, and JT Padding. Viscoelastic flow simulations in model porous media. *Physical Review Fluids*, 2(5):053303, 2017.

[118] A Vázquez-Quesada and M Ellero. Sph simulations of a viscoelastic flow around a periodic array of cylinders confined in a channel. *Journal of Non-Newtonian Fluid Mechanics*, 167:1–8, 2012.

[119] Shauvik De, JAM Kuipers, EAJF Peters, and JT Padding. Viscoelastic flow simulations in random porous media. *Journal of Non-Newtonian Fluid Mechanics*, 248: 50–61, 2017.

[120] Simon J. Haward, Cameron C. Hopkins, and Amy Q. Shen. Stagnation points control chaotic fluctuations in viscoelastic porous media flow. *Proceedings of the National Academy of Sciences*, 118(38), 2021.

[121] Stephen B Pope. *Turbulent flows*. Cambridge University Press, 2000.

[122] Andreas Hartmann, Scott Jasechko, Tom Gleeson, Yoshihide Wada, Bartolomé Andreo, Juan Antonio Barberá, Heike Brielmann, Lhoussaine Bouchaou, Jean-Baptiste Charlier, W George Darling, et al. Risk of groundwater contamination widely underestimated because of fast flow into aquifers. *Proceedings of the National Academy of Sciences*, 118(20), 2021.

[123] FRBU Durst, R Haas, and BU Kaczmar. Flows of dilute hydrolyzed polyacrylamide solutions in porous media under various solvent conditions. *Journal of Applied Polymer Science*, 26(9):3125–3149, 1981.

[124] Mariaines Di Dato, Claudia D'Angelo, Alessandro Casasso, and Antonio Zarlenga. The impact of porous medium heterogeneity on the thermal feedback of open-loop shallow geothermal systems. *Journal of Hydrology*, page 127205, 2021.

[125] Philippe M. Doyen. Permeability, Conductivity, and Pore Geometry of Sandstone. *Journal of Geophysical Research*, 93(B7):7729–7740, 1988.

[126] M. J. Kwiecien, I. F. Macdonald, and F. A.L. Dullien. Three-dimensional reconstruction of porous media from serial section data. *Journal of Microscopy*, 159(3): 343–359, sep 1990. ISSN 13652818. doi: 10.1111/j.1365-2818.1990.tb03039.x. URL http://doi.wiley.com/10.1111/j.1365-2818.1990.tb03039.x.

[127] Y. Bernabe. Pore geometry and pressure dependence of the transport properties in sandstones. *Geophysics*, 56(4):424–576, 1991.

[128] Marios A. Ioannidis and Ioannis Chatzis. Network modelling of pore structure and transport properties of porous media. *Chemical Engineering Science*, 48(5):951–972, 1993.

[129] James P Harnett and Thomas F Irvine. *Advances in heat transfer*. Elsevier Science, 1979.

[130] Younggon Son. Determination of shear viscosity and shear rate from pressure drop and flow rate relationship in a rectangular channel. *Polymer*, 48(2):632–637, 2007.

[131] M. Grilli, A. Vázquez-Quesada, and M. Ellero. Transition to turbulence and mixing in a viscoelastic fluid flowing inside a channel with a periodic array of cylindrical obstacles. *Phys. Rev. Lett.*, 110(17):174501, 2013.

[132] R Sureshkumar, Antony N Beris, and Robert A Handler. Direct numerical simulation of the turbulent channel flow of a polymer solution. *Physics of Fluids*, 9(3): 743–755, 1997.

[133] E Balkovsky, A Fouxon, and V Lebedev. Turbulent dynamics of polymer solutions. *Physical review letters*, 84(20):4765, 2000.

[134] Michael Chertkov. Polymer stretching by turbulence. *Physical review letters*, 84(20): 4761, 2000.

[135] VK Gupta, R Sureshkumar, and B Khomami. Polymer chain dynamics in newtonian and viscoelastic turbulent channel flows. *Physics of Fluids*, 16(5):1546–1566, 2004.

[136] VE Terrapon, Yves Dubief, Parviz Moin, Eric SG Shaqfeh, and Sanjiva K Lele. Simulated polymer stretch in a turbulent flow using brownian dynamics. *Journal of Fluid Mechanics*, 504:61–71, 2004.

[137] Frédéric Zami-Pierre, R De Loubens, Michel Quintard, and Yohan Davit. Transition in the flow of power-law fluids through isotropic porous media. *Physical Review Letters*, 117(7):074502, 2016.

[138] Marios Avgousti and Antony N Beris. Non-axisymmetric modes in viscoelastic taylor-couette flow. *Journal of non-newtonian fluid mechanics*, 50(2-3):225–251, 1993.

[139] Radhakrishna Sureshkumar, Antony N Beris, and Marios Avgousti. Non-axisymmetric subcritical bifurcations in viscoelastic taylor–couette flow. *Proceedings of the Royal Society of London. Series A: Mathematical and Physical Sciences*, 447 (1929):135–153, 1994.

[140] Stergios Pilitsis and Antony N Beris. Calculations of steady-state viscoelastic flow in an undulating tube. *Journal of Non-Newtonian Fluid Mechanics*, 31(3):231–287, 1989.

[141] Stergios Pilitsis and Antony N Beris. Viscoelastic flow in an undulating tube. part ii. effects of high elasticity, large amplitude of undulation and inertia. *Journal of non-newtonian fluid mechanics*, 39(3):375–405, 1991.

[142] Christian Clasen, JP Plog, W-M Kulicke, M Owens, Chris Macosko, LE Scriven, M Verani, and Gareth H McKinley. How dilute are dilute solutions in extensional flows? *Journal of Rheology*, 50(6):849–881, 2006.

[143] Md Zulfikar Ali, Ned S Wingreen, and Ranjan Mukhopadhyay. Hidden long evolutionary memory in a model biochemical network. *Physical Review E*, 97(4):040401, 2018.

[144] S De, SP Koesen, RV Maitri, M Golombok, JT Padding, and JFM van Santvoort. Flow of viscoelastic surfactants through porous media. *AIChE Journal*, 64(2):773–781, 2018.

[145] Firoozeh Babayekhorasani, Dave E Dunstan, Ramanan Krishnamoorti, and Jacinta C Conrad. Nanoparticle dispersion in disordered porous media with and without polymer additives. *Soft Matter*, 12(26):5676–5683, 2016.

[146] Soroush Aramideh, Pavlos P Vlachos, and Arezoo M Ardekani. Nanoparticle dispersion in porous media in viscoelastic polymer solutions. *Journal of Non-Newtonian Fluid Mechanics*, 268:75–80, 2019.

[147] Alain Bourgeat, Olivier Gipouloux, and Eduard Marusic-Paloka. Filtration law for polymer flow through porous media. *Multiscale Modeling & Simulation*, 1(3): 432–457, 2003.

[148] Min Luo and Iwao Teraoka. High osmotic pressure chromatography for large-scale fractionation of polymers. *Macromolecules*, 29(12):4226–4233, 1996.

[149] David F James and DR McLaren. The laminar flow of dilute polymer solutions through porous media. *Journal of Fluid Mechanics*, 70(4):733–752, 1975.

[150] FRBU Durst and R Haas. Dehnstromungen mit verdunnten polymerlosungen: Ein theoretisches modell und seine experimentelle verifikations. *Rheol. Acta*, 20: 179–192, 1981.

[151] N Kauser, L Dos Santos, M Delgado, AJ Muller, and AE Saez. Flow of mixtures of poly(ethylene oxide) and hydrolyzed polyacrylamide solutions through porous media. *Journal of applied polymer science*, 72:783–795, 1999.

[152] Teodor Burghelea, Enrico Segre, Israel Bar-Joseph, Alex Groisman, and Victor Steinberg. Chaotic flow and efficient mixing in a microchannel with a polymer solution. *Physical Review E*, 69(6):066305, 2004.

[153] Anaïs Machado, Hugues Bodiguel, Julien Beaumont, Gérald Clisson, and Annie Colin. Extra dissipation and flow uniformization due to elastic instabilities of shear-thinning polymer solutions in model porous media. *Biomicrofluidics*, 10(4):043507, 2016.

[154] Boyang Qin, Paul F Salipante, Steven D Hudson, and Paulo E Arratia. Flow resistance and structures in viscoelastic channel flows at low Re. *Physical Review Letters*, 123(19):194501, 2019.

[155] R. G. Larson, E. S. G. Shaqfeh, and S. J. Muller. A purely elastic instability in Taylor–Couette flow. *J. Fluid Mech.*, 218:573–600, 1990.

[156] Eric SG Shaqfeh. Purely elastic instabilities in viscometric flows. *Annual Review of Fluid Mechanics*, 28:129–185, 1996.

[157] AM Afonso, MA Alves, and FT Pinho. Purely elastic instabilities in three-dimensional cross-slot geometries. *Journal of Non-Newtonian Fluid Mechanics*, 165(13-14):743–751, 2010.

[158] PC Sousa, FT Pinho, and MA Alves. Purely-elastic flow instabilities and elastic turbulence in microfluidic cross-slot devices. *Soft Matter*, 14(8):1344–1354, 2018.

[159] Martin J Blunt. *Multiphase flow in permeable media: A pore-scale perspective*. Cambridge University Press, 2017.

[160] Steffen Berg and John van Wunnik. Shear rate determination from pore-scale flow fields. *Transport in Porous Media*, 117(2):229–246, 2017.

[161] Narsing K Jha and Victor Steinberg. Universal coherent structures of elastic turbulence in straight channel with viscoelastic fluid flow. *arXiv preprint arXiv:2009.12258*, 2020.

[162] A. Groisman and V. Steinberg. Elastic turbulence in curvilinear flows of polymer solutions. *New J. Phys.*, 6(1):29, 2004.

[163] Alexander Groisman and Victor Steinberg. Elastic turbulence in curvilinear flows of polymer solutions. *New Journal of Physics*, 6(1):29, 2004.

[164] R van Buel, C Schaaf, and H Stark. Elastic turbulence in two-dimensional Taylor-Couette flows. *Europhysics Letters*, 124(1):14001, 2018.

[165] Reinier van Buel and Holger Stark. Active open-loop control of elastic turbulence. *Scientific reports*, 10(1):1–9, 2020.

[166] Grégoire Lemoult, Liang Shi, Kerstin Avila, Shreyas V Jalikop, Marc Avila, and Björn Hof. Directed percolation phase transition to sustained turbulence in couette flow. *Nature Physics*, 12(3):254–258, 2016.

[167] C Letellier. Intermittency as a transition to turbulence in pipes: the long tradition from reynolds to the 21st century. *Mechanical Reports*, 345(9):642–659, 2017.

[168] Dwight Barkley. Theoretical perspective on the route to turbulence in a pipe. *Journal of Fluid Mechanics*, 803:1–80, 2016.

[169] PG De Gennes. Molecular individualism. *Science*, 276(5321):1999–2000, 1997.

[170] Stephen Whitaker. *Introduction to Fluid Mechanics*. Krieger Pub Co, 1992.

[171] Gareth H McKinley and Tamarapu Sridhar. Filament-stretching rheometry of complex fluids. *Annual Review of Fluid Mechanics*, 34(1):375–415, 2002.

[172] Angélique Delafosse, Marie-Laure Collignon, Michel Crine, and Dominique Toye. Estimation of the turbulent kinetic energy dissipation rate from 2d-piv measurements in a vessel stirred by an axial mixel ttp impeller. *Chemical Engineering Science*, 66(8):1728–1737, 2011.

[173] Kendra V Sharp, Kyung Chun Kim, and R Adrian. Dissipation estimation around a rushton turbine using particle image velocimetry. In *Laser Techniques Applied to Fluid Mechanics*, pages 337–354. Springer, 2000.

[174] Li Xi and Michael D Graham. Intermittent dynamics of turbulence hibernation in Newtonian and viscoelastic minimal channel flows. *Journal of Fluid Mechanics*, 693:433, 2012.

[175] Christian Scholz, Frank Wirner, Juan Ruben Gomez-Solano, and Clemens Bechinger. Enhanced dispersion by elastic turbulence in porous media. *EPL (Europhysics Letters)*, 107(5):54003, 2014.

[176] Phil Ligrani, Daniel Copeland, Chong Ren, Mengying Su, and Masaaki Suzuki. Heat transfer enhancements from elastic turbulence using sucrose-based polymer solutions. *Journal of Thermophysics and Heat Transfer*, 32(1):51–60, 2018.

[177] Xin Wang, Man Jiang, Zuowan Zhou, Jihua Gou, and David Hui. 3d printing of polymer matrix composites: A review and prospective. *Composites Part B: Engineering*, 110:442–458, 2017.

[178] R Allan Freeze. A stochastic-conceptual analysis of one-dimensional groundwater flow in nonuniform homogeneous media. *Water resources research*, 11(5):725–741, 1975.

[179] Gedeon Dagan. *Flow and transport in porous formations*. Springer Science & Business Media, 2012.

[180] Larry W Lake and George J Hirasaki. Taylor's dispersion in stratified porous media. *Society of Petroleum Engineers Journal*, 21(04):459–468, 1981.

[181] Victor C Ibezim, Robert J Poole, and David JC Dennis. Viscoelastic fluid flow in microporous media. *Journal of Non-Newtonian Fluid Mechanics*, 296:104638, 2021.

[182] George Y Onoda and Eric G Liniger. Random loose packings of uniform spheres and the dilatancy onset. *Physical review letters*, 64(22):2727, 1990.

[183] Amber T Krummel, Sujit S Datta, Stefan Münster, and David A Weitz. Visualizing multiphase flow and trapped fluid configurations in a model three-dimensional porous medium. *AIChE Journal*, 59(3):1022–1029, 2013.

[184] Sujit S Datta and David A Weitz. Drainage in a model stratified porous medium. *EPL (Europhysics Letters)*, 101(1):14002, 2013.

[185] Albert P Philipse and Chellappah Pathmamanoharan. Liquid permeation (and sedimentation) of dense colloidal hard-sphere packings. *Journal of Colloid and Interface Science*, 159(1):96–107, 1993.

[186] William Thielicke and Eize Stamhuis. Pivlab–towards user-friendly, affordable and accurate digital particle image velocimetry in matlab. *Journal of Open Research Software*, 2(1):e30, 2014. doi: http://doi.org/10.5334/jors.bl.

[187] TK Perkins and OCt Johnston. A review of diffusion and dispersion in porous media. *Society of Petroleum Engineers Journal*, 3(01):70–84, 1963.

[188] Andrew W Woods. *Flow in porous rocks*. Cambridge University Press, 2015.

[189] Shi-Qing Wang, S Ravindranath, and PE Boukany. Homogeneous shear, wall slip, and shear banding of entangled polymeric liquids in simple-shear rheometry: A roadmap of nonlinear rheology. *Macromolecules*, 44(2):183–190, 2011.

[190] Suzanne M Fielding. Complex dynamics of shear banded flows. *Soft Matter*, 3(10): 1262–1279, 2007.

[191] Peter D Olmsted. Perspectives on shear banding in complex fluids. *Rheologica Acta*, 47(3):283–300, 2008.

[192] Koichi Saito, Mazakazu Horie, Norihide Nose, Kazuya Nakagomi, and Hiroyuki Nakazawa. High-performance liquid chromatography of histamine and 1-methylhistamine with on-column fluroescence derivatization. *Journal of Chromatography A*, 595(1-2):163–168, 1992.

[193] O Trapp. Unified equation for access to rate constants of first-order reactions in dynamic and on-column reaction chromatography. *Analytical chemistry*, 78(1): 189–198, 2006.

[194] Kazunori Saitoh, Kohta Koichi, Fumiko Yabiku, Yumiko Noda, Marc D Porter, and Masami Shibukawa. On-column electrochemical redox derivatization for enhancement of separation selectivity of liquid chromatography: Use of redox reaction as secondary chemical equilibrium. *Journal of Chromatography A*, 1180(1-2):66–72, 2008.

[195] Sameer K Ajmera, Matthew W Losey, Klavs F Jensen, and Martin A Schmidt. Microfabricated packed-bed reactor for phosgene synthesis. *AIChE Journal*, 47(7): 1639–1647, 2001.

[196] Florian Meirer and Bert M Weckhuysen. Spatial and temporal exploration of heterogeneous catalysts with synchrotron radiation. *Nature Reviews Materials*, 3(9): 324–340, 2018.

[197] Sarkyt E Kudaibergenov and Gulzhian I Dzhardimalieva. Flow-through catalytic reactors based on metal nanoparticles immobilized within porous polymeric gels and surfaces/hollows of polymeric membranes. *Polymers*, 12(3):572, 2020.

[198] Marek Trojanowicz. Flow chemistry in contemporary chemical sciences: A real variety of its applications. *Molecules*, 25(6):1434, 2020.

[199] Samuel Marre and Klavs F Jensen. Synthesis of micro and nanostructures in microfluidic systems. *Chemical Society Reviews*, 39(3):1183–1202, 2010.

[200] JP Maree and Wilma F Strydom. Biological sulphate removal in an upflow packed bed reactor. *Water Research*, 19(9):1101–1106, 1985.

[201] JP Maree and Wilma F Strydom. Biological sulphate removal from industrial effluent in an upflow packed bed reactor. *Water Research*, 21(2):141–146, 1987.

[202] CLK Tennakoon, RC Bhardwaji, and JO'M Bockris. Electrochemical treatment of human wastes in a packed bed reactor. *Journal of applied electrochemistry*, 26(1): 18–29, 1996.

[203] Sander Noorman, Martin van Sint Annaland, and Hans Kuipers. Packed bed reactor technology for chemical-looping combustion. *Industrial & Engineering Chemistry Research*, 46(12):4212–4220, 2007.

[204] Emily J Anglin, Lingyun Cheng, William R Freeman, and Michael J Sailor. Porous silicon in drug delivery devices and materials. *Advanced drug delivery reviews*, 60 (11):1266–1277, 2008.

[205] S Datta, B Mailloux, H-B Jung, MA Hoque, M Stute, KM Ahmed, and Y Zheng. Redox trapping of arsenic during groundwater discharge in sediments from the meghna riverbank in bangladesh. *Proceedings of the National Academy of Sciences*, 106(40):16930–16935, 2009.

[206] Peter K Kitanidis and Perry L McCarty. *Delivery and Mixing in the Subsurface: Processes and Design Principles for in Situ remediation*, volume 4. Springer Science & Business Media, 2012.

[207] Michael L Szulczewski, Christopher W MacMinn, Howard J Herzog, and Ruben Juanes. Lifetime of carbon capture and storage as a climate-change mitigation technology. *Proceedings of the National Academy of Sciences*, 109(14):5185–5189, 2012.

[208] Knut Drescher, Yi Shen, Bonnie L Bassler, and Howard A Stone. Biofilm streamers cause catastrophic disruption of flow with consequences for environmental and medical systems. *Proceedings of the National Academy of Sciences*, 110(11):4345–4350, 2013.

[209] Jesus D Gomez-Velez, Judson W Harvey, M Bayani Cardenas, and Brian Kiel. Denitrification in the mississippi river network controlled by flow through river bedforms. *Nature Geoscience*, 8(12):941–945, 2015.

[210] Juerg M Matter, Martin Stute, Sandra Ó Snæbjörnsdottir, Eric H Oelkers, Sigurdur R Gislason, Edda S Aradottir, Bergur Sigfusson, Ingvi Gunnarsson, Holmfridur Sigurdardottir, Einar Gunnlaugsson, et al. Rapid carbon mineralization for permanent disposal of anthropogenic carbon dioxide emissions. *Science*, 352(6291):1312–1314, 2016.

[211] James C Stegen, James K Fredrickson, Michael J Wilkins, Allan E Konopka, William C Nelson, Evan V Arntzen, William B Chrisler, Rosalie K Chu, Robert E Danczak, Sarah J Fansler, et al. Groundwater–surface water mixing shifts ecological assembly processes and stimulates organic carbon turnover. *Nature communications*, 7(1):1–12, 2016.

[212] Benedict Borer, Robin Tecon, and Dani Or. Spatial organization of bacterial populations in response to oxygen and carbon counter-gradients in pore networks. *Nature communications*, 9(1):1–11, 2018.

[213] Olivier Bochet, Lorine Bethencourt, Alexis Dufresne, Julien Farasin, Mathieu Pédrot, Thierry Labasque, Eliot Chatton, Nicolas Lavenant, Christophe Petton, Benjamin W Abbott, et al. Iron-oxidizer hotspots formed by intermittent oxic–anoxic fluid mixing in fractured rocks. *Nature Geoscience*, 13(2):149–155, 2020.

[214] William A Braff, Martin Z Bazant, and Cullen R Buie. Membrane-less hydrogen bromine flow battery. *Nature communications*, 4(1):1–6, 2013.

[215] Stephen G Newman and Klavs F Jensen. The role of flow in green chemistry and engineering. *Green chemistry*, 15(6):1456–1472, 2013.

[216] Klavs F Jensen. Flow chemistry—microreaction technology comes of age. *AIChE Journal*, 63(3):858–869, 2017.

[217] Luigi Vaccaro. *Sustainable flow chemistry: methods and applications*. John Wiley & Sons, 2017.

[218] Abraham D Stroock, Stephan KW Dertinger, Armand Ajdari, Igor Mezić, Howard A Stone, and George M Whitesides. Chaotic mixer for microchannels. *Science*, 295(5555):647–651, 2002.

[219] Klavs F Jensen. Microreaction engineering—is small better? *Chemical Engineering Science*, 56(2):293–303, 2001.

[220] C Heath Turner, J Karl Johnson, and Keith E Gubbins. Effect of confinement on chemical reaction equilibria: The reactions 2no<->(no) 2 and n 2+ 3h 2<->2nh 3 in carbon micropores. *The Journal of Chemical Physics*, 114(4):1851–1859, 2001.

[221] C Heath Turner, John K Brennan, J Karl Johnson, and Keith E Gubbins. Effect of confinement by porous materials on chemical reaction kinetics. *The Journal of chemical physics*, 116(5):2138–2148, 2002.

[222] Shuo Zhang, Meng Sun, Tayler Hedtke, Akshay Deshmukh, Xuechen Zhou, Seunghyun Weon, Menachem Elimelech, and Jae-Hong Kim. Mechanism of heterogeneous fenton reaction kinetics enhancement under nanoscale spatial confinement. *Environmental Science & Technology*, 54(17):10868–10875, 2020.

[223] Helen Song, Michelle R Bringer, Joshua D Tice, Cory J Gerdts, and Rustem F Ismagilov. Experimental test of scaling of mixing by chaotic advection in droplets moving through microfluidic channels. *Applied physics letters*, 83(22):4664–4666, 2003.

[224] Helen Song and Rustem F Ismagilov. Millisecond kinetics on a microfluidic chip using nanoliters of reagents. *Journal of the American Chemical Society*, 125(47): 14613–14619, 2003.

[225] Shia-Yen Teh, Robert Lin, Lung-Hsin Hung, and Abraham P Lee. Droplet microfluidics. *Lab on a Chip*, 8(2):198–220, 2008.

[226] Xavier Casadevall i Solvas and Andrew DeMello. Droplet microfluidics: recent developments and future applications. *Chemical Communications*, 47(7):1936–1942, 2011.

[227] Mira T Guo, Assaf Rotem, John A Heyman, and David A Weitz. Droplet microfluidics for high-throughput biological assays. *Lab on a Chip*, 12(12):2146–2155, 2012.

[228] Luoran Shang, Yao Cheng, and Yuanjin Zhao. Emerging droplet microfluidics. *Chemical reviews*, 117(12):7964–8040, 2017.

[229] Sujit S Datta, Arezoo M Ardekani, Paulo E Arratia, Antony N Beris, Irmgard Bischofberger, Jens G Eggers, J Esteban López-Aguilar, Suzanne M Fielding, Anna Frishman, Michael D Graham, et al. Perspectives on viscoelastic flow instabilities and elastic turbulence. *arXiv preprint arXiv:2108.09841; under review in Physical Review Fluids*, 2021.

[230] J Bałdyga and R Pohorecki. Turbulent micromixing in chemical reactors—a review. *The Chemical Engineering Journal and the Biochemical Engineering Journal*, 58(2):183–195, 1995.

[231] James C Hill. Homogeneous turbulent mixing with chemical reaction. *Annual review of fluid Mechanics*, 8(1):135–161, 1976.

[232] Paul E Dimotakis. Turbulent mixing. *Annu. Rev. Fluid Mech.*, 37:329–356, 2005.

[233] Andrey Nikolaevich Kolmogorov. Cr (doklady) acad. *Sci. URSS (NS)*, 30:301–305, 1941.

[234] Michio Yamada and Koji Ohkitani. Lyapunov spectrum of a chaotic model of three-dimensional turbulence. *Journal of the Physical Society of Japan*, 56(12):4210–4213, 1987.

[235] Erik Aurell, Guido Boffetta, Andrea Crisanti, Giovanni Paladin, and Angelo Vulpiani. Growth of noninfinitesimal perturbations in turbulence. *Physical review letters*, 77(7):1262, 1996.

[236] Prakash Mohan, Nicholas Fitzsimmons, and Robert D Moser. Scaling of lyapunov exponents in homogeneous isotropic turbulence. *Physical Review Fluids*, 2(11):114606, 2017.

[237] DR Fereday, PH Haynes, A Wonhas, and JC Vassilicos. Scalar variance decay in chaotic advection and batchelor-regime turbulence. *Physical Review E*, 65(3): 035301, 2002.

[238] B. Thomases and M. Shelley. Transition to mixing and oscillations in a Stokesian viscoelastic flow. *Phys. Rev. Lett.*, 103(9):094501, 2009.

[239] B. Thomases, M. Shelley, and J.-L. Thiffeault. A stokesian viscoelastic flow: transition to oscillations and mixing. *Physica D*, 240(20):1602–1614, 2011.

[240] A. Groisman and V. Steinberg. Efficient mixing at low reynolds numbers using polymer additives. *Nature*, 410(6831):905–908, 2001.

[241] T Burghelea, Enrico Segre, and Victor Steinberg. Statistics of particle pair separations in the elastic turbulent flow of a dilute polymer solution. *EPL (Europhysics Letters)*, 68(4):529, 2004.

[242] Claire Simonnet and Alex Groisman. Chaotic mixing in a steady flow in a microchannel. *Physical review letters*, 94(13):134501, 2005.

[243] Boubou Traore, Cathy Castelain, and Teodor Burghelea. Efficient heat transfer in a regime of elastic turbulence. *Journal of Non-Newtonian Fluid Mechanics*, 223: 62–76, 2015.

[244] T Burghelea, Enrico Segre, and Victor Steinberg. Validity of the taylor hypothesis in a random spatially smooth flow. *Physics of Fluids*, 17(10):103101, 2005.

[245] Teodor Burghelea, Enrico Segre, and Victor Steinberg. Role of elastic stress in statistical and scaling properties of elastic turbulence. *Physical review letters*, 96(21): 214502, 2006.

[246] T Burghelea, E Segre, and V Steinberg. Mixing by polymers: Experimental test of decay regime of mixing. *Phys. Rev. Lett.*, 92(16):164501, 2004.

[247] S. Kumar and G.M. Homsy. Chaotic advection in creeping flow of viscoelastic fluids between slowly modulated eccentric cylinders. *Phys. Fluids*, 8(7):1774–1787, 1996.

[248] Y. Jun and V. Steinberg. Polymer concentration and properties of elastic turbulence in a von Karman swirling flow. *Phys. Rev. Fluids*, 2(10):103301, 2017.

[249] TC Niederkorn and Julio M Ottino. Mixing of a viscoelastic fluid in a time-periodic flow. *J. Fluid Mech.*, 256:243–268, 1993.

[250] P. E. Arratia, C. C. Thomas, J. Diorio, and J. P. Gollub. Elastic instabilities of polymer solutions in cross-channel flow. *Phys. Rev. Lett.*, 96(14):144502, 2006.

[251] Teodor Burghelea, Enrico Segre, and Victor Steinberg. Elastic turbulence in von karman swirling flow between two disks. *Phys. Fluids*, 19(5):053104, 2007.

[252] Waleed M Abed, Richard D Whalley, David JC Dennis, and Robert J Poole. Experimental investigation of the impact of elastic turbulence on heat transfer in a serpentine channel. *Journal of Non-Newtonian Fluid Mechanics*, 231:68–78, 2016.

[253] RD Whalley, WM Abed, DJC Dennis, and RJ Poole. Enhancing heat transfer at the micro-scale using elastic turbulence. *Theoretical and Applied Mechanics Letters*, 5 (3):103–106, 2015.

[254] D.-Y. Li, X.-B. Li, H.-N. Zhang, F.-C. Li, S. Qian, and S. W. Joo. Efficient heat transfer enhancement by elastic turbulence with polymer solution in a curved microchannel. *Microfluid. Nanofluid.*, 21(1):10, 2017.

[255] Haie Yang, Guice Yao, and Dongsheng Wen. Efficient mixing enhancement by orthogonal injection of shear-thinning fluids in a micro serpentine channel at low reynolds numbers. *Chemical Engineering Science*, 235:116368, 2021.

[256] Michael Chertkov and Vladimir Lebedev. Decay of scalar turbulence revisited. *Physical review letters*, 90(3):034501, 2003.

[257] Yonggun Jun and Victor Steinberg. Mixing of passive tracers in the decay batchelor regime of a channel flow. *Physics of Fluids*, 22(12):123101, 2010.

[258] Emmanuel Villermaux. Mixing by porous media. *Comptes Rendus Mécanique*, 340 (11-12):933–943, 2012.

[259] Daniel Robert Lester, Guy Metcalfe, and MG Trefry. Is chaotic advection inherent to porous media flow? *Physical review letters*, 111(17):174101, 2013.

[260] Tanguy Le Borgne, Marco Dentz, and Emmanuel Villermaux. Stretching, coalescence, and mixing in porous media. *Physical review letters*, 110(20):204501, 2013.

[261] Tanguy Le Borgne, Marco Dentz, and Emmanuel Villermaux. The lamellar description of mixing in porous media. *Journal of Fluid Mechanics*, 770:458–498, 2015.

[262] Daniel R Lester, Marco Dentz, and Tanguy Le Borgne. Chaotic mixing in three-dimensional porous media. *Journal of Fluid Mechanics*, 803:144–174, 2016.

[263] Mihkel Kree and Emmanuel Villermaux. Scalar mixtures in porous media. *Physical Review Fluids*, 2(10):104502, 2017.

[264] Régis Turuban, David R Lester, Tanguy Le Borgne, and Yves Méheust. Space-group symmetries generate chaotic fluid advection in crystalline granular media. *Physical review letters*, 120(2):024501, 2018.

[265] Régis Turuban, Daniel R Lester, Joris Heyman, Tanguy Le Borgne, and Yves Méheust. Chaotic mixing in crystalline granular media. *Journal of Fluid Mechanics*, 871:562–594, 2019.

[266] Mathieu Souzy, Henri Lhuissier, Yves Méheust, Tanguy Le Borgne, and Bloen Metzger. Velocity distributions, dispersion and stretching in three-dimensional porous media. *Journal of Fluid Mechanics*, 891, 2020.

[267] Joris Heyman, Daniel R Lester, Régis Turuban, Yves Méheust, and Tanguy Le Borgne. Stretching and folding sustain microscale chemical gradients in porous media. *Proceedings of the National Academy of Sciences*, 117(24):13359–13365, 2020.

[268] Joris Heyman, DR Lester, and Tanguy Le Borgne. Scalar signatures of chaotic mixing in porous media. *Physical Review Letters*, 126(3):034505, 2021.

[269] Katepalli R Sreenivasan. Turbulent mixing: A perspective. *Proceedings of the National Academy of Sciences*, 116(37):18175–18183, 2019.

[270] Siva A Vanapalli, Steven L Ceccio, and Michael J Solomon. Universal scaling for polymer chain scission in turbulence. *Proceedings of the National Academy of Sciences*, 103(45):16660–16665, 2006.

[271] William W Graessley. Polymer chain dimensions and the dependence of viscoelastic properties on concentration, molecular weight and solvent power. *Polymer*, 21(3): 258–262, 1980.

[272] Michael Rubinstein and Ralph H. Colby. *Polymer Physics*. Oxford university press New York, 2003.

[273] Hao Zhang and Yujun Feng. Dependence of intrinsic viscosity and molecular size on molecular weight of partially hydrolyzed polyacrylamide. *Journal of Applied Polymer Science*, page 50850, 2021.

[274] Sujit S Datta, Harry Chiang, TS Ramakrishnan, and David A Weitz. Spatial fluctuations of fluid velocities in flow through a three-dimensional porous medium. *Physical review letters*, 111(6):064501, 2013.

[275] Daniel J Ruth, Wouter Mostert, Stéphane Perrard, and Luc Deike. Bubble pinch-off in turbulence. *Proceedings of the National Academy of Sciences*, 116(51):25412–25417, 2019.

[276] Jeffrey Alan Byars. *Experimental characterization of viscoelastic flow instabilities*. PhD thesis, Massachusetts Institute of Technology, 1996.

[277] P Zitha, G Chauveteau, A Zaitoun, et al. Permeability~ dependent propagation of polyacrylamides under near-wellbore flow conditions. In *SPE International Symposium on Oilfield Chemistry*. Society of Petroleum Engineers, 1995.

[278] Timothy M Obey and PC Griffiths. Polymer adsorption: Fundamentals. *COSMETIC SCIENCE AND TECHNOLOGY SERIES*, pages 51–72, 1999.

[279] Pacelli LJ Zitha, Guy Chauveteau, and Liliane Léger. Unsteady-state flow of flexible polymers in porous media. *Journal of colloid and interface science*, 234(2):269–283, 2001.

[280] CA Grattoni, PF Luckham, XD Jing, L Norman, and Robert W Zimmerman. Polymers as relative permeability modifiers: adsorption and the dynamic formation of thick polyacrylamide layers. *Journal of petroleum science and engineering*, 45(3-4): 233–245, 2004.

[281] Rahul Kekre, Jason E Butler, and Anthony JC Ladd. Comparison of lattice-boltzmann and brownian-dynamics simulations of polymer migration in confined flows. *Physical Review E*, 82(1):011802, 2010.

[282] Hongbo Ma and Michael D Graham. Theory of shear-induced migration in dilute polymer solutions near solid boundaries. *Physics of Fluids*, 17(8):083103, 2005.

[283] Lin Fang, Hua Hu, and Ronald G Larson. Dna configurations and concentration in shearing flow near a glass surface in a microchannel. *Journal of rheology*, 49(1): 127–138, 2005.

This thesis was typeset using LaTeX, originally developed by Leslie Lamport and based on Donald Knuth's TeX. The body text is set in 11 point Egenolff-Berner Garamond, a revival of Claude Garamont's humanist typeface. A template that can be used to format a PhD thesis with this look and feel has been released under the permissive MIT (X11) license, and can be found online at github.com/suchow/Dissertate or from its author, Jordan Suchow, at suchow@post.harvard.edu.